Doctoral Thesis

Mechanism of Defect Formation and Defect-Driven Growth of Two-Dimensional Materials

Hyo Ju Park

Department of Materials Science and Engineering

Graduate School of UNIST

2019

Mechanism of Defect Formation and Defect-Driven Growth of Two-Dimensional Materials

Hyo Ju Park

Department of Materials Science and Engineering

Graduate School of UNIST

Mechanism of Defect Formation and Defect-Driven Growth of Two-Dimensional Materials

A thesis/dissertation

submitted to the Graduate School of UNIST

in partial fulfillment of the

requirements for the degree of

Doctor of Philosophy

Hyo Ju Park

12.10.2018

Approved by

_____

Advisor

Zonghoon Lee

Mechanism of Defect Formation and Defect-Driven Growth of Two-Dimensional Materials

Hyo Ju Park

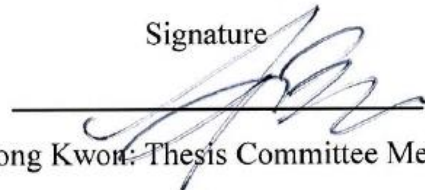This certifies that the thesis/dissertation of Hyo Ju Park is approved.

12.10.2018

Signature

Advisor: Zonghoon Lee

Signature

Soon-Yong Kwon: Thesis Committee Member #1

Signature

Hyung-Joon Shin: Thesis Committee Member #2

Signature

Jung-Woo Yoo: Thesis Committee Member #3

Signature

Eui-Tae Kim: Thesis Committee Member #4

Abstract

The extraordinary properties of graphene have led to intensive research on two-dimensional (2D) materials since the discovery of mechanically exfoliated graphene. Especially development of synthesis of large-area 2D materials films using chemical vapor deposition (CVD) has extremely enlarged the spectrum of potential applications of 2D materials in the fields of various nanotechnology. CVD methods, however, also produce various defective structures with slight modifications to the growth parameters which influence the intrinsic properties of 2D materials. Although defects on 2D materials were often considered as hindrance to degrade the intrinsic properties, if well adjusted, they have huge ability to modulate electromagnetic and mechanical property of the materials, with better performance as needed. Hence, in-depth knowledge of crystal structures with defects and their formation mechanisms must be established to understand the relationship between defects and properties of 2D materials.

In this study, transmission electron microscopy (TEM) have made a significant contribution to understanding in the mechanism of defect formation and defect-driven growth of 2D materials, by directly imaging the features at atomic scale and dynamics of defect formation in real-time, and analyzing information of electron diffraction of crystals, and also examining corresponding change in electric property from the defect structure using electron energy loss spectroscopy.

Among many 2D materials, I have focused on novel defective structures on hexagonal boron nitride (hBN). In contrast to the wide spectrum of proposed applications for graphene as an active component in nanodevices, hBN is often regarded as a passive material where the range of applications is largely confined to substrates or electron barriers for 2D material-based devices due to its electrically insulating feature with a large bandgap and thus received less attention. Herein, through a systematic study using TEM, I report many interesting features of hBN including controllable hole defects, spiral growth driven by screw dislocation at anti-phase boundary, and atomically sharp twin boundary as a promising one-dimensional hBN conducting channel.

Contents

List of Figures

List of Tables

List of Abbreviations

2D	two-dimensional
APB	anti-phase boundary
APCVD	atmospheric pressure chemical vapor deposition
AR-TEM	atomic resolution transmission electron microscopy
CVD	chemical vapor deposition
DFT	density functional theory
DF-TEM	dark-field transmission electron microscopy
EELS	electron energy loss spectroscopy
EK	extended Klein
ELNES	energy-loss near-edge structure
FFT	fast Fourier transform
GGA	generalized gradient approximation
hBN	hexagonal boron nitride
IFFT	inverse fast Fourier transform
LAMMPS	large-scale atomic/molecular massively parallel simulator
MD	molecular dynamics
MoS$_2$	molybdenum disulfide
PAW	projector augmented wave
SAED	selected area electron diffraction
SEM	scanning electron microscopy
STEM	scanning transmission electron microscopy
TEM	transmission electron microscopy
ReaxFF	reactive force field
VASP	Vienna *ab initio* simulation package
vdW	van der Waals
ZLP	zero-loss peak

Chapter 1: Introduction

Defects have huge influence on the electromagnetic and mechanical properties of materials, especially more strongly on two-dimensional (2D) materials since the defects are all located on the surface. Vacancies, dislocations, grain boundaries and other topological defects have been shown to alter its chemical and physical properties and, as such, have been extensively investigated[1-2]. Defects on 2D materials were often considered as hindrance despite of potential controllability in electromagnetic and mechanical property of the materials[3-6]. For example, the actual performance of graphene devices failed to satisfy the expectations due to the inherent defect in them[7]. Although many efforts to remove the defects in 2D materials[8-9] have been performed, it has turned out to be only partial healing of the defects. Accordingly, people started to use these inevitable defects to many applications using the fact that defects can manipulate the electrical and magnetic properties of 2D materials.

Among various types of defects, the hole defects that are made from ejection of atoms from the sheet were studied for many applications as atomically thin nanopores. In the case of graphene, many studies addressed possibility of hole defects as DNA sequencing[10-13], gas sensing[14], ion and molecules sieve[15-16] and many other applications[17-18]. Several comparable studies also have been done with hBN[19] and MoS_2[20-22]. These studies focus on performance tests at the hole defects without the information of edge configuration and chemical stability which may affect to the performance significantly.

Stacking boundaries or phase boundaries of few-layer 2D materials were also shown to possess unique properties which open new ways to control the performance of a material[4, 23-27]. For example, AB/BA stacking boundary with broad range in bilayer graphene showed insulating-like characteristics and reversible transport regimes[24], and 558 line defect formed at a stacking boundary in graphene was reported to act as a metallic wire[4]. One-dimensional twin boundaries found in tungsten diselenide[27], molybdenum diselenide[28] also revealed bandgap changes. In the meantime Li, Q. C. et al. reported Grain boundaries in hBN such as the 5|7 and 4|8 configurations reduce its bandgap to ~3.4 eV and ~4.3 eV, respectively[29].

Among many 2D materials, I have deeply studied especially on interesting defective features of hBN. HBN is analogous to graphene but is comprised of alternating boron and nitrogen atoms. It shows great potential as a substrate for 2D heterostructured devices because of its atomically flat surface, unique electrically insulating nature, and high-temperature and chemical stability[30-31]. Using h-BN as a substrate layer for graphene increases the electron mobility by nearly an order of magnitude compared to conventional SiO_2 substrates[30]. Although reputable for its interfacing capability with other 2D materials and structural similarities to graphene, hBN has been rarely spotlighted to perform an active role in 2D electronics as limited by its insulating nature. Thus, I have studied the novel defective structures of hBN and postulate the mechanism of defect formation and defect-driven growth of hBN

major assistant with transmission electron microscopy (TEM) analysis plus theoretical calculations of density functional theory (DFT) and molecular dynamics (MD) simulations.

Firstly, production of holes by electron beam irradiation in hBN was monitored over time using atomic resolution (AR) TEM. The holes appear to be initiated by the formation of a vacancy of boron and grow in a manner that retains an overall triangular shape. The hole growth process involves the formation of single chains of B and N atoms, and is accompanied by the ejection of atoms and bundles of atoms along the hole edges as well as atom migration. hBN hole defects have advantage in shape control to triangle, hexagon and randomly shaped hole by managing the number of layers and the stacking structure. And it always has N-terminated zigzag edges which make it possible to control the electromagnetic properties for nanopore devices.

Second, the formation of intertwined double-spiral few-layer hBN that are driven by screw-dislocations is reported. Pairs of screw dislocations initiated at the anti-phase boundaries (APBs) of monolayer domains make double-spiral structure. Distinct from other 2D materials with single-spiral structures, the double-spiral structure enables the intertwined h-BN layers to preserve the most stable AA′ stacking configuration. Unlike commonly reported few layers grown by interfacial nucleation where the second layer is grown independently beneath the first, the growth of a spiral structure adopts a top growth mechanism where the top layers are an extension from the initial monolayer which spirals around an axial dislocation in self-perpetuating steps. I also found that the occurrence of strains between merged spiral islands is dependent on the propagation directions of encountering screw dislocations, and present the strained features by density functional theory calculations and atomic image simulations. This study unveils the unique double-spiral growth of 2D hBN multilayers synthesized in a chemical vapor deposition (CVD) chamber.

And lastly, I will discuss about one-dimensional hBN conducting channel with 6′6′ and 558 configuration embedded at AA′/AB stacking boundaries of few-layer hBN. In contrast to the electronic properties found in pristine hBN, this atomically sharp twin boundary displays a highly reduced bandgap close to zero. Such atomic wide channels can potentially create ultimately narrow active passages for electrons or form an embedded single-hBN device within an electrically non-conducting hBN sheet. Furthermore, formation mechanism of atomically sharp twin boundaries is suggested by analogy of stacking combinations of AA′/AB with observations of extended Klein edges at the layer boundaries of AB-stacked hBN.

Chapter 2. Research background

2.1. Aberration corrected transmission electron microscopy

There has been a constant demand for higher resolution of electron microscopy since after its invention. With the development of nanoscience and nanotechnology, atomic-scale synthesis requires atomic resolution characterization[32-33], even higher resolution far below 1 Å to identify individual atoms or vacancies in materials. Although a "high resolution" TEM imaging already became a quite common technique a few decades ago in materials science[34], that was concerned with collective crystal properties from atomic columns in bulk crystal structure, rather than real "individual" atomic positions or behaviors. In the meantime, the advent of low dimensional materials intensified the needs of atomic resolution characterization[35].

Over the last few decades, a huge progress has been made in TEM with the introduction of an aberration corrector[36-41]. Basically, the limitation of resolution of TEM come from a fundamental failure of building perfect electron lenses, which cause spherical aberrations. And another type of aberration, chromatic aberration, which arise from the electron-energy dependence of the refraction properties of magnetic fields, also limits the resolution. Two types of aberrations are illustrated in Figure 1. According to Scherzer theorem, correcting the spherical and chromatic aberrations just by combination of ordinary lenses is impossible[42]. Since the electromagnetic focusing fields in TEM are free of space charge, cylinder-symmetric, and the optic axis has no point of reversal, spherical aberrations are compensated by breaking the cylindrical symmetry or adopting a reflecting device[43-45]. Hexapole-type spherical aberration correctors have been realized successfully in conventional TEM and scanning TEM (STEM) and demonstrate their advantages by various applications[46-49]. For the latter, multiple quadrupole-octopole systems[50-51] are also used. And then, the chromatic aberration can be almost free by using a chromatic aberration corrector or monochromator which minimize the energy spreading the electron beam[52].

As a consequence, the electron microscopes has undergone a dramatic improvement with achievable resolution having more than doubled in a very short time with the development of aberration correctors[53-55] as illustrated in Figure 2. And due to this revolution by the successful correction of lens aberration, now we can probe the individual atoms and defects in low dimensional materials even in the low acceleration voltages such as 60 and 80 kV, which significantly minimizes the damaging effect on the specimen[2, 56].

Beyond the atomic resolution imaging such as mapping of atomic positions, aberration-corrected TEM allows atomic scale imaging of chemical composition and bonding by combining high resolution in energy and space with the use of spatially-resolved electron energy loss spectroscopy (EELS) to map electron states localized at or between atoms[57-59].
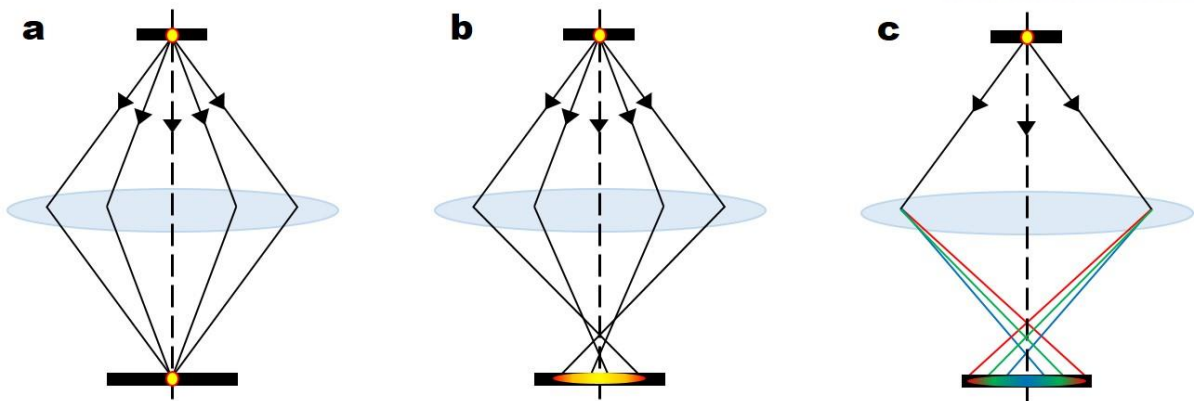
Figure 1. Schematic illustration of lens aberrations of a converging lens. a, A perfect lens focuses a point source to a single point in the image plane. **b**, Spherical aberration causes electron waves from a point source spherically distorted by bending the rays at higher angles to be overfocused. Thus the point is images as a disk. **c**, Chromatic aberration causes rays at different energies (indicated by color) to be focused in different planes.
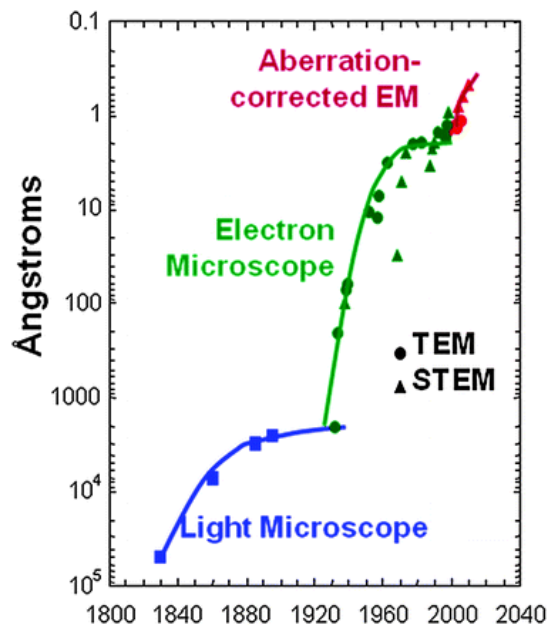
Figure 2. The evolution of resolution in microscopy. Spatial resolution versus year for light and electron microscopes. The data is adapted from Reference 53, 54. The figure is reprinted from Yang et al. (2012) (Chem. Soc. Rev., 41, 8179-8194). Copyright 2012 Royal Society of Chemistry.

2.2. Hole defects on 2D materials induced by electron beam irradiation

2.2.1. Formation of defect by electron beam and knock-on thresholds of graphene, hBN and MoS$_2$

Among various methods to make holes on 2D materials[16, 60-64], electron beam in TEM is good at size control at atomic scale, which is the most important issue for the sensitivity and selectivity of nanopore devices. If electron beam irradiation on a 2D specimen with a high electron energy breaks the atomic bonds within the material, which is called knock-on voltage, atoms are ejected from the lattice leaving holes on the materials. The atom displacement, knock-on thresholds and other structural information of graphene[65], hBN[66] and MoS$_2$[67] are summarized in Table 1.

Materials	Atomic Number	Lattice System	Lattice Parameter	Displacement Threshold	Knock-on Threshold
Graphene (Smith & Luzzi, 2001)	C:6	Hexagonal	2.46A	**17eV**	**86kV**
hBN (Kotakoski et al., 2010)	B:5	Hexagonal	2.51A	**B:19eV**	**79.5kV**
	N:7			**N:23eV**	**118.6kV**
MoS$_2$ (2H) (Komsa et al., 2012)	S:16	Hexagonal	3.2A	**S:6.9eV**	**80keV**
	Mo:42			**Mo:20eV**	**560keV**

Table 1. The calculated values of displacement threshold and knock-on threshold of graphene, hBN and MoS$_2$.

2.2.2. Hole defects on graphene

Figure 3a shows the hole defects of graphene by the electron beam irradiation at 80 kV. To make hole defects in graphene, over 86 kV of electron beam energy, the knock-on threshold voltage of graphene, needs to be irradiated on the sample. But some studies showed the existence of oxygen or other chemicals on the sheet or inside TEM chamber can lower the knock-on threshold of graphene by chemical etching effect[68]. Inherent defects created from the synthesizing process of graphene also lower the knock-on threshold voltage[69]. Once a vacancy is formed, it continuously grows as electron beam irradiates to make an enlarged hole in the sheet. The size of hole defect can be controlled by the time of electron beam irradiation at a given acceleration voltage.

The hole defect of graphene has mixed armchair and zigzag atomic configuration at the edge. Because the edge configuration of graphene are known to have significant influences to the electromagnetic property of graphene[70-74], the edge configuration and its stableness become one of major interests in studies of graphene hole defect. Direct atomic imaging at the graphene edges using aberration corrected TEM gave the insight on the stability of edge configurations[64, 75-77]. Recently, He et al. reported the temperature dependence of graphene edge configuration through in-situ heating experiment using TEM[64]. As shown in Figure 3b, c, armchair and reconstructed 5-7 zigzag configurations were predominant above 600 °C which has good agreement with the theoretical predictions[78]. Below 400 °C, zigzag configuration was dominantly observed, which was led by major involvement of chemical etching process from contamination of sample. It gives a prospect in edge control of graphene hole defect for graphene nanopore devices, though contamination effect still remains an issue to be resolved.

Meanwhile, high reactivity of the edges of graphene hole defect has been a big obstacle to realization of graphene nanopore devices. Graphene has high reactivity with chemicals, especially at the hole edges that have dangling bonds. For example, DNA would be fond of sticking to the hole edges and surface when translocating the graphene nanopore, which makes it complicate to identify the DNA sequence[79-80]. Moreover, despite all the efforts to make holes, small holes in graphene are filled with carbon adatoms nearby within hours even under ultra-high vacuum conditions of TEM as shown in Figure 3d, e[81]. Thus, fixation or stabilization of hole defects is emerging as a key issue for graphene nanopore devices and passivation of hole edges with other atoms was suggested as one potential method as shown in Figure 3f-j[82]. Si-passivated holes in graphene were directly observed using STEM, and proved to be stable against carbon filling even under intense electron beam condition and ambient atmospheric condition. MD simulations supported this observation, showing that carbon adatoms would stick out of the graphene plane preventing filling hole defects. Si passivation opens potential of stabilization of hole defects, however, the fabrication methods should be further developed. Additionally, considering the binding energy between C-Si at armchair site is higher than that at zigzag site, importance of

understanding edge configuration of graphene hole defects is highlighted again. Therefore, in-depth studies on the edge configuration and stabilization will make progress toward graphene nanopore devices.
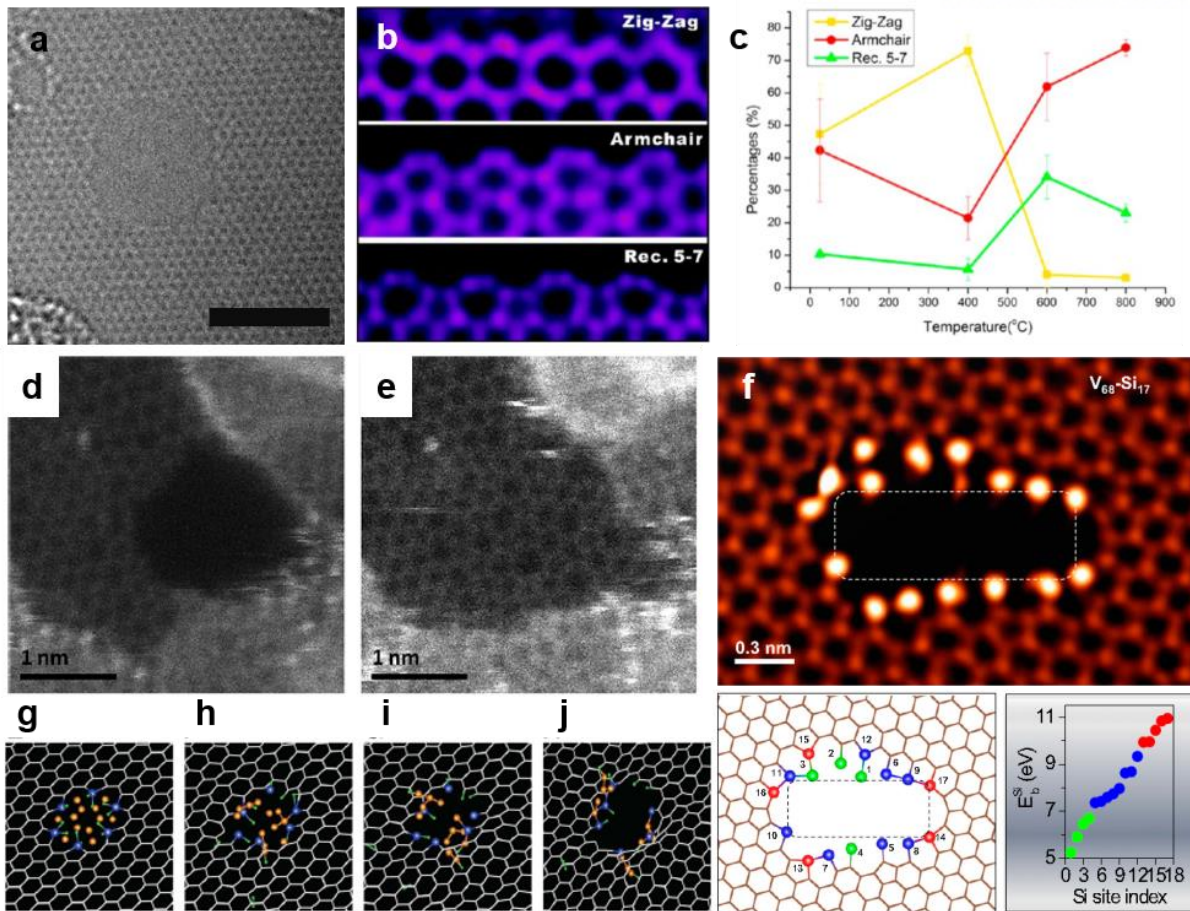
Figure 3. Features and stability of graphene hole defects. a, AR-TEM image of graphene hole defect. Scale bar, 2nm. **b**, Graphene has zig-zag, armchair, reconstructed 5-7 zigzag configuration at the edges. **c**, Percentage of each edge configurations is marked on the graph. It shows temperature dependence of edge configurations. **d**, STEM image of hole defect created near the hydrocarbon contamination. **e**, The hole is filled with C polygons even under ultra high vacuum condition. **f**, STEM image and structure model of Si-passivated graphene hole defect and binding energy of Si atoms at the edge. Si-passivated hole defect is stable against hole filling. **g-i**, *ab initio* MD simulations reveal the Si-passivated hole forms bonding with C adatoms out of the graphene plane, preventing the hole filling.

(b and c) Reprinted from He et al. (2015) (*ACS Nano* 9, 4786-4795) with original copyright holder's permission. Copyright 2015 American Chemical Society.

(d and e) Reprinted from Zan et al. (2012) (*Nano Lett*. 12, 3936-3940) with original copyright holder's permission. Copyright 2012 American Chemical Society.

(f-j) Reprinted from Lee et al. (2014) (*PNAS*, 111, 7522-7526) with original copyright holder's permission. Copyright 2014 National Academy of Sciences, USA.

2.2.3. Hole defects on hBN

Compared to graphene, hBN has received less attention as a 2D device due to the difficulties in getting synthesized large sheet and non-conducting property[83]. As an insulator, hBN has been used as a substrate of graphene to show high electrical performance[84], but not much used alone. However, Liu et al. remarked hBN may exhibit superior durability and insulating properties in high-ionic strength solution compared with graphene and realized hBN nanopore device for DNA sensor[19].

The notable thing is that hBN hole defects have a unique feature in shape, which is controllable unlike graphene. Figure 4a-c represent a triangular hole defect in monolayer hBN sheet. Because boron has a lower knock-on threshold than nitrogen under transmission electron beam (See the Table 1), 80 kV of electron beam preferentially knock off the boron atoms first, making B monovacancies with N terminated edge along the hole defect edge[66, 85-87] (Figure 4a). The hole defect formed by prolonged electron beam irradiation at Figure 4a is defined as triangular shape more clearly (Figure 4b). This triangular hole defect maintains its shape as it grows which is verified up to area of 110 nm^2 (Figure 4c). Atomic model of triangular hole defect in Figure 4d shows that the edges are terminated with N atoms. According to the calculation result of Kotakoski et al., N monovacancy as well as B monovacancy is expected to be formed by above 120 kV of electron beam[53]. Nevertheless, all experimental results using TEM have shown N terminated triangular hole defect starting from B monovacancy. Yin et al. explained by cohesive energy calculations that N-terminated hole defect is more stable than B-terminated one due to the ionic character of the material[88]. Hole defects created by electron beam on monolayer hBN sheet will be more discussed deeply in Chapter 3.

Furthermore, hexagonal hole defect could be fabricated in AA′-stacked double layer hBN sheet. The nature of AA′ stacking structure of hBN, which B atoms are on top of N atoms and vice versa, makes the orientation of defects in one layer 180 degree opposite to those in the other layer of hBN sheet[87]. Two opposite triangle defects grow and result in a hexagonal hole defect with N terminated zigzag edges (Figure 4e). Because AA′ stacking structure is known to be the most stable structure in bulk hBN structure[89], AA′-stacked double layer hBN can be easily obtained through the scotch-tape exfoliation[90]. If double layer of hBN is randomly rotated each other by stacking two monolayer of hBN, hole defects have no longer triangular or hexagonal shaped hole defects (Figure 4f). The rotated stacking structure can be directly inferred from the Moire pattern. To sum up, ultimately we are able to manufacture freely the hBN nanopores in shape by managing the number of layer and stacking structure, and in size by the irradiation time. Due to these shape and size of hBN hole defects with controllable manners, the utilization of the hBN nanopores as a nano-patterning template is promising. Also N-terminated hole defect of hBN is found to give enhanced half-metallicity and large magnetism. It suggests the potential of hBN nanopore application for spintronics, light emission and photocatalysis[91].
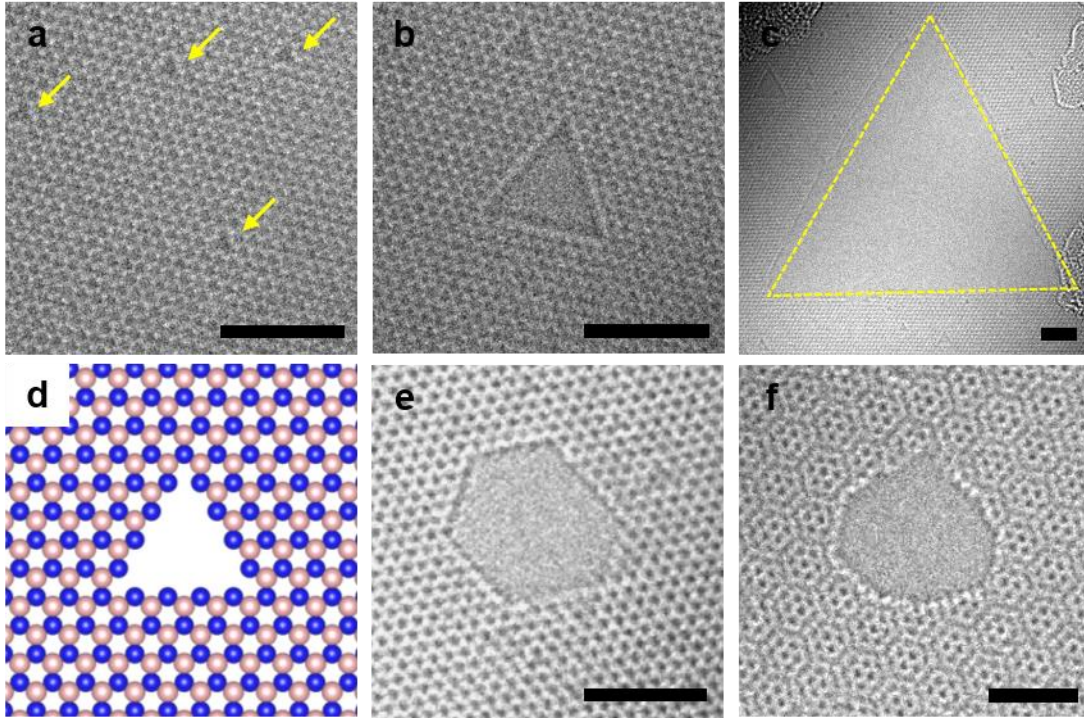
Figure 4. Hole defects on mono- and double-layer hBN. a-c, In monolayer hBN, hole defects grow with maintaining triangular shape from monovacancy (**a**) to enlarged (~ 110 nm²) hole (**c**) by electron beam irradiation. **d**, Atomic model of N-terminated edges of hBN hole defect. The pink and blue balls represent boron and nitrogen atoms, respectively. **e**, Hexagonal shape of hole defect is created on AA′-stacked hBN double layer. **f**, Randomly shaped hole defect is created on rotated hBN double layer. Scale bars, 2 nm.

2.2.4 Hole defects on MoS_2

MoS_2 has been growing interest as a promising material due to its semiconducting nature which makes it facile to make sensing and electronic applications[20-22]. Especially as a DNA detecting sensor, MoS_2 nanopore membranes have shown better performance than graphene nanopore membranes for transverse detection without special surface treatment process to prevent the interaction between DNA and the surface, unlike graphene[79].

MoS_2 is commonly found in 2H form in nature among three polytypes: 1T, 2H and 3R. Synthesized MoS_2 films may have 3R structures[92] but most of studies on MoS_2 defects are performed with exfoliated MoS_2, so with 2H structure. The smallest hole in 2H MoS_2 can be created by the removal of one Mo atom or two S atoms (Figure 5a-c) but much higher concentration of S site holes than Mo site holes are found in TEM due to the different knock-on threshold of S and Mo atoms[93].

Figure 5d-f are the serial images of MoS_2 hole defect created by 80 kV of electron beam in TEM. Because the knock-on thresholds of S and Mo atom are 80 kV and 560 kV respectively as shown in Table 1, S vacancies are formed first by slightly focused electron beams. Meanwhile Mo atoms are less likely to be ejected by 80 kV electron beam, resulting in the agglomeration of Mo atoms at the edge of hole defects. Mo atoms aggregate at the edge under continued electron beam irradiation. Although a few papers reported the phenomenon of Mo atoms agglomeration[94-95], none reported the corresponding effects in electrical or magnetic properties at the edge. According to the theoretical calculations[96], Mo-Mo metallic bonds are formed at S vacancy sites and cancel the magnetism by pairing the unsaturated spin electrons. Similarly, the degree of Mo atoms agglomeration may affect to the metallicity so to the electrical performance such as the current signals when DNA or molecules transverse the holes. Therefore, for MoS_2-based nanopore devices, understanding of edge configuration of MoS_2 hole defects and consequent electrical and magnetic properties is required.
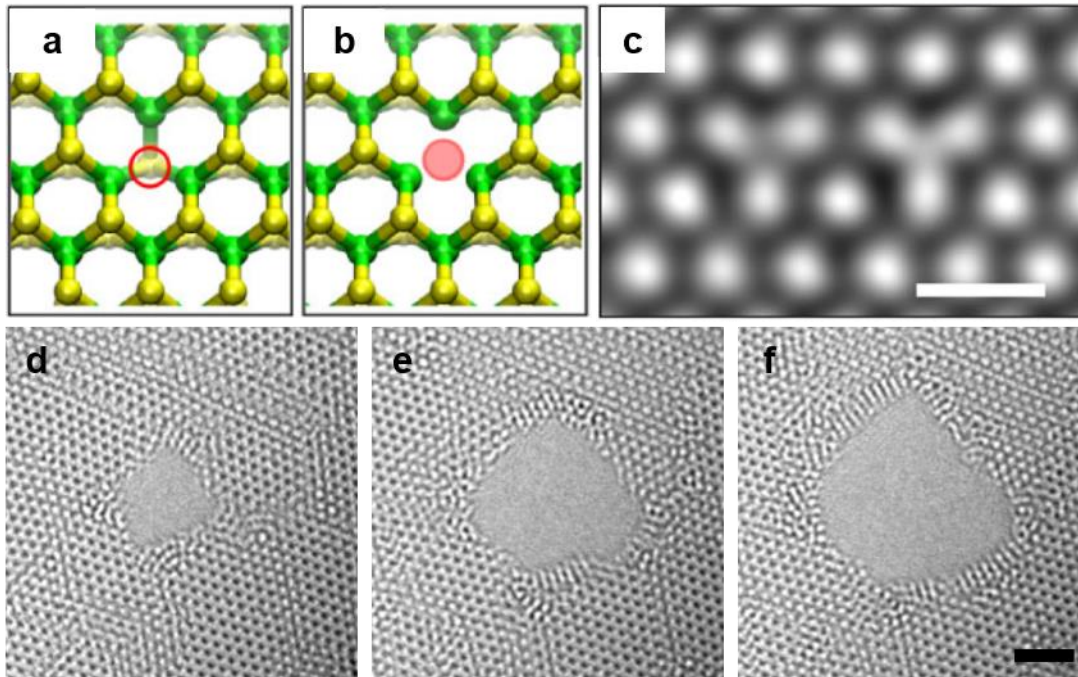
Figure 5. Point defect and enlarged hole defect on MoS₂. a,**b**, Structure models of single S atom vacancy (**a**) and double S atoms vacancies (**b**), creating a point defect. Corresponding TEM image is shown in (**c**). The left and right one are one and double S atoms ejected site, respectively. Scale bar, 5 Å. **d-e**, The sequential growth process of a hole defect by electron beam irradiation in monolayer MoS₂ sheet. Mo atoms aggregate at the edge. Scale bar, 2 nm.

(a-c) Reprinted from Komsa et al. (2012) (*Phys. Rev. Lett.* 109, 035503) with original copyright holder's permission. Copyright 2012 American Physical Society.

2.3. Stacking structure and Stacking boundary of hBN

2.3.1 Stacking structures of hBN

Due to its bi-elemental composition, hBN can assemble in various stacking structures, with two different types of interlayer orientations. In this study, I use the symbols [BN] and [NB] (a hexagonal structure rotated by 60° relative to [BN]) to represent hexagonal structures defined by the order of atoms clockwise from the apex (Figure 6a).

There are six possible stacking structures with high symmetry, depending on the rotation (0° or 60°) and translation of the hexagons relative to the bottom layer, termed "A" (Figure 6b). The structure in which all atoms in the upper and lower layers are in the same positions and the same orientations is termed "AA stacking". The structures in which the upper layer is translated to the center of a hexagon in the lower layer are called either "AB stacking" or "AC stacking". Both AB and AC stacking are also known as "Bernal stacking," which is easily found in graphite. The AB and AC stackings are distinguished in this paper since the consequential atomic configurations at stacking boundaries are different even though AB and AC have the same level of structural stability. The configuration in which the N atoms are on top of the B atoms is defined as the "AB stacking structure," and the opposite is true for "AC stacking" in this paper. The prime (′) mark indicates that the orientation of the upper layer is rotated by 60° relative to the lower layer like [BN]/[NB] or [NB]/[BN].

The stability of a stacking structure depends strongly on the interactions between the atoms in the upper layer with those in the lower layer. Since differing atoms (B-N) experience an attractive force, while identical atoms (B-B or N-N) have a repulsive interaction, AA′ is the most stable structure, and AB and AC are less stable[97-98].
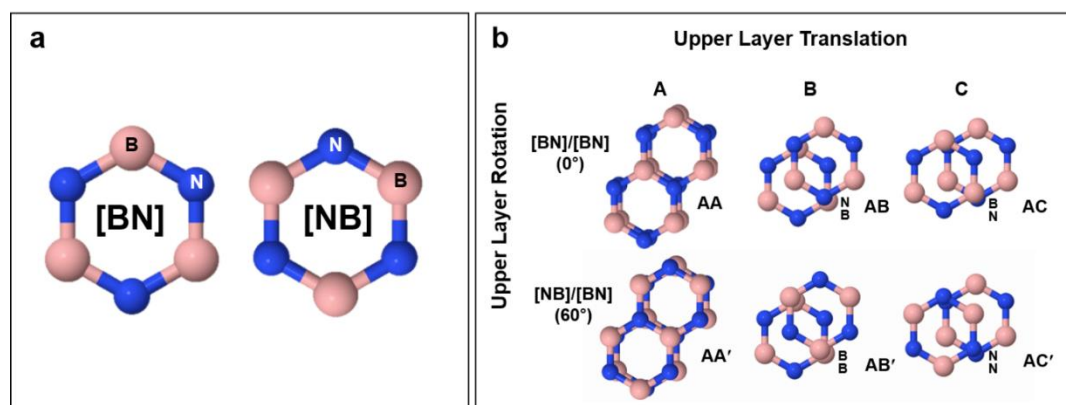
Figure 6. Stacking structure of hBN. a, Atomic models of the [BN] and [NB] configurations. **b**, High-symmetry stacking structures of hBN. Boron and nitrogen atoms are represented in pink and blue, respectively.

2.3.2. Identification of the stacking structure and the number of layers of hBN using DF-TEM

The stacking structure and the number of layers of hBN can be determined by measuring the intensity of dark-field (DF) TEM images. The intensity of the DF-TEM image depends on the interference of electron waves produced though the specific lattice periodicity, corresponding to the diffraction spot being used in acquiring the DF-TEM image. Thus, it is sensitive to the lateral translation between layers. As shown in Figure 7, for AA′ stacking, which has no lateral translation, the intensities of the first- ($\Phi1$) and second-($\Phi2$) order families of diffraction spots increase with the number of layers since the electron wave diffracted from one layer always interferes constructively with the wave diffracted from the other layers. In contrast, for Bernal stacking, like AB or AC, in which one layer of the lattice is translated with a lattice spacing of $3a/2$ relative to another, a phase difference is caused depending on the diffraction spot. The electron wave interferes destructively along the 2.16 Å ($\Phi1$) lattice periodicity but it still interferes constructively along the 1.25 Å ($\Phi2$) lattice periodicity[99-100]. For ABC stacking, the $\varnothing1$ diffraction spots show completely destructive interference since the phases of the electron wave scattered from the AB and AC stackings are opposites[101-102].
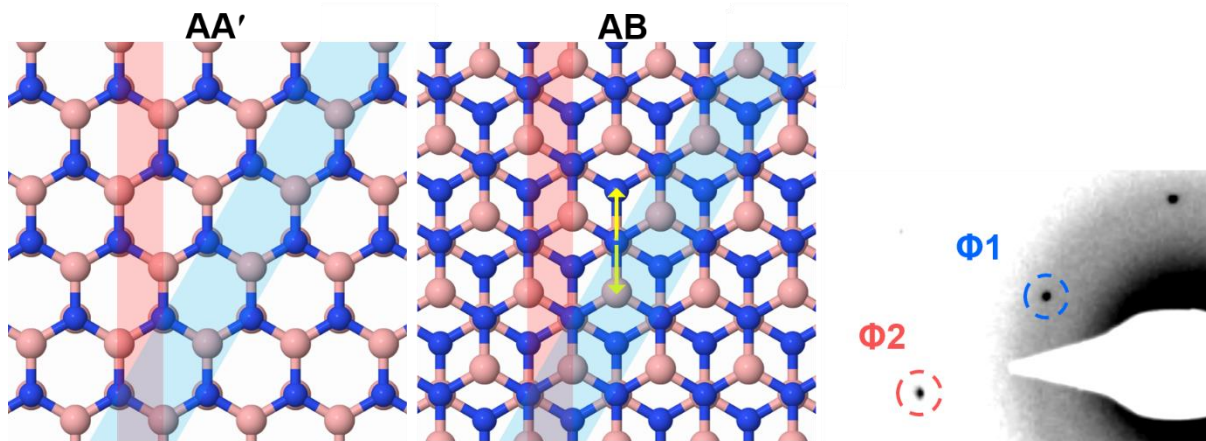
Figure 7. Schematics of the AA′ and AB stacking structures of hBN. The lattice periodicity of 2.16 Å (1. 25 Å) is highlighted in blue (red) and corresponds to the diffraction spot $\Phi1$ ($\Phi2$) in the SAED patterns. Displacement vectors for the AB or AC structures are marked in yellow. Boron and nitrogen atoms are represented by pink and blue, respectively.

2.3.3 Transition region at stacking boundary

As discussed in the previous section, bright contrast in a DF-TEM image means constructive interference of the waves diffracted from a given lattice. Especially for the second-order diffraction spots ($\Phi 2$), the DF-TEM images always have brighter contrast with increasing numbers of layers if the hBN layers are oriented in a high-symmetry stacking structure. Thus, the dark line displayed in Figure 9c, is the locus of positions of atoms in one layer that are shifted relative to other layers, causing destructive interference[99, 103-105]. Considering that an selected area electron diffraction (SAED) pattern shows one set of hexagonal spots (Figure 8d), the relative positions of the atoms shift gradually, without any rotation of the dark-line region. That is, the dark line indicates the presence of a transition region at the boundary between the two different stacking structures. The higher mag TEM images of Figure 8e, f, directly demonstrate this. The red dashed lines are the outlines of triangular defects caused by prolonged electron-beam irradiation. The opposite directions of the red outlines, which are divided by the black dashed line, indicate a change of phase between [BN] and [NB]; the orientations of triangular defects are in opposite directions in [BN] and [NB] structures since the electron beam always creates N-terminated triangular defects. The atomic-scale image for the region marked with a black arrow in Figure 8f loses the original hexagonal lattice contrast, which indicates a transition region, not in high-symmetry stacking, between different stacking structures. The various stacking structures noted in Figure 8b are identified by using the characteristics of DF-TEM images that the image contrast from $\Phi 1a$ and $\Phi 1b$ are alternatively bright for odd (even) numbers of layers when they have the AB (AC) stacking structure. The AA′/AB stacking boundary of hBN will be discussed in detail in the Chapter 5.
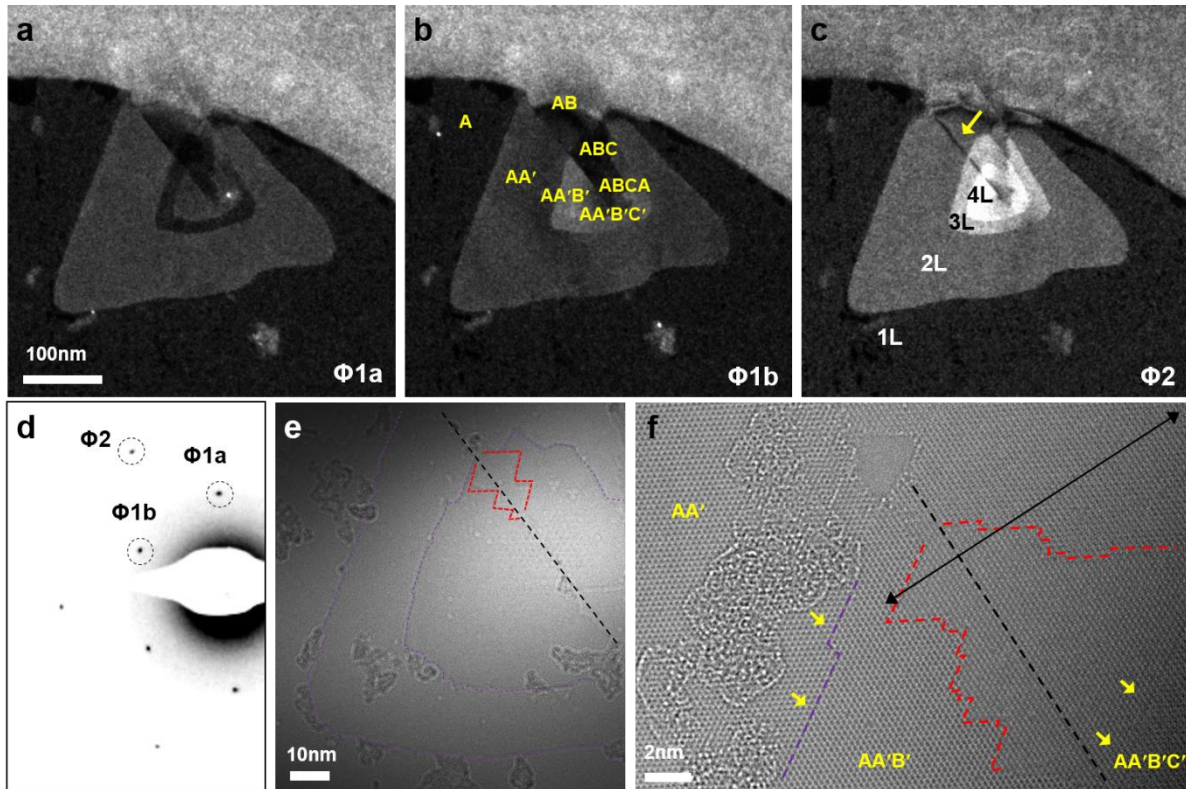
Figure 8. Transition region at AA′/AB stacking boundary of hBN. a-c, DF-TEM images from the diffraction spots Φ1a, Φ1b, and Φ2, respectively, in (**d**). The different stacking structures are designated in (**b**), and the numbers of layers are given in (**c**). **e**,**f**, The corresponding TEM images under low (**e**) and high (**f**) magnification after electron-beam irradiation. The red dashed lines show the triangular defects caused by the TEM electron beam. The region indicated by the black dashed lines in (**e**) and (**f**) matches the region represented by the dark line in (**c**).

Chapter 3. Atomic-scale dynamics of triangular hole growth in monolayer hBN

3.1. Introduction

Defects are known to influence the intrinsic electronic and mechanical properties of materials. In graphene, vacancies, dislocations, grain boundaries and other topological defects have been shown to alter its chemical and physical properties and, as such, have been extensively investigated[1-2]. The defect structures in hBN are even more varied and complex because, unlike graphene[106-107], its hexagonal 2D lattice is occupied by two elements. Indeed, most reports have focused on defect formation and characterization[86, 108-109] in localized regions of exfoliated hBN. At present, it is known that the edges of holes in hBN layers usually adopt zigzag and armchair-type configurations, with the former being more common[108]. Moreover, the zigzag configuration contains two different types of terminated edges due to the heterogeneity of hBN, factors that have been shown to affect the material's intrinsic electrical properties[110]. The growth mechanisms of extended holes in hBN are also not well established. For example, unlike graphene, where single chains of carbon atoms and related defects are well characterized[111-116], single chains made deliberately in hBN sheets via *in situ* production techniques (i.e., inside a transmission electron microscope) have been observed at 650 °C[117].

Herein, the growth of triangular holes is studied in large, monolayer sheets of hBN from the nucleation of a B vacancy to areas that exceed 50 nm^2 using AR-TEM. As part of these studies, the growth dynamics of single triangular holes as well as the processes by which they merge with other holes were explored. The experimental observations were then compared with DFT calculations and MD simulations, which provided additional insight into the mechanisms of hole growth.

3.2. Experimental section

Synthesis of hBN and AR-TEM observations. The hBN specimens used in the experiments consisted primarily of monolayers and were synthesized using chemical vapor deposition[83]. Conventional TEMs do not have adequate resolution for imaging single atoms of hBN and are often operated at high voltages, which lead to immediate irradiation damage in the specimens before reliable observations can be made. Furthermore, if experiments are performed at a low voltage such as 60 kV, knock-on damage as well as ionization damage should be considered. To avoid these problems, specimens were analyzed using an aberration-corrected FEI Titan Cube TEM (FEI Titan3 G2 60-300), which was operated at 80 kV acceleration voltage since 80 kV is an intermediate value of the knock-on threshold values of B (74 kV) and N (84 kV)[118]. Therefore, the experiments mainly consider the knock-on damage. The microscope provides sub-Angstrom resolution at 80 kV and -21±0.5 μm of spherical aberration (Cs) with a monochromator and thus is capable of imaging individual atoms within the hBN lattice. Typical electron beam densities were adjusted to around 5×10^5 e- nm-2. The atomic images are taken with a white atom contrast (as opposed to a black atom contrast) in order to obtain actual atom positions under properly focused conditions needed for direct image interpretation.

Time Lapse Microscopy. After acquiring a series of images using the Gatan Digital Micrograph Script, structural changes in the observed area were analyzed frame-by-frame. Each of these images was taken with an exposure time of 0.5 sec and an interval time of 1.7 sec. To facilitate the identification of the holes generated by electron beam irradiation, clean areas that were free of adsorbates and other impurities were examined.

DFT Calculations. Density functional theory calculations were performed using the Vienna *ab initio* simulation package (VASP)[119-120]. A single k-point (Γ point) for a 15 x 15 supercell with a cutoff kinetic energy of 400 eV was used. The ions were represented by projector-augmented wave (PAW) potentials[121-122], and van der Waals (vdW) interactions[123] as used in Grimme's theory were implemented into the VASP. A generalized gradient approximation was used to describe the exchange-correlation functional[124-125]. The atomic positions of all structures were relaxed until the Hellmann-Feynman forces were lower than 0.01 eV/Å.

MD Simulations. To explore hole growth in layers of hBN, MD simulations were performed using the large-scale atomic/molecular massively parallel simulator (LAMMPS) code[32] with reactive force field (ReaxFF) potentials[126-128]. The MD time step was set to 0.25 fs, which was determined from a stability test using a microcanonical ensemble (NVE). To properly account for the electron beam irradiation, heating was controlled during simulation by increasing the temperature from 1000 K to 4000 K for 1000 ps using a canonical ensemble (NVT) and the Nose-Hoover chain thermostat.

3.3. Results and discussion

To elucidate the mechanism of hole growth in hBN monolayers, the dynamics of triangular holes induced by electron beam irradiation were analyzed using AR-TEM. A large area monolayer of hBN was grown by chemical vapor deposition and then transferred to a TEM grid. Figure 9 shows the formation and growth of large triangular holes in monolayer hBN by electron beam irradiation.

The hBN hole growth process was subsequently investigated (Figure 10). A vacancy labeled VB, which refers to the site of a missing B atom, is shown in Figure 10a. Through continuous electron beam irradiation, B and N atoms were removed from sites adjacent to VB in a manner that maintained an overall triangular shape, although some trapezoidal intermediates were observed. For example, while the removal of a pair of B and N atoms adjacent to the VB (i.e., VB-BN) resulted in the formation of a trapezoidal site, a triangular hole reformed upon the subsequent loss of an additional B atom (e.g., VB-BN-B), as shown in Figure 10c. This process continued as the hole grew and involved the temporary introduction of an atom within the growing hole (c.f., Figure 10d and 11e; see below for a deeper discussion of the migration of B and N atoms).
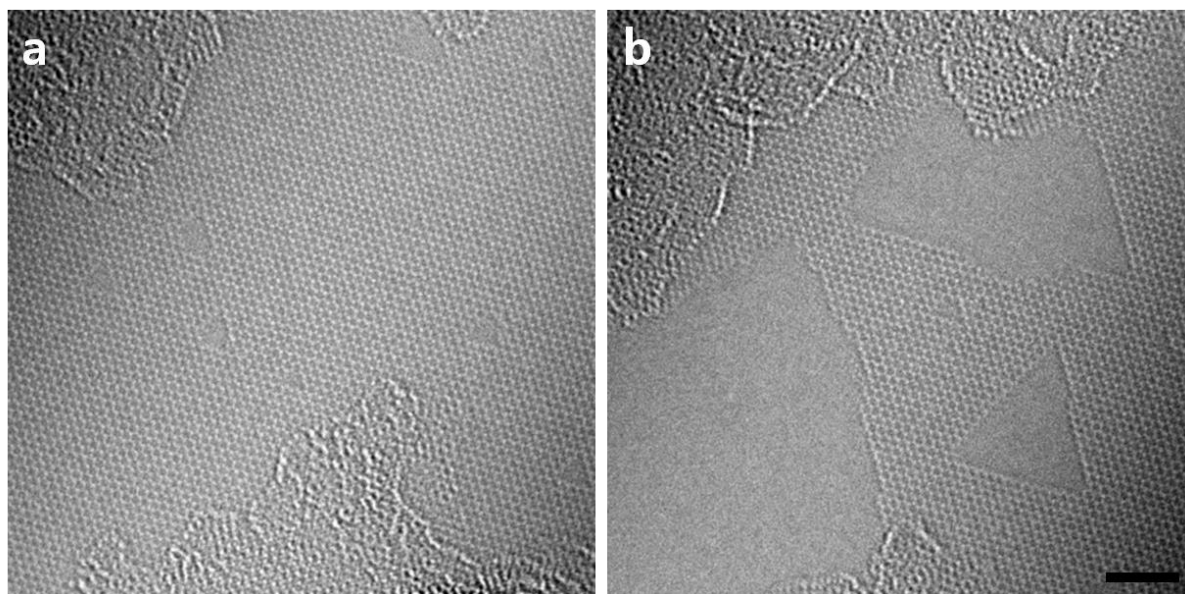
Figure 9. Formation and growth of large triangular holes in monolayer hBN by electron beam irradiation. The TEM images show (**a**) the initial defects and (**b**) an enlarged area of the same region. Scale bar, 2nm.
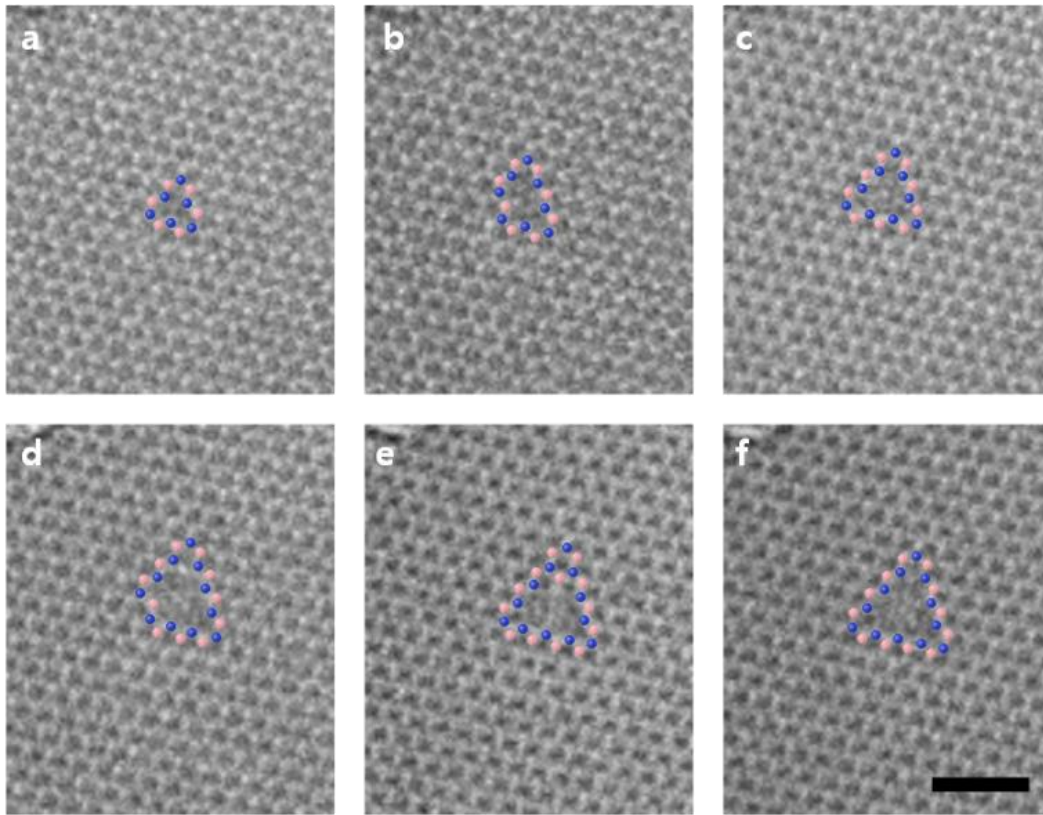
Figure 10. The sequential hole growth process from a vacancy in monolayer hBN at atomic resolution. The process starts (**a**) with the development of a B vacancy (V_B) and grows as shown in (**b**) to (**f**). The blue and red dots reflect the N and B atoms, respectively. Scale bar, 1 nm.

Efforts were then directed towards assessing whether the holes maintained their triangular shape after prolonged periods of electron beam irradiation. As summarized in Figure 11, the growth of a triangular hole appeared to be initiated by the removal of B and N atoms near the centers of the hole edges. This experimental observation was supported by energy calculations, which indicated that triangular holes featuring edges with missing B and/or N atoms are more stable than those with atoms missing near a vertex (Figure 12). Regardless, under prolonged electron beam irradiation, the B and N atoms next to the vacancies were subsequently ejected in a manner that ultimately restored the overall triangular shape of the hole. As shown in Figure 13, the triangular shape of the holes was maintained even after two holes merged together. Additionally, exposure of an edge region to electron beam irradiation resulted in the formation of triangular holes. Once electron beam irradiates within or at edge of a hBN sheet, a N terminated triangular hole is unconditionally formed and its shape is maintained during the hole growth process.
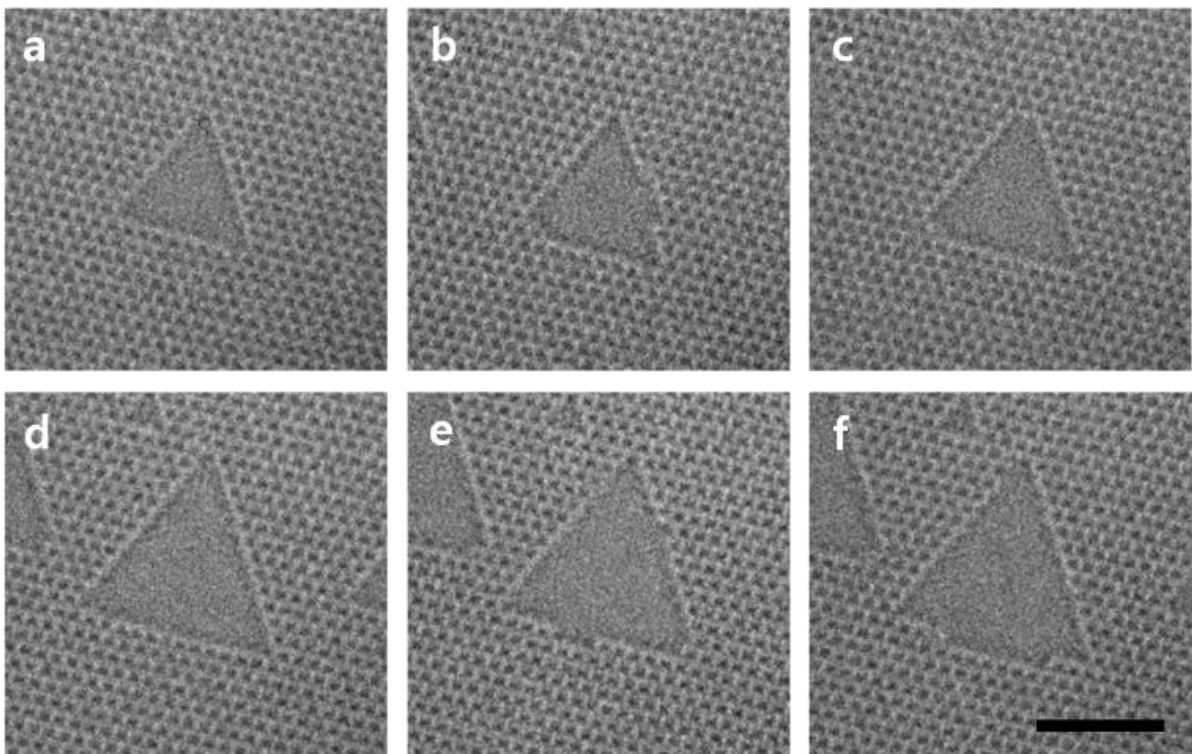
Figure 11. Sequential atomic resolution images of monolayer hBN showing how the shape and orientation of the holes are maintained upon further growth.
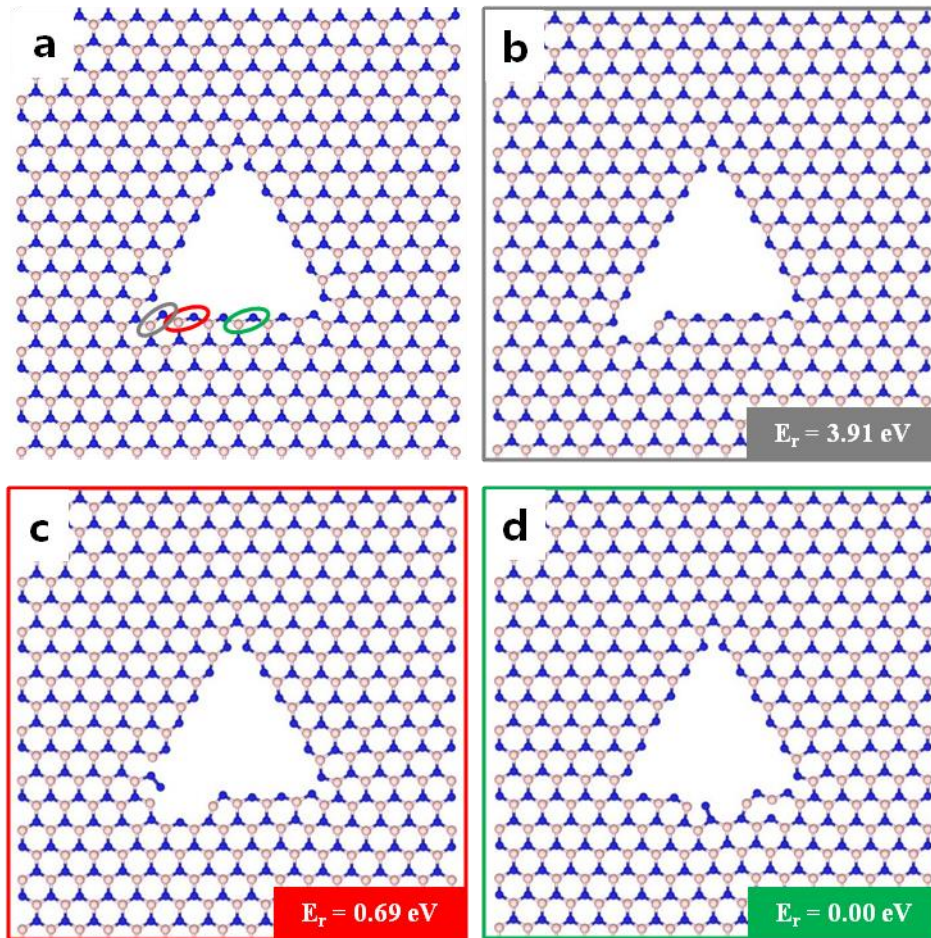
Figure 12. Comparison of formation energy in missing B-N atoms at a corner, near the corner, and near the middle region of a defect edge. a, Models for paired B–N atoms missing at an edge of a triangular hole defect in a monolayer hBN sheet with their relative energies: (**b**) at a corner; (**c**) near the corner; and (**d**) near the middle region of a defect edge. Paired B–N atoms missing near the middle of an edge appear to be more stable than those missing at a corner or near a corner.
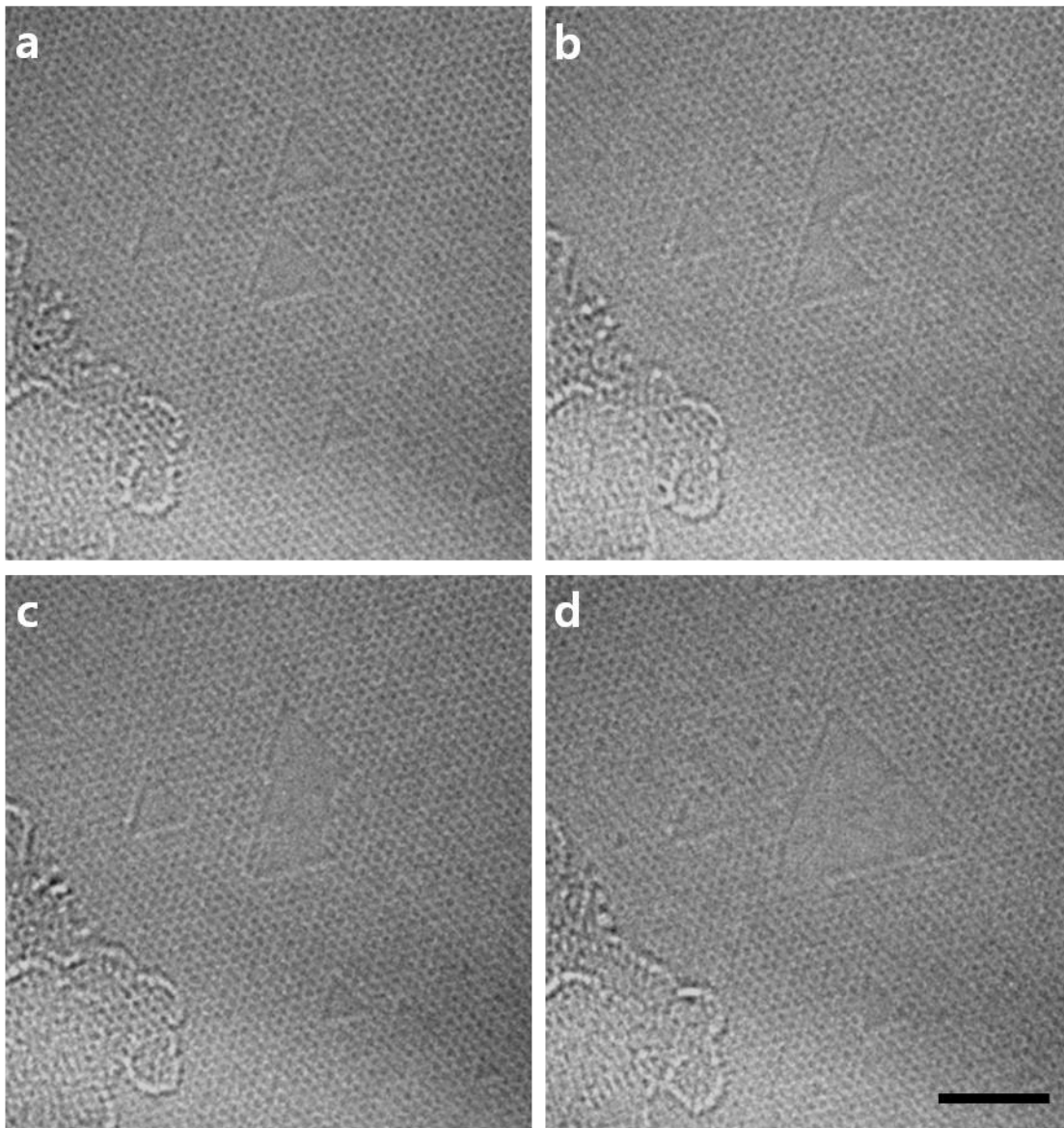
Figure 13. A series of sequential atomic resolution images of monolayer hBN showing how the merging of two holes ultimately maintains a triangular shape. Scale bar, 2 nm.

During these studies, it was noted that B and N atoms were often ejected as bundles as opposed to individual atoms, between successive imaging time intervals (~0.5 sec), at least under the experimental conditions used. Since atom movement is faster than 0.5 sec, DFT calculations and MD simulations were performed to gain additional insight into this process. A summary of the calculated bond lengths between various atoms in and near a triangular hole in hBN is shown in Figure 14. Note that the calculated B–N bond lengths measured perpendicular to the hole edge were longer than those found along the hole edge (c.f., positions indicated by 6, 7 and 8 vs. positions indicated by 3, 4 and 5 in Figure 14a). Moreover, the difference in the calculated B–N bond lengths was found to be consistent regardless of the hole size. Hence, when a B and/or N atom is ejected, the B–N bonds perpendicular to the edge become weakened and thus are more likely to be broken upon further electron beam irradiation. The results derived from the DFT calculations were supported by MD simulations. As shown in Figure 14b, the breaking of a B–N bond perpendicular to a hole edge generated a chain of B and N atoms as indicated by the yellow dotted box. The chain then became detached and was subsequently knocked off as a bundle of atoms, as indicated by the green dotted box.

Direct evidence of single chain formation, as supported by DFT calculations and MD simulations, was observed by AR-TEM in Figure 14c-f. Electron beam irradiation of the triangular hole (Figure 14c) resulted in the formation of a single chain comprised of B and N atoms (Figure 14d). The chain detachment process appeared to originate from the breaking of a B–N bond perpendicular to a hole edge. The chain was found to fluctuate in position (Figure 14e) before being finally knocked off (Figure 14f). Based on these observations, B and N atoms do not appear to be ejected individually; rather, B–N bonds perpendicular to a triangular hole edge may break first, resulting in the formation of a single chain of atoms that is ultimately removed. Compared to the B and N atoms found within the lattice of hBN, single chains containing the two heteroatoms are relatively unstable and, under the experimental conditions used here, are readily removed.
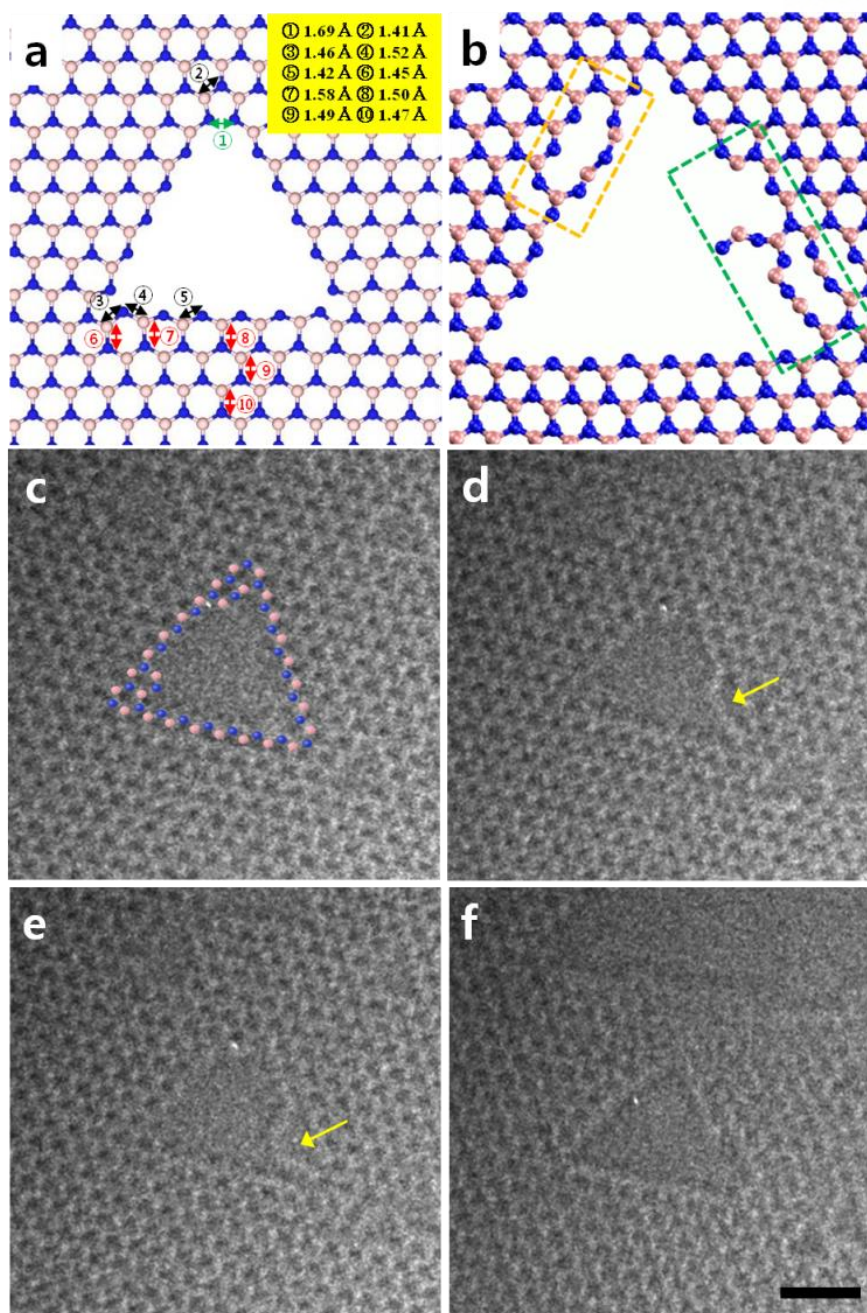
Figure 14. A summary of DFT calculations, MD simulations, and AR-TEM of hole growth processes in monolayers of hBN. The blue dots represent N atoms whereas the red dots represent B atoms. **a**, Calculated bond lengths between various atoms in a triangular hole. **b**, The B–N bonds perpendicular to the hole edge are broken first and often bundles of atoms are then knocked off. **c-f**, A series of AR-TEM images taken over time. The images show the formation of a single chain followed by its fluctuation in position and ultimate removal. Scale bar, 1 nm.

To gain additional insight into the properties of single chains comprised of B and N atoms, efforts were directed toward determining whether single chains were formed during the merging of multiple holes. A series of consecutive TEM images that captured the merging of two holes is shown in Figure 15. In general, such processes are too fast to be captured by TEM, as atoms are often ejected and/or are repositioned faster than the time elapsed between images; however, adsorbates can pin the hole and thus facilitate the capture of an intermediate state. As shown in Figure 15d, the merging of two holes resulted in a temporal bright contrast line, which may be due to the local fluctuation of the corresponding hBN edges and/or an accelerated ejection rate. Subsequent spreading of the fluctuating region resulted in the formation of single chains of B and N atoms inside the hole (Figure 15f) followed by the development of two triangular holes (Figure 15g). Loops and stretched chains containing a series of alternating B and N atoms were also observed (Figure 15h-k). Collectively, these observations indicate that single chains comprised of B and N atoms may be formed when holes in hBN coalesce. Note that some of the brighter spots at the edge of the triangular holes may be due to Si atoms. Although the materials described herein were not subjected to further chemical analysis, there does not appear to be any metal residue during the synthesis or transfer processes. Moreover, Si atoms are commonly observed in materials synthesized via CVD in quartz vessels. I conclude that the Si atoms may move around freely on the surfaces of hBN, but do not contribute to any hole growth. This conclusion was based in part on a report indicating that pure Si is unlikely to exhibit drilling or etching behavior in graphene. Apart from silicon or other metal atoms, oxygen containing species may contribute to hole formation mechanism because there are much oxygen and water vapor inside TEM even in UHV condition. To avoid oxygen-mediated etching effect, defect-free regions where oxygen is hard to attach are carefully selected and observed from the start of forming a monovacancy. As electron beam is continuously irradiated on the hBN sheet as hole grows, oxygen atom may not be able to cling to the defect site of hBN. Therefore, only the knock-on damage is addressed in hole forming mechanism in this study. Even though a careful selection of defect-free regions, residual oxygen inside TEM may contribute to the hole growth speed or atoms migration. But the triangular hole shape was constantly maintained all in the experiments in any condition.
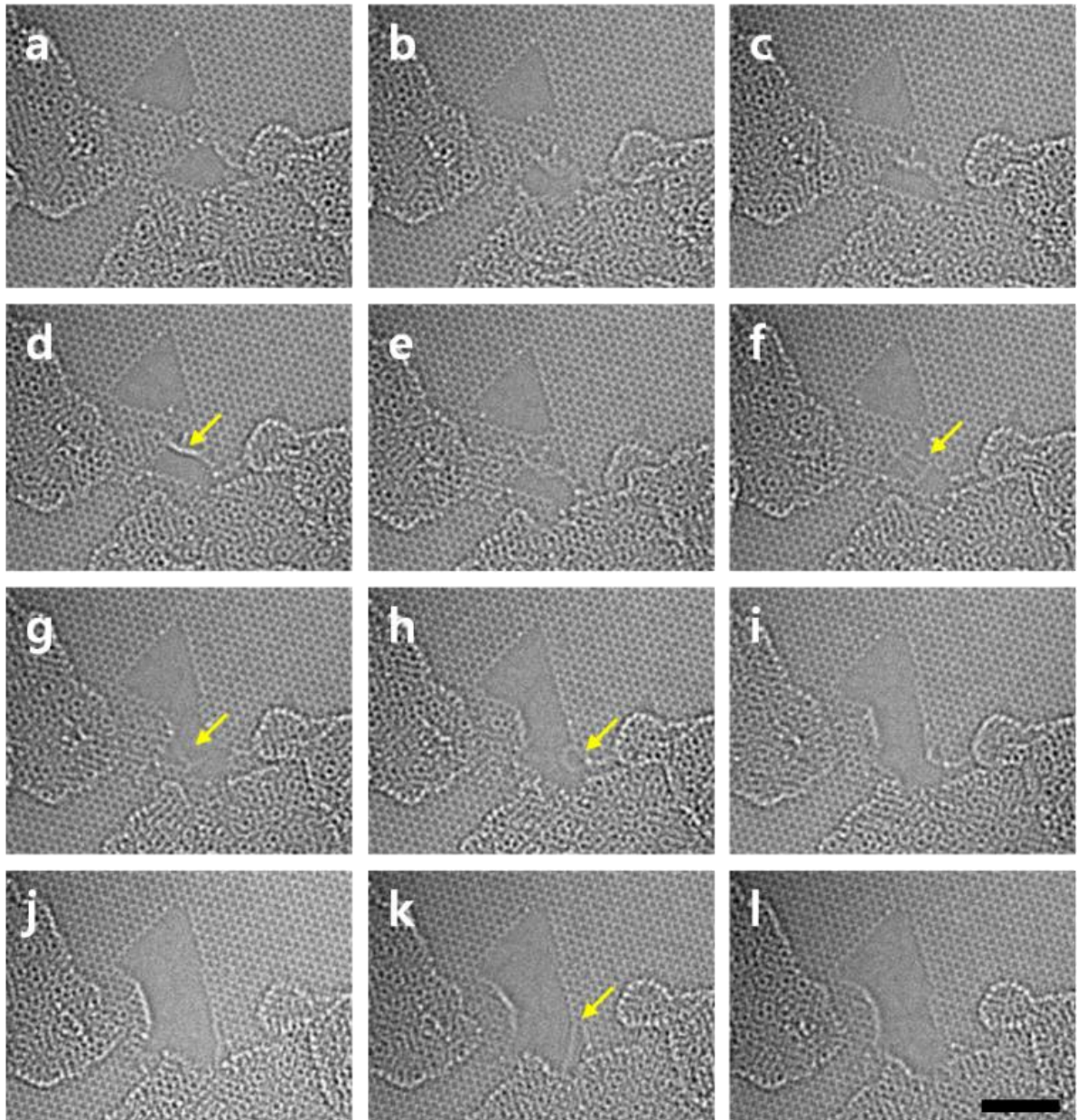
Figure 15. A series of TEM images showing how two triangular holes merge in a monolayer of hBN. The yellow arrows indicate single chains or loops containing B and N. Scale bar, 2nm.

As indicated in Figure 16, the migration of atoms along the edges of the holes in hBN was also evaluated over time. Although the B and N atoms may be predicted to move faster than the sampling time required for sequential imaging, a series of meta-stable configurations at the hole edges was observed. For example, the blue arrow in Figure 16b points to a series of missing B and N atoms sites whereas subsequent migration changed the shape of the hole as indicated in Figure 16c. In an earlier study, it was reported that electron beam irradiation does not induce the migration of B and N atoms in hBN[129]; however, the data presented here clearly show that the migration as well as reconstruction of B and N atoms on monolayer hBN is possible. Although the adding atoms to the hole might be derived from adventitious carbon adsorbates, it is more likely that B and N atoms migrate because the number of adding atoms and missing atoms in hBN sheet are same and the distance between adding atoms and missing atoms is shorter than that between adding atoms and carbon adsorbates. As such, holes may not grow but may become filled, at least partially, by the migration of B and N atoms over time. Collectively, these observations differ from those obtained with graphene. In graphene, various hydrocarbon adsorbates adhere to the surface and carbon impurities are often abundant so that the addition of carbon atoms to holes and/or migration is relatively more likely to occur under electron beam irradiation. While the lack of B and N sources intrinsically limits the addition of such atoms to holes in hBN, the migration of such atoms does appear to occur, albeit infrequently.
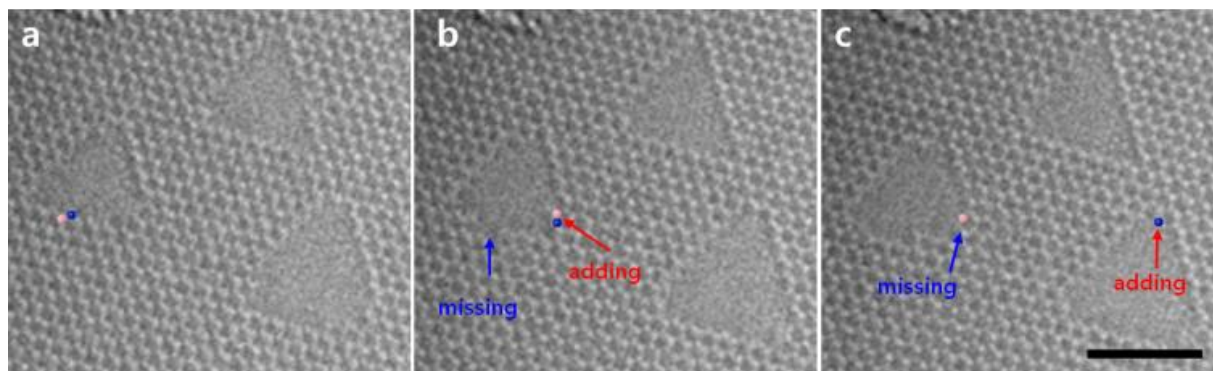
Figure 16. A series of TEM images of triangular holes produced by the prolonged irradiation of hBN. The blue dots represent N atoms whereas the red dots represent B atoms. The migration of the B and N atoms is observed over time. Scale bar, 2 nm.

3.4. Conclusion

The growth of triangular holes in hBN monolayers was observed using sequential AR-TEM imaging. When a monolayer of hBN was subjected to electron beam irradiation, a vacancy formed initially and grew while maintaining a triangular shape. Such shapes were observed even when such holes merged. Through a series of TEM images that were supported by DFT calculations and MD simulations, the mechanism for the growth of these holes appeared to involve the ejection of B and N atoms near the centers of the hole edges and also the ejection of bundles of atoms. Such processes involve the breaking of B–N bonds perpendicular to the hole edges and result in the formation of single chains containing B and N atoms. Multiple chains containing B and N were also observed when two holes merged together, while previous studies have focused primarily on the observation of a single chain of C atoms in holes in graphene. Moreover, the migration of B and N atoms in monolayers of hBN was observed using AR-TEM, as indicated by edge reconstruction, although such phenomena occur less frequently when compared to analogous carbon-based materials (i.e., graphene).

Chapter 4. Screw dislocation-driven growth of double-spiral hBN

4.1. Introduction

HBN has emerged as a critical building block for 2D heterostructured devices in which hBN serves as a substrate, electron barrier, or passivation material[130-132]. The controllable and large-scale synthesis of hBN films for use in scalable electronic devices has been achieved using CVD on various catalytic metals[83, 133-135]. Among metal substrates, Cu is most commonly used because of its abundance and its closely matched lattice constant with hBN that enables epitaxial growth, resulting in relatively high-quality films[136-137]. It also facilitates hBN growth by catalyzing the decomposition of BN precursors[138-139]. Furthermore, the relatively low solubilities of B and N in Cu allow a more controllable surface-mediated growth[135]. Planar and lateral growth has been observed in many studies for the first layer of hBN[135, 140-141]. A monolayer domain then nucleates on the Cu surface and grows laterally by the attachment of BN atoms to its edges. Following the Wulff construction, the resulting 2D single crystals often adopt well-defined shapes, e.g., triangles[135, 141] and hexagons[140, 142], depending on the edge attachment energies and the chemical potentials of the constituent elements[143-145].

As reported in previous studies, the growth of hBN does not cease after the formation of a monolayer[135, 142]. However, a complete study of the growth mechanisms of multilayer hBN films has not yet been made. Only a few studies have discussed further growth processes. In one of the first studies on monolayer hBN grown on Cu, Kim et al. reported that the growth was not self-limited and multilayer islands were observed after extended growth periods[135]. They concluded that the growth mechanism changed to the Stranki–Krastanov model (island on layer) after the completion of the first layer. In contrast, based on the *in situ* observation of Cu lattice expansion during hBN growth, Kidambi et al. proposed that the second hBN layer grows beneath the first layer in an inverted wedding cake structure formed by the incorporation of B atoms into bulk Cu[146]. Ji et al. grew few-layer hBN domains and proposed that the growth of the subsequent layers originated from the same nucleation center as the monolayer domain thereby suggesting that growth of multilayers may be caused by defects[147], similar to previous reports on graphene adlayers[148-151]. Here I show that multilayer hBN islands can also be formed from screw dislocations at APB[6, 152-153]. Unlike the single-spiral screw dislocation-driven growth in nanoplates and other 2D materials[154-158], a pair of screw dislocations always exist along an hBN APB resulting in a double-spiral structure for isolated islands. Strained boundaries, a consequence of merged adjacent multilayer islands when the screw dislocations propagate in opposite directions, were commonly observed. Using a combination of TEM and DFT calculations, I propose what are the most stable strained features such as width, magnitude, and direction between spiral clusters at the atomic scale.

4.2. Experimental Section

Synthesis of multilayer hBN spirals. hBN was grown on resolidified Cu by CVD at atmospheric pressure[142]. W foil (Alfa Asear; product no. 10417; thickness = 50 μm) was used as a supporting substrate for the Cu. Three pieces of Cu foil (Alfa Asear; product no. 13382; thickness = 25 μm) were cut to 2 cm × 1.5 cm and placed on top of the W foil. The stack was then loaded into a 1-inch quartz tube. The temperature of the furnace was first increased to 1000°C in 50 min and then to 1090°C in 10 min under a constant Ar/H_2 flow (200:5 sccm). Subsequently, the temperature was maintained at 1090°C for 30 min and then gradually decreased to 1075°C at a rate of 1°C/min. For hBN growth, ~8 mg of ammonia borane (Sigma Aldrich, 97%) was placed in a ceramic boat upstream of the heating zone and heated at ~85°C using a heating belt for 30 min. After the growth, the temperature was quickly decreased by opening the lid of the furnace.

TEM characterization of the hBN spiral structure. CVD-grown multilayer hBN was directly transferred onto a TEM grid[159]. TEM analysis was conducted on an aberration-corrected TEM (FEI Titan[3] G2 60-300) operated at 80 kV. Atomic resolution was successfully obtained at −21 μm ± 0.5 μm of spherical aberration (C_s) using a monochromator. The AR-TEM images were acquired with an exposure time of 0.2 s and an electron dose of approximately 5×10^5 e$^-$ nm^{-2}s^{-1} (8 A/cm^2). The DF-TEM images were taken from a second-order diffraction spot to identify the multilayer structures because the intensity of the SAED and DF-TEM images improves with increasing number of layers when multilayers are stacked with high symmetry such as AA′ or AB stacking[160-161]. An objective aperture with a radius of 1.28 nm^{-1} was placed on the back focal plane of the diffraction spots to collect electrons diffracted from the crystallographic plane of interest.

TEM image processing and simulations. For better visualization, some DF-TEM images were colorized by a lookup table using ImageJ. TEM image simulation was implemented in MacTempasX under experimental imaging conditions.

Computational modeling. The DFT-based calculations within the VASP[119-120] were performed to optimize the AA′-stacked hBN. The electronic exchange and correlation were described by the Perdew–Burke–Ernzerhof[162] functional in the generalized gradient approximation. The interaction between the valence electrons and ion cores was embodied in the projected augmented-wave method[163-164] with a cutoff energy of 400 eV. The Grimme DFT-D2 method[165] was used to modify the contribution of interlayer interactions. A supercell volume of $2.50 \times 108.40 \times 20.00$ Å^3 made the vacuum space sufficiently large to void image interference. Accordingly, 9×1×1 k-points were uniformly sampled in the Brillouin zone using the Monkhorst–Pack method[166] to ensure an energy convergence of less than 0.1 meV/atom. For simplification, the following optimizations and deductions are based on bilayer hBN: the bottom layer was fixed, and a uniformly distributed shear was imposed along the zigzag direction on the top layer. This is in accordance with the experimental observations. The shortest dislocation

length along the zigzag direction was one periodic unit (i.e., 2.50 Å). All structures were optimized using the conjugate gradient algorithm until the convergence reached 0.01 eV/Å.

4.3. Results and discussion

4.3.1. Synthesis and characterization of double-spiral hBN.

Self-aligned monolayer hBN films with multilayer islands were grown on resolidified Cu by atmospheric pressure (AP) CVD. In the scanning electron microscopy image (SEM) shown in Figure 17a, hexagonal multilayer islands are easily distinguished by their bright contrast. Multilayer islands tend to grow along defect lines (white lines in Figure 17a) with some as isolated individual islands while others are clustered and merged. The microstructures of these multilayer islands were elucidated using DF-TEM and AR-TEM. The DF-TEM image in Figure 17b reveals all the hexagonal multilayer islands grown along the defect lines are spiral-shape islands; an isolated multilayer island has a double-spiral structure while more complex spiral structures are formed when multiple islands are situated close together and merge along the defect lines. The one set of hexagonal diffraction spots (inset of Figure 17b) indicates that all the monolayer hBN domains and multilayers in Figure 17b share the same orientation. While, the spiral contours of the multilayer islands are divided by defect lines, which means these defect lines are APBs that are created where two monolayer domains having different polarities, i.e. [BN]/[NB] (60 ° rotation angle difference), meet (Figure 18). I demonstrated that hBN monolayer single crystals grown by CVD primarily have the same orientation and comprise both [BN] and [NB] domains, with defect lines along the APBs[142]. Also note that the isolated spiral islands tend to be bigger in lateral size (~1 μm) than clustered ones and their hexagonal edges are usually aligned to the zigzag direction as verified by the orientation of diffraction pattern (inset of Figure 17b). This indicates the presence of alternating B- and N-terminated edges[140]. Whereas, clustered spiral islands show slightly mixed edges where they merge. Both left- and right-handed spirals were observed and found up to 7 layers as far as I have searched.

Figure 17c shows an AR-TEM image at the interlayer boundary region of a double-spiral multilayer island as indicated by the red box in Figrue 401b. The number of hBN layers was determined by etching the layers by prolonged electron-beam irradiation. The left and right regions were determined to be two and three layers respectively, confirming that the number of hBN layers increases by one for each rotation. The interlayer boundary was identified from the intensity profile (Figure 17d) across the blue line shown in the AR-TEM image in Figure 17c. Fast Fourier transforms (FFTs) of the bilayer and trilayer regions (insets in Figure 17c) indicate the same hexagonal structure with no difference in orientation. The layer boundary has zigzag termination as suggested earlier in Figure 17b that spiral islands grow along the zigzag direction. The stacking structure was evaluated from the orientation of

the triangular defects created by electron beam irradiation. Since the triangular hole defects of hBN have N-terminated edges[88, 167-168], the opposite orientation of the triangular defects between adjacent layers indicates that the hBN layers were AA′-stacked (i.e., [BN]/[NB]/[BN]/[NB]; Figure 1E), which is the most energetically favorable stacking configuration in bulk hBN (37-38). The above analyses suggest that the double-spiral multilayer island was formed with AA′ stacking with two intertwined hBN domains, which spiral around each other one layer per step across the APB.
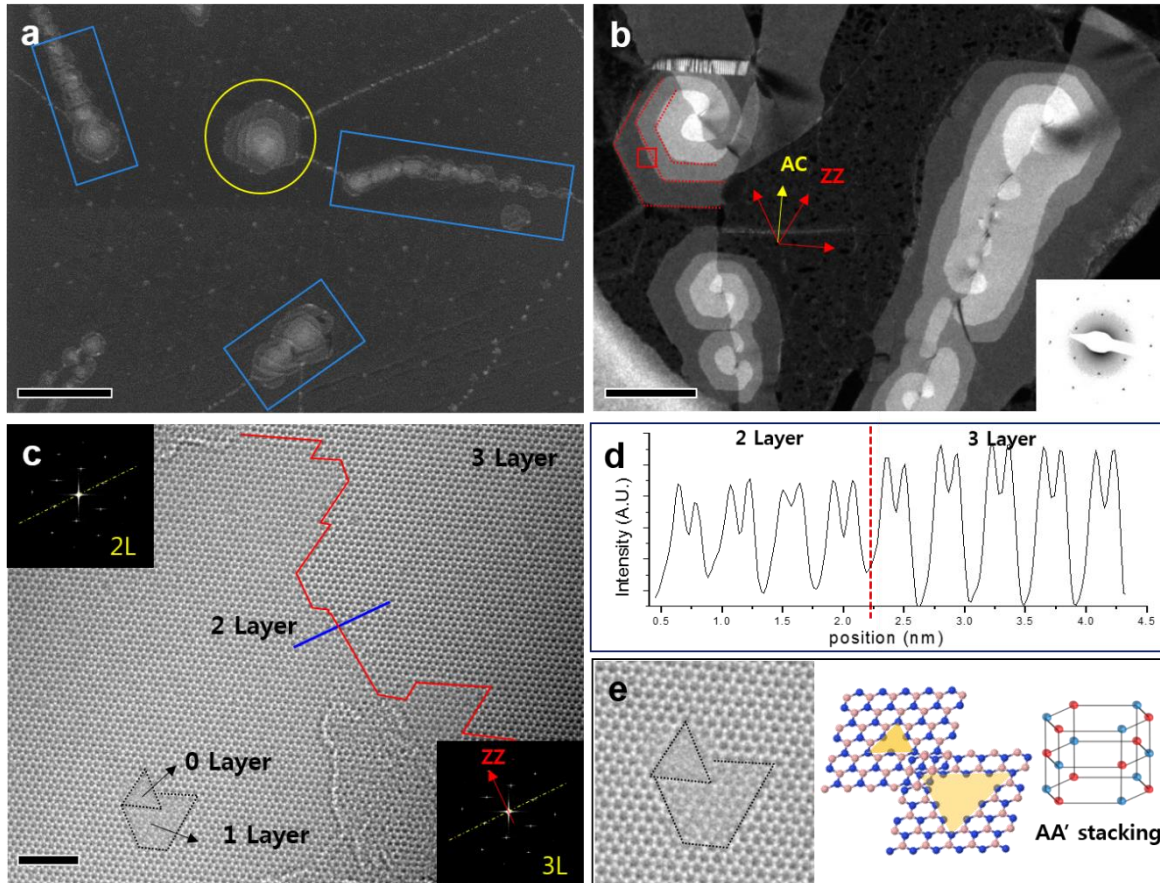
Figure 17. Spiral growth of multilayer hBN islands. a, SEM image of multilayer hBN islands grown on a resolidified Cu substrate. Both isolated (yellow dotted circle) and clustered (blue dotted rectangles) spirals exist along defect lines in monolayer hBN. **b**, DF-TEM image showing the spiral structure of the hBN islands. The islands have a double-spiral structure along APB. The inset shows the SAED pattern of the entire area of (**b**). **c**, AR-TEM image of the area indicated by a red square in (**b**). The red dotted line represents a layer boundary. Insets are FFTs over bi- and tri-layer region, respectively. **d**, Intensity profile along the blue line in (**c**). One layer increases for each spiral contour. **e**, The opposite direction of an electron beam-induced triangular hole defect in the neighboring layers demonstrates the AA′ stacking configuration of multilayer hBN. Scale bar (**a**), 1 μm. (**b**), 0.2 μm, (c), 2nm.
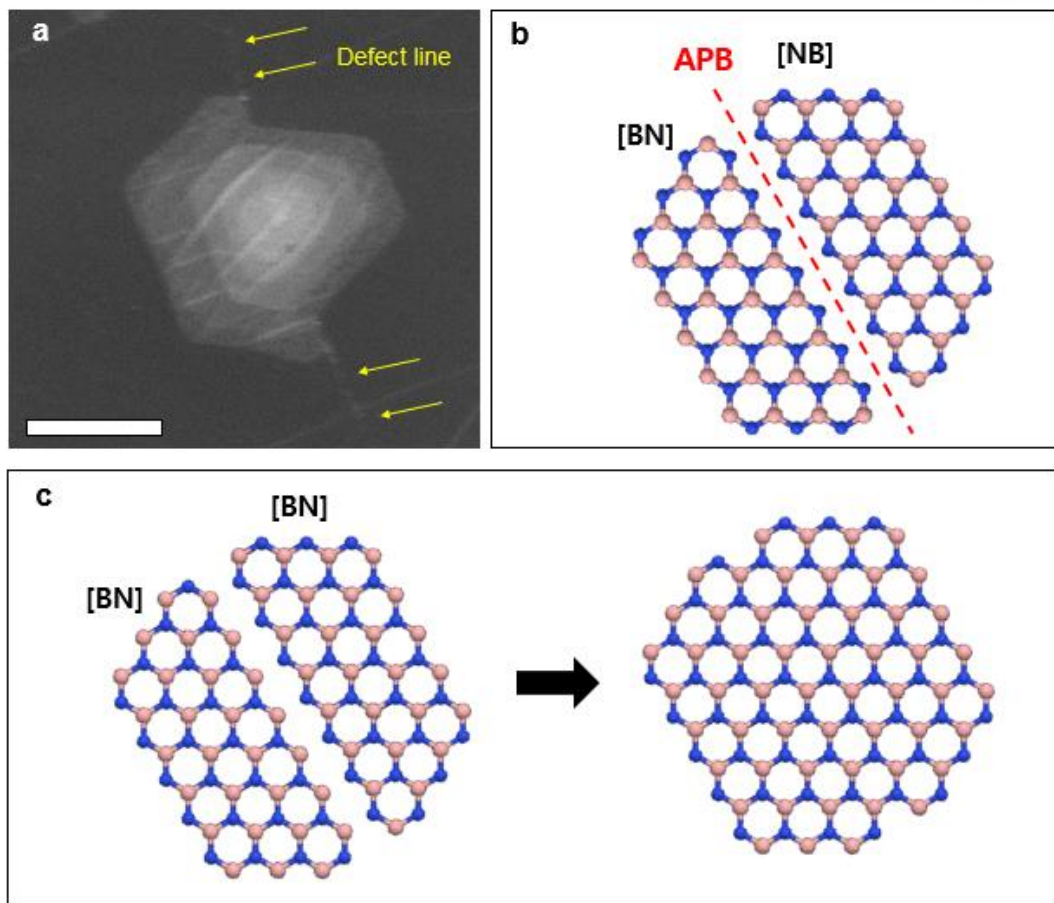
Figure 18. Multilayer hBN islands grown along APB. Contrast to seamless stitching of [BN]/[BN] (or [NB]/[NB]) domains, coalescence of [BN]/[NB] domains leaves defect line. The boundary of [BN]/[NB] is called APB. Scale bar, 1μm.

4.3.2. Growth mechanism of screw dislocation-driven double spiral hBN.

Based on the results of TEM characterization in Figure 17, the mechanism for the double-spiral growth of isolated multilayer islands is inferred. Figure 19a shows a false-colored DF-TEM image of an isolated double-spiral multilayer hBN island which is schematically depicted in Figure 19b showing the layer numbers and the domain orientations. The formation mechanism of double-spiral hBN multilayers is illustrated in Figure 19c. At first, monolayer domains nucleate and then grow epitaxially along the (110) Cu surface by edge attachment (EBSD shows that the resolidified Cu has a surface orientation of (110)). Because of the prolific nucleation of hBN, there are numerous instances where the edges of neighboring domains meet. If domains coalescence with the same polarity ([BN]/[BN]), they can stitch seamlessly together, while those with different polarities ([BN]/[NB]) cannot, leaving exposed edges and an APB instead. When the APCVD growth of hBN continues after the monolayer has fully covered the Cu surface, an abundance of multilayer hBN spiraling islands is formed along the APBs, where a pair of dislocations is initiated and causes the hBN domains to simultaneously grow and extend over each other. Growth progressed by spiraling in the vertical direction as the BN atoms attached to the active edges, leaving slipped planes in the bottom layer (i.e., generating screw defects). Once each spiral reached the domain boundary, another layer grew on top of the existing one. This process continued perpetually. TEM observations have shown that the spirals climbed one layer per step, which is equivalent to one elemental Burgers vector of hBN. Because the top layer was the last to form and had the least time to grow, the multilayer islands formed pyramid-like structures in which the layers became progressively smaller while moving toward the top (Figure 19d). Each of the two spiraling domains grew independently across the boundary and retained its orientation, thereby maintaining the energetically favorable AA′ stacking at each side of domains to the APB. This is possible because of the unique double-spiral system that was initiated at the APB. Although spiral growth has been observed in other 2D materials, including graphene[154], molybdenum disulfide[155-156], and tungsten diselenide[157], the growth process in these materials usually involves a single screw dislocation. In these cases, AA-like stacking configurations (which means AA, or AB, or with translation but not twisted in-between layers) were formed in a single spiral because the crystal orientation remained unchanged.
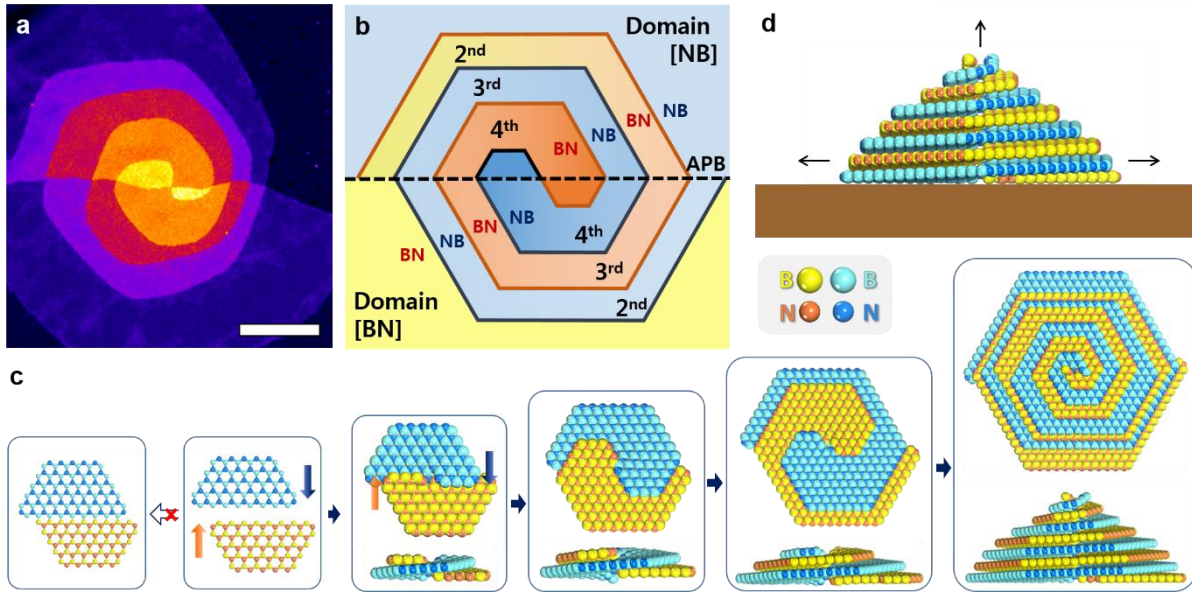
Figure 19. Growth mechanism of hBN spirals. a, False-colored DF-TEM image of multilayer hBN with a double-spiral structure along the APB (scale bar, 0.2 μm). **b,** Illustration of (a) with information of the number of layers and domain orientations. **c,** Illustration of growth mechanism of hBN spirals. **d,** Side view of top growth of multilayer island from the substrate.

Furthermore, it is verified that the spiral islands grow upward from the initial monolayer by spiraling around the axial dislocation located at the APB as BN atoms are attached to the active edges. It is experimentally demonstrated by comparing the orientations of triangular defects on each side of domains to 2|3 layer boundary as shown in Figure 20. This demonstration is possible due to the characteristic behavior of hBN defect growth under an 80 kV electron beam. (1) Under an 80 kV electron beam, atoms are knocked out leaving an N-terminated triangular hole defect[88, 167-168]. Hexagonal hole defects with B-terminated edges can be created at elevated temperature[169] or at higher current density[170], but in the TEM image condition it is confirmed that N-terminated triangular hole defects are always created with TEM image simulations using MacTempasX. (2) Since hBN has an AA′ stacking structure, the orientation of the triangular defects are rotated 180 ° between layers (refer to the schematic in Figure 17e). (3) Atoms are normally ejected from the bottom layer first, and the triangular defects grow layer by layer. Therefore, the smallest triangular defects are found in the top layer[87]. Based on these characteristics of electron beam-induced hBN defects, triangular defects for both top and bottom growth are illustrated in Figure 20. Note that the hBN layers are turned upside down when transferred onto the TEM grid (Figure 20a) by a direct transfer method[159]. Figure 20b, c show the features of the triangular defects corresponding to top and bottom growth, respectively, including the layer boundary of the double layer and trilayer, for a comparison of the orientation of the triangular defects in the AR-TEM image in Figure 20d. As illustrated in Figure 20b, c, the orientations of the smallest triangular defect on the left and right of the layer boundary should be the same as that in the case of top growth and opposite in the case of bottom growth. In Figure 20d, the empty regions with no atom contrast after the top layer is etched out are marked as purple triangles. The orientations of the purple triangles over the layer boundary are the same, which proves the top growth of hBN layers. There are exceptions such as small vacancies possessing the opposite orientation to the others like the green triangle marked in Figure 20D because of sputtering caused by the large momentum transfer so atoms exit the surface in the forward direction[87], but this is very rare.

Therefore, unlike bottom growth caused by the substrate's catalytic effect, which results in the "inverted wedding cake" structure and is commonly found in few-layer graphene[148-151], growth by screw dislocations occurs by a top growth mechanism in which the growth extends from the first layer and spirals upward around an axial dislocation, forming multiple layers of perpetuating steps, which agree to my recent study of spiral growth in graphene[171].
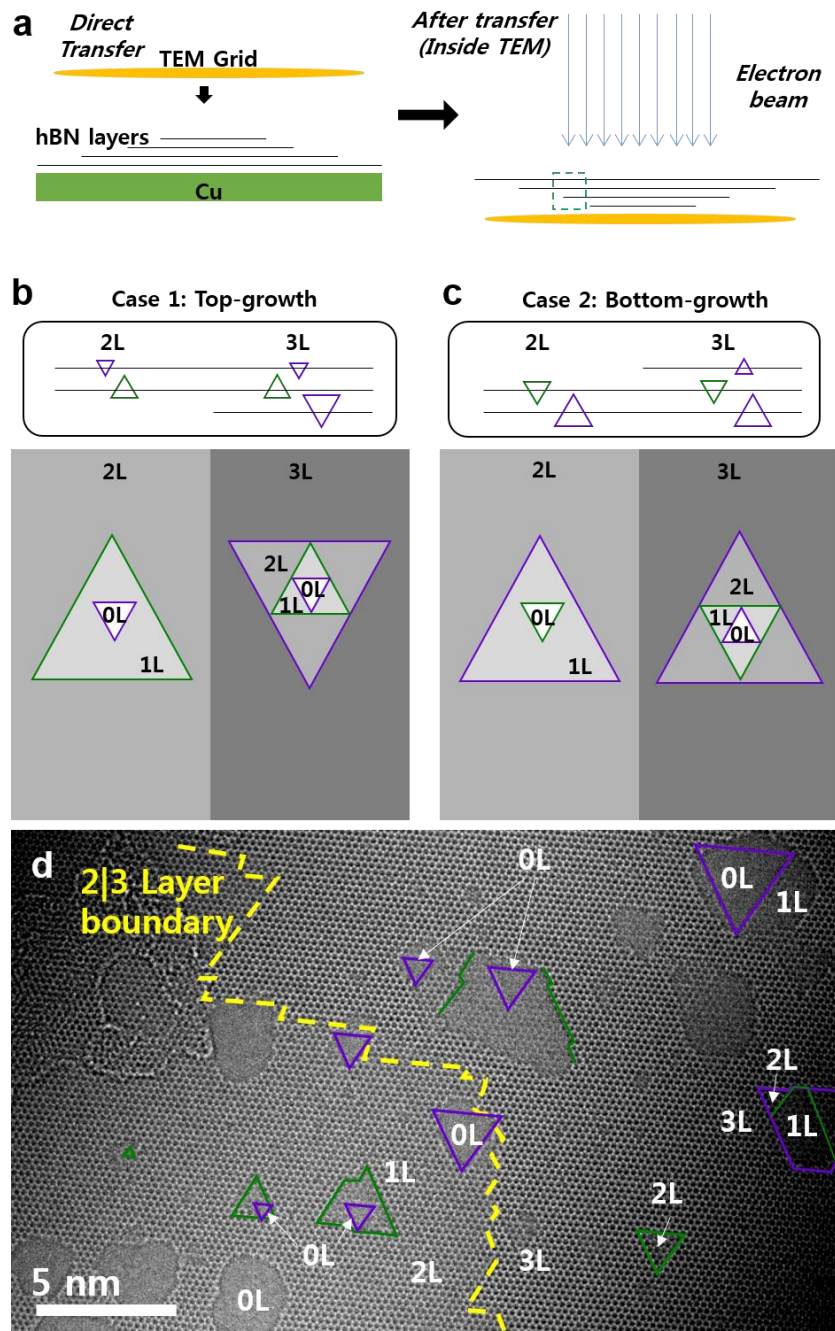
Figure 20. Top growth of hBN spirals. a, Schematic of multilayer hBN grown upward from the Cu substrate. The hBN layers are turned upside down after being transferred onto the TEM grid. **b,c,** Schematic showing the features of triangular defects for top growth (**b**) and bottom growth (**c**). **d,** AR-TEM image with triangular holes formed by prolonged electron beam irradiation. The image shows the area indicated by a red box in Figure 1b and corresponds to the area indicated by a green dashed box in (**a**). Scale bar, 5 nm.

4.3.3. Shear strain between hBN spiral clusters.

Typically, hBN spiral islands cluster along defect lines as a result of the many screw dislocation sites situated along the APBs (Figure 17a). Interestingly, these clusters exhibited different features, as observed in the DF-TEM images in Figure 21a, b. Some clusters were smoothly connected (Figure 21a), whereas others showed dark lines in between merged multilayer regions (Figure 21b). The DF-TEM images in both Figure 21a, b were acquired by selecting a second-order diffraction spot in the SAED pattern. This should result in increased intensity of the DF-TEM image with increasing number of layers when the layers are well ordered without misorientation (AA′-stacked) by constructive interference of waves between layers[160-161]. Hence, the dark lines in Figure 21b indicate strained regions that have lost the high-symmetry stacking configuration (not AA′-stacked). The absence or presence of these dark lines in Figure 21a, b are related to the rotation direction of neighboring islands. When two neighboring islands grow in opposite spiraling directions (i.e., one left-handed and one right-handed), they coalesce smoothly because the encountering screw dislocations propagate in the same direction (Figure 21c). However, when they have the same spiraling direction (i.e., both are right- or left- handed spirals), the counter-directional propagation of screw dislocations at the merging region results in a strained boundary between them (Figure 21d), from the APB to merging apex.
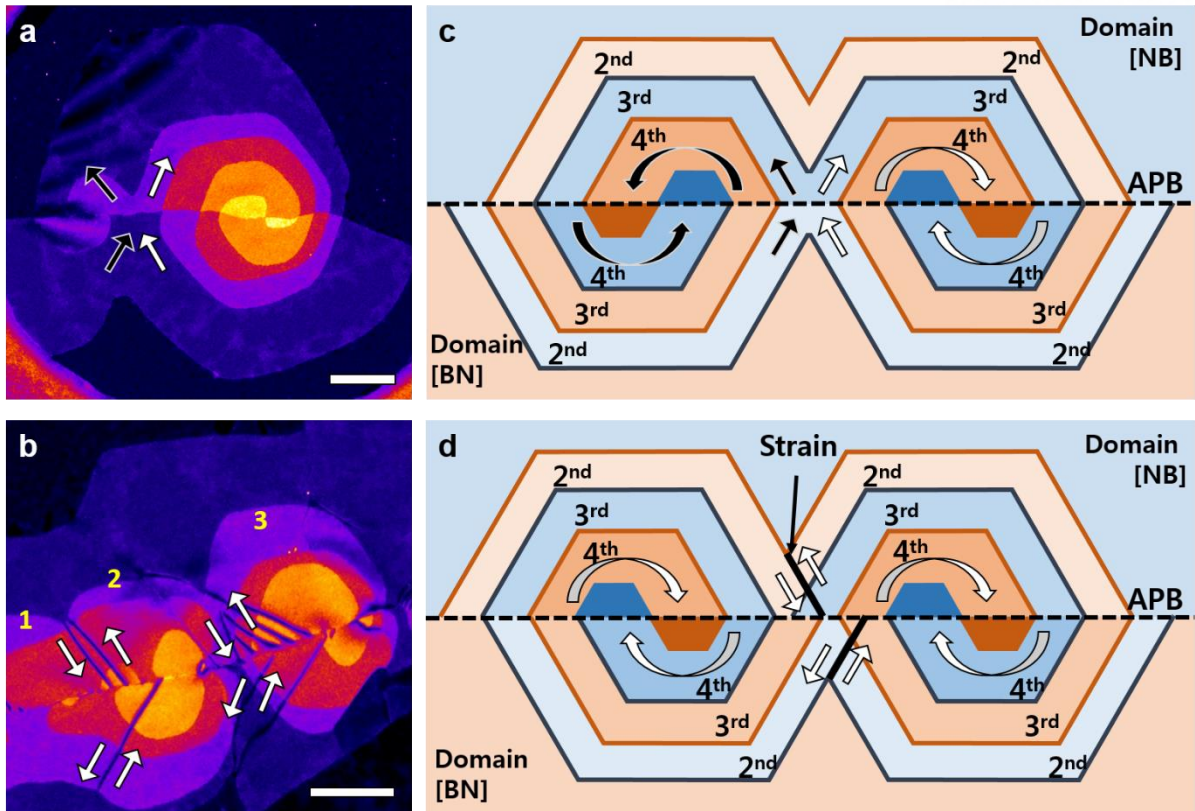
Figure 21. Merging of hBN spirals and creation of strain. a, b, False-colored DF-TEM images of spiral clusters. Two islands smoothly merge in (**a**), whereas dark lines are formed between the merging regions of three islands in (**b**). **c, d,** Schematics showing the merging of two islands: (**c**) is for the case in (**a**), where the two spirals have opposite directions (right- and left-handed spirals) and (**d**) is for the case in (**b**), where the two spirals have the same direction (both left-handed). The right- and left-handed spirals are represented by black and white curved arrows, respectively, and the propagation directions of the screw dislocations are indicated by an arrow with the same color of the corresponding spiral direction. The black dashed lines are the APBs formed between the [NB] (blue) and [BN] (orange) domains. The solid black line indicates strain applied in-between two merging spiral islands. Scale bar, 0.2 μm.

The regions with dark lines were further investigated at in the TEM at the atomic scale. An AR-TEM image of the white rectangular area including a dark line in Figure 22a is shown in Figure 22b. A strained region along the zigzag direction was observed, as indicated by the red dashed lines. The FFT (inset of Figure 22b) shows only one set of hexagonal diffraction spots, indicating that the strained structure was caused by a gradual shift in the relative atomic position between layers with no interlayer twisting[172]. Figure 22c shows a magnified atomic resolution image within the area indicated by a cyan rectangle in Figure 22b. The square pattern observed in the center of Figure 22c gradually becomes 'wiggly' moving away from the center before returning to the stable hexagonal configuration. By fitting the atomic models with different widths and magnitude of the shear strain (Figure 23 and Figure 24), I replicated the experimental dimensions of the strained region using a shear strain value of 1 unit cell of hBN (2.50 Å) on the upper layer of AA′-stacked bilayer hBN, with a width of approximately 10 nm along the zigzag direction (Figure 22d). The simulated TEM image shown in Figure 22e closely resembles the experimental image. The strained region had a width of approximately 10 nm (including approximately 2 nm of square patterns, 4 nm of wiggly patterns, and 4 nm of slightly misfit hexagonal patterns), consistent with the width of the dark lines observed in the DF-TEM image (Figure 22a).
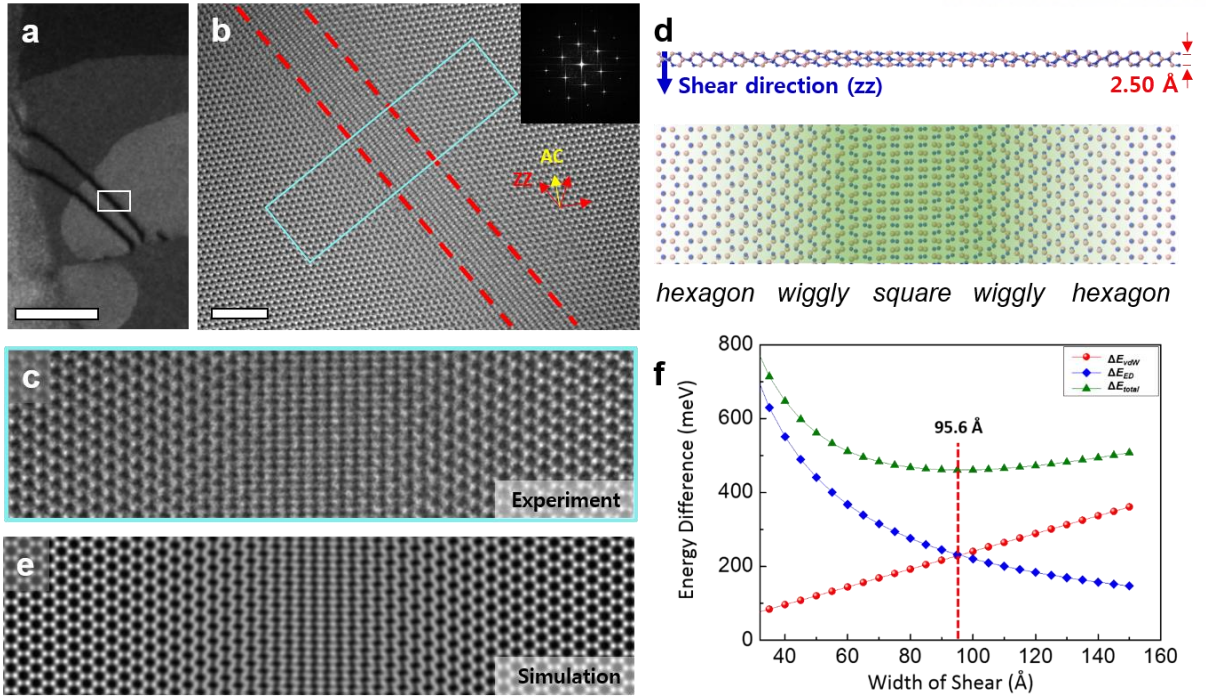
Figure 22. Shear strain in hBN spirals. a, DF-TEM image of strained hBN (strain displayed by dark lines). **b,** AR-TEM image of the area indicated by a white box in (**a**). The inset shows the FFT over the whole area. The region highlighted by the red dotted lines along the zigzag direction shows a square-like moiré pattern instead of the original hexagonal lattice of hBN with AA′ stacking configuration. **c,** Setting 1 hBN unit cell (2.50 Å) strength of shear strain along the zigzag direction makes similar feature with AR-TEM result of (**b**), including hexagonal, wiggle-like, and square-like parts over a width of ~10 nm. **d,e,** Magnified AR-TEM image (**d**) and simulated image of DFT calculations (**e**) from the structure in (**c**) are well matched together. **f,** The increase in total energy (ΔE_{total}) resulting from the shear strain depends on shear width. ΔE_{total} is minimized when the shear width is 9.56 nm. Scale bar (a), 1 μm, (b), 2nm.
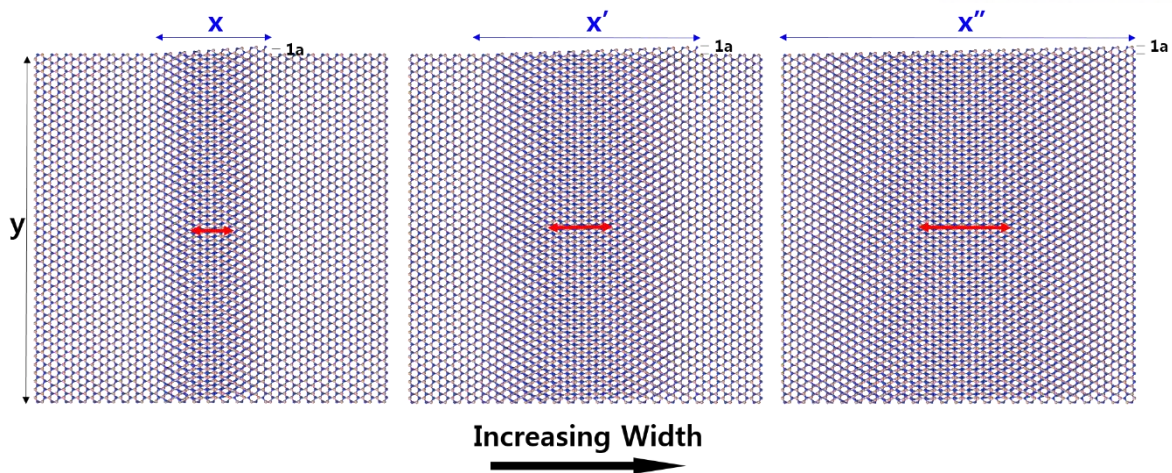
Figure 23. Relation between shear width and the width of the square-like region. "x" is the width where shear is applied in the hBN bilayer with fixed shear strength of 1 hBN unit cell (2.50 Å) in y-direction. The red arrows indicate the square-like region resulting from shear. Larger "x" results in a wider square-like region.
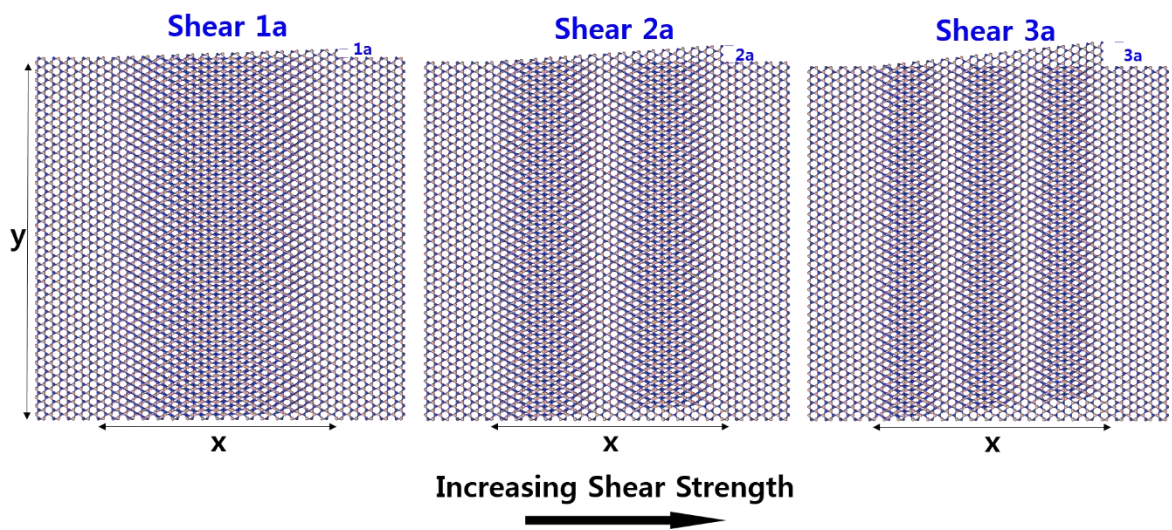
Figure 24. Relation between shear strength and the periodicity of the square-like region. The periodicity of square-like region increases per 1 hBN unit cell (2.50 Å) of shear strain in the y-direction. Shear width (x) is fixed for the three models.

To obtain the general value of shear strain in an hBN spiral, the total increase in energy was calculated for the shear of a 1 hBN unit cell in AA′-stacked hBN. In the most stable configuration of hBN (i.e., AA′ stacking), shear causes elastic deformation and the formation of other stacking sequences. Therefore, the increase in total energy is comprised of two parts: the change in elastic deformation energy (ΔE_{ED}) and the change in van der Waals interaction (ΔE_{vdW}) between adjacent hBN layers.

$$\Delta E_{total} = \Delta E_{ED} + \Delta E_{vdW} \tag{1}$$

ΔE_{ED} can be expressed as follows:

$$\Delta E_{ED} = G \times (a/b)^2 \times (h \times b \times a), \tag{2}$$

where G is the shear modulus, a is the length of the displacement of hBN along the zigzag direction, b is the width of the sheared region in the armchair direction, and h is the layer distance in hBN. Thus, (a/b) is the shear strain and $(h * b * a)$ is the effective volume of the sheared material (Figure 25).

The increase of total energy resulting from the vdW term (ΔE_{vdW}) could be written as:

$$\Delta E_{vdW}\Delta E_{vdW} = \alpha * b * a, \tag{3}$$

where α is the scaling factor, which is equal to the reduction in vdW energy per area.

Thus, ΔE_{total} can be obtained as follows:

$$\Delta E_{total} = G * a^3 * h/b + \alpha * a * b. \tag{4}$$

ΔE_{total} is minimized when $\frac{\partial \Delta E_{total}}{\partial b} = 0$. Therefore, the width of the sheared region at equilibrium can be expressed as follows:

$$b_{eq} = (G * h/\alpha)^{1/2} * a. \tag{5}$$

To calculate b_{eq}, the shear modulus G and the scaling factor α are estimated theoretically. The value G was obtained using the definition in Eq. (2). Four different supercells of hBN were designed. The lattice constants are listed in Table S1. All supercells had same a and h but different b because they had different periodic units along the armchair direction. Shear was imposed along the zigzag direction with a displacement of 2.50 Å, which is equal to a. The value of h was set as the interlayer distance of hBN (3.40 Å). By only adjusting b, different values of ΔE_{ED} were obtained using DFT calculations and determined the average value of G to be 1036.48 meV/Å^3.
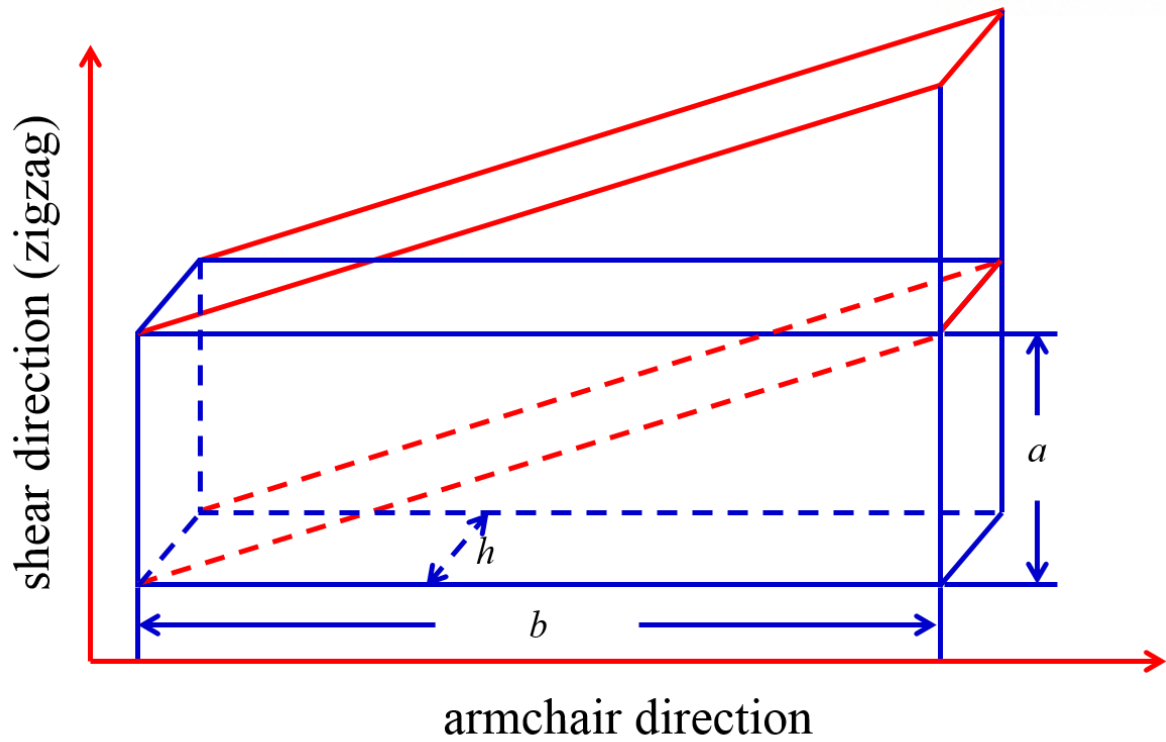
Figure 25. Theoretical model used to calculate the increase in total energy caused by shear strain in the hBN system.

Supercell		I_1	I_2	I_3	I_4
Lattice constant (Å)	a	2.50	2.50	2.50	2.50
	b	17.33	25.99	34.65	43.32
Shear modulus (meV/Å³)		1026.66	1036.74	1040.19	1042.34
Average shear modulus (meV/Å³)			1036.48		

Table 2. Lattice constants and shear modulus for the chosen supercells.

The scaling factor α represents the increase in energy per area caused by the reduction in the vdW interaction between adjacent hBN layers. To calculate α, a bilayer hBN containing a total of four N atoms and four B atoms is designed. The volume of the supercell was $2.50 \times 4.33 \times 20.00$ Å^3. The bottom layer was fixed, and the atoms in the top layer were slid in 0.1 Å steps until the distance was of a full hBN unit cell, 2.50 Å along the zigzag direction. The relation between the step distance and ΔE_{vdW} is shown in Figure 26.

The value of α can then be estimated as the average of the vdW energy difference with the step distance:

$$\alpha = \frac{\sum \Delta E_{vdw} * \Delta x}{\sum \Delta x} = 2.41 \text{ meV/Å}^2. \tag{6}$$

The dependence of ΔE_{total}, ΔE_{ED}, and ΔE_{vdW} on the width of the sheared region are shown in Figure 22f. Having obtained G and α, b in the equilibrium state can be estimated as follows:

$$b_{eq} = (\alpha \times h/\alpha)^{1/2} \times a = 95.6 \text{ Å} = 9.56 \text{ nm}. \tag{7}$$
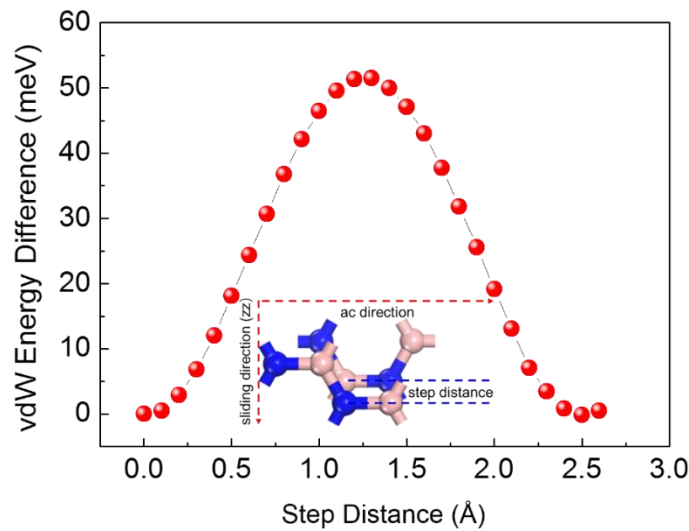
Figure 26. Relation between the vdW energy difference and step distance. The step increment is 0.1 Å. The inset shows the model used to calculate α.

Based on Eq. (3), the total increase in the energy attributed to the shear strain can be obtained from b, i.e., the width of the shear region (Figure 22f). The width of the shear region corresponds to the local minimum in total energy and was calculated to be 9.56 nm, which is in agreement with the experimental results and image simulation model (Figure 22d, e). This explains why many of the observed dark lines had similar widths (9–10 nm). Thus, the merging of hBN spiral islands grown from counter-directional screw dislocations induces a shear stress over a distance of 9.56 nm between the islands, generating moiré patterns in the AR-TEM image and dark lines in the DF-TEM image.

4.4. Conclusion

In this study, growth was carried out at atmospheric pressure with 200:5 sccm of Ar:H2 flow, potentially leading to the overgrowth at the exposed edges of APBs. Since the gas flow rate is higher to low pressure CVD, there are more collisions between the gas molecules/precursor leading to more active precursor species to be absorbed at the exposed edges of APBs. Furthermore, the growth was controlled by feeding small amounts of precursor (8 mg of ammonia borane heated at 85 °C) to the system, fostering low supersaturation conditions which enable the growth of multilayers by screw dislocation. According to the Burton–Cabrera–Frank theory, crystal growth is dominated by dislocations at low supersaturation condition[173-175]. And dislocations are also known to form along the grain boundaries of merged monolayer domains, especially APBs of aligned hBN domains in this case. Therefore, the spiral growth extends from the first layer as the BN atoms attached to the active edges of APBs, and grow upward spiraling around the axial dislocation in the vertical direction.

In summary, multilayered hBN spiral islands were grown along the APBs of aligned hBN on resolidified Cu substrates by APCVD at low supersaturation condition. Paired screw-dislocations initiated at the APBs resulted in intertwined spiraling hBN domains which climb one layer per step across the APB by growing from the active edges. The unique double-spiral structure means that the hBN multilayer preserves AA′ stacking configuration throughout the entire region unlike other 2D materials with a single spiral structure. Shear strains along boundaries between merged multilayer regions were commonly observed arising from neighboring islands with counter-directional screw dislocations. The strained regions, which are typically 9-10 nm wide, generate moiré patterns at the boundaries between adjacent multilayer spirals. This study provides understanding of the growth mechanism of spiral hBN multilayers and explains the shear strain between spiral clusters.

Chapter 5. Atomically sharp AA′/AB stacking boundary of hBN as one-dimensional conducting channel

5.1 Introduction

In contrast to the wide spectrum of proposed applications for graphene as an active component in nanodevices, hBN is often regarded as a passive material where the range of applications is largely confined to substrates or electron barriers for 2D material-based devices due to its electrically insulating feature with a large bandgap ~5 eV[176]. Many attempts to lower bandgap of hBN by substitutional doping (e.g., with carbon or oxygen atoms) have been mostly ineffective because of the strong covalent BN bonds and chemical inertness[177-179], while hBNC, in-planar compound of graphene and hBN synthesized by Gong et al. showed semiconducting property with tunable bandgap[29].

Stacking boundaries or phase boundaries of few-layer 2D materials were shown to possess unique properties which open new ways to control the performance of a material[4, 23-26]. For example, AB/BA stacking boundary with broad range in bilayer graphene showed insulating-like characteristics and reversible transport regimes[24], and 558 line defect formed at a stacking boundary in graphene was reported to act as a metallic wire[4]. One-dimensional twin boundaries found in tungsten diselenide[27], molybdenum diselenide[28] also revealed bandgap changes. In the meantime Li, Q. C. et al. reported Grain boundaries in hBN such as the 5|7 and 4|8 configurations reduce its bandgap to ~3.4 eV and ~4.3 eV, respectively[29]. However, there is no further report on few-layer hBN stacking boundaries. Although the most stable stacking structure in bulk hBN is AA′ stacking[98, 180], few-layer hBN can also exist as AB-stacked, which is the next-most stable configuration according to theoretical calculations[97] and have been experimentally observed in both chemically exfoliated[181] and synthesized hBN[99, 182].

Herein, one-dimensional hBN conducting channel at AA′/AB stacking boundaries of few-layer hBN grown by CVD was studied through a systematic analysis using TEM. Using a combination of DF-TEM and AR-TEM, both AB-stacked and AA′-stacked hBN regions were identified, enabling us to observe the boundary structure with atomic precision. The experimental TEM results were further complemented by image simulations, DFT calculations, and MD simulations to investigate the structural stability of specific stacking boundary configurations. The bandgap tuning of hBN with the atomically sharp twin boundaries was also confirmed theoretically and experimentally. In addition the formation mechanism of atomically sharp stacking boundaries was deduced by observations of extended Klein (EK) edges at the layer boundary of hBN.

5.2. Experimental section

Synthesis and transfer of hBN films. Cu foils (Alfa Asear, product no. 13382, 25 μm thick) was used as growth substrates for the hBN films. The Cu foil was first dipped into dilute nitric acid for a few seconds and then rinsed with deionized water. It was next loaded into a 1 in. quartz tube and placed within the heating zone of the furnace. The furnace was heated to 1050 °C for 40 min and kept constant for another 2 h to anneal Cu and remove the surface oxide under a constant Ar/H_2 flow of 200:20 sccm. After annealing the sample, 8 mg of an ammonia borane complex (Sigma-Aldrich, product no. 682098, 97%) was placed in a ceramic boat upstream from the quartz tube, outside the heating zone, and heated this compound at 85 °C to begin hBN growth. The typical growth time needed to achieve a complete hBN film over the entire Cu substrate was 30 min. After the growth of the film was complete, the lid of the furnace was lifted to allow rapid cooling. The hBN was then transferred onto the TEM grid using the direct-transfer method[159]. That is, the hBN/Cu was directly transferred onto a quantifoil TEM grid without Poly(methyl methacrylate) by sticking them by isopropyl alcohol, and then Cu was etched out in sodium persulfate overnight. The hBN transferred onto the TEM grid was rinsed and dried at ambient conditions.

TEM analysis. All TEM work was performed using an aberration-corrected FEI Titan Cube TEM (FEI Titan³ G2 60-300). The microscope provides sub-Ångstrom resolution at 80 kV with a monochromator and -21 ± 0.5 μm of spherical aberration (C_s). The DF-TEM images were taken from first-and second-order diffraction spots of the hexagonal lattice of hBN using an objective aperture of a 1.28 nm^{-1} for 10 s of acquisition time. The AR-TEM images were obtained in 0.2 s of exposure time at electron-beam densities around 5×10^5 e$^-$nm^{-2}. Individual atoms are imaged in white to get the actual atomic positions for direct interpretations of the atomic configurations. The STEM-EEL spectra were obtained in the same TEM system (FEI Titan³ G2 60-300) with Gatan Quantum 965 dual EELS system at 80 kV. The energy spread of a monochromated zero-loss peak was 0.15 eV in full-width at half-maximum at 0.01 eV/ch energy dispersion. The convergence angle was 26.6 mrad. Each spectrum was acquired for 0.00053s with 0.1 energy dispersion. Zero-loss peaks were subtracted to 2 eV due to the tails and plural scattering is removed using Fourier-log method using Gatan Digital Micrograph software.

Image processing and simulations. Some TEM images presented in this study were processed to emphasize interesting features as described below. I applied false-color for better visualization using a color-look-up table and performed bandpass filtering with 40- and 3-pixel filtering for large and small structures, respectively, to make the image contrast even using the Image J software. Fourier filter built in Gatan Digital Micrograph was used to confirm the edge configuration. Inverse FFT (IFFT) image was obtained from the filtered FFT image after negatively masking all the hexagonal spots representing the hBN lattice in real space. The TEM image simulations were performed using MacTempasX under the experimental TEM imaging condition.

Computational methods. To explain the atomic and electronic structure of twin boundary of BN nanoribbons, the DFT calculation was performed within generalized gradient approximation (GGA) using the VASP[183-185]. The PAW potentials, as implemented in the VASP, were employed to describe the potentials from atom centers. The energy cutoff for the plane-wave basis was set to 400 eV in GGA. Geometries were optimized until the Hellman-Feynman forces acting on the atoms became smaller than 0.01 eV/Å. To include weak vdW interactions among them, the Grimme's DFT-D2 vdW correction was adopted based on a semi-empirical GGA-type theory[123]. For the Brillouin-zone interaction a (9x1x1) and (20x1x1) grid was used for atomic relaxation and band states calculation in Gamma centered special k-point scheme, respectively. The super cell of 558, 44 and 6′6′ configuration is consisting of 26 boron, 28 nitrogen and 4 hydrogen atoms.

To investigate the temperature dependence of the structural deformation behaviors of twin boundary of BN nanoribbons, MD simulations was performed at temperatures of 10 ~ 1000 K. NVT-MD simulations was performed using the LAMMPS with a ReaxFF potential[186] for 40 ps.

5.3. Results and discussion

5.3.1. Synthesized few-layer films of hBN with AA′ and AB stacking structures

A few-layer hBN films was synthesized on a copper substrate using CVD and transferred them onto TEM grids[140, 187]. First, DF-TEM was performed on oriented, few-layer hBN films to determine their structural characteristics. Figures 501a, b are DF-TEM images obtained using a second-order ($\Phi2$) and first-order ($\Phi1$) spot from a SAED pattern (inset of Figure 27a). Triangular, multi-layered hBN islands are grown on continuous monolayer hBN film with the same orientation. The intensities of the islands acquired from diffraction spot $\Phi2$ increase with the number of layers, regardless the AA′ or AB stacking structure (Figure 27a). However, the intensity obtained from diffraction spot $\Phi1$ is determined by the stacking structure (Figure 27b). In Figure 27b, some regions show brighter contrast with the increasing number of layers, indicating that they have the AA′ stacking structure, while the darker regions despite having the same number of layers as the AA′-stacked region have the AB stacking structure. The darkest region outlined with white solid line represents an ABC-stacked region because all the diffracted waves interfere destructively and cancel out each other for this region. However, DF-TEM hardly verifies that an AA′-stacked region is not AA-stacked or that an AB-(AC-) stacked region is not an AB′-(AC′-) stacked region since those images have similar diffraction conditions[99]. Hence, the stacking structures were confirmed directly using AR-TEM images (Figure 27c-e). The AA′-stacked bilayer region shows the same hexagonal lattice contrast but brighter than the monolayer region, while the AB-stacked bilayer region reveals a triangular shape with alternating contrast[188-189] (Figure 27c). The AA′ and AB stacking were further confirmed by the relation of orientation of the triangular defects in two different layers. Triangular hole created by 80 kV electron-beam irradiation always show N-terminated edges[88, 167-168]. Thus, triangular defects in adjoined layers have the same orientations in AB stacking ([BN]/[BN]) (Figure 27d), while those in AA′ stacking ([BN]/[NB]) point in opposite directions (Figure 27e). Therefore, a combination of DF-TEM and AR-TEM clearly proves that AA′- and AB-stacked, few-layer hBN films have been grown in this CVD system.

Recent experimental works have suggested the possibility of AB-stacked hBN[99, 181-182] but none reports coexistence of AA′- and AB-stacked hBN in one continuous island. Note that coexistence and even perfect stitching of AA′ and AB stacking structures of the hBN islands is shown in the upper right part of Figure 1b. Many studies have reported the existence of transition regions without high symmetry structures between different phases or stacking structures[103-105].

Transition regions which lost high symmetry stacking structure (neither AA′ nor AB) appear dark in DF-TEM images acquired from the second-order diffraction spot, $\Phi2$ (refer to Figure 8), but surprisingly no dark line was detected between the AA′ and AB stacking structures in our DF-TEM image in Figure 27a (yellow dash-lined regions in Figure 27b). This represents an abrupt change of stacking structure without any transition region between AA′ and AB stacking. The stacking boundary

was further studied under high magnification. Conditions whether it forms the atomically sharp stacking boundary or broad transition region will be discussed in the Chapter 5.3.4.
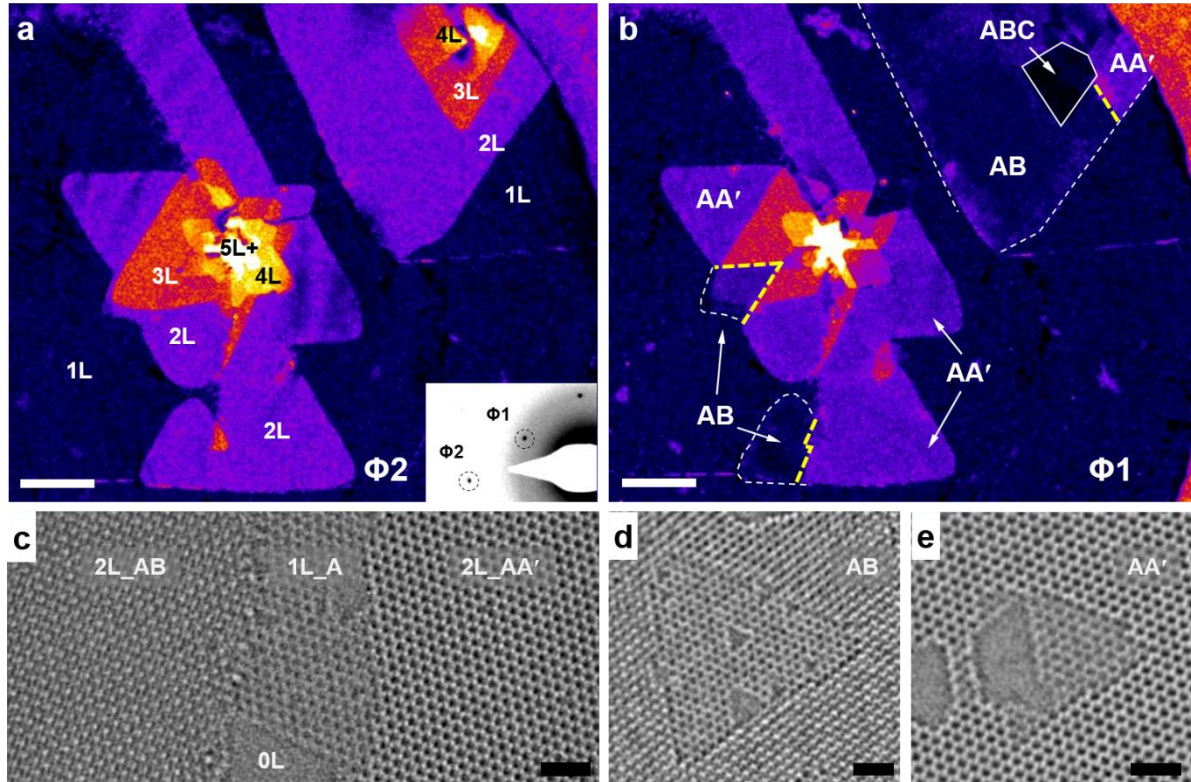
Figure 27. TEM images of few-layer AA′- and AB-stacked hBN films. a,**b**, False-color DF-TEM images of triangular, few-layer hBN islands from (**a**) a second-order diffraction spot [Φ2, inset of (**a**)] and (**b**) a first-order diffraction spot [Φ1, inset of (**a**)]. In (**a**), regions with one layer (1L) and two layers (2L) are identified, while different stacking structures (AA′, AB, etc.) are shown in (**b**). The outer part of the rim on the right side of each image is an amorphous-carbon mesh on the TEM grid. **c-e,** AR-TEM images of AA′- and AB-stacked hBN. Triangular defects grow in the same orientation in AB-stacked hBN (**d**) and in the opposite direction in AA′-stacked hBN (**e**). Scale bar (**a**,**b**), 0.1 μm, (**c-e**), 1 nm.

5.3.2. Twin boundary at the AA′ and AB stacking boundaries

Figure 28a is an AR-TEM image taken from the white-boxed area in the false-color DF-TEM image in Figure 28b, which has no dark line between islands having different stacking structures. The magnified atomic images on each side of the insets in Figure 28a clearly show the AA′ and AB stacking structures on the left and right sides of the figure. Both sides contain three layers, as confirmed by counting the etched layers after prolonged electron-beam irradiation (Figure 29). In addition, the "ABA" stacking structure on the right side instead of an "ABC" structure is proved by the contrast difference in the TEM image simulation (Figure 30). Hence, the tri-layers of AA′A- and ABA-stacked hBN are stitched together perfectly, forming an atomically sharp stacking boundary along zigzag direction. Figure 28c displays the stacking boundary in a false-color image of the black-boxed region in Figure 28a.
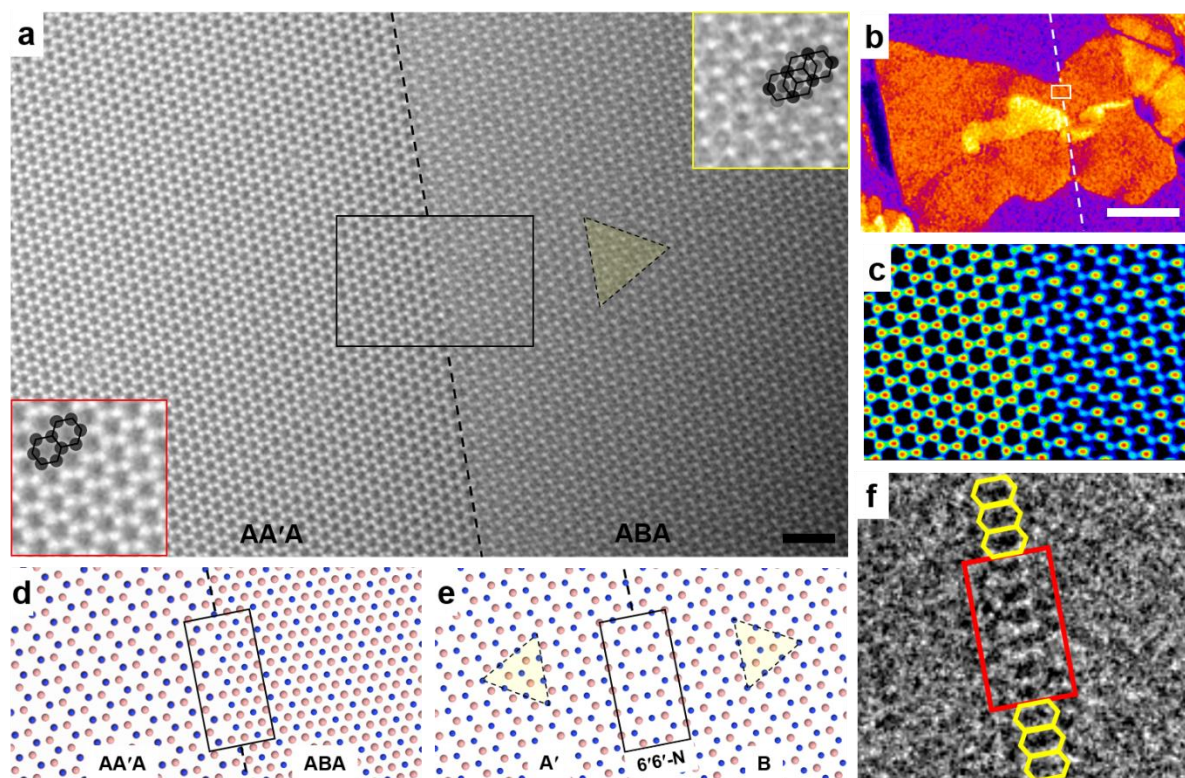
Figure 28. Atomically sharp AA′/AB stacking boundary. a, AR-TEM image of the stacking boundary of a tri-layer ABA/AA′A-stacked hBN film, from the white-boxed region in (**b**). **b**, False-color DF-TEM image. **c**, False-color image of the black-boxed region in (**a**). **d,e**, Atomic models of the stacking boundary of AA′A/ABA-stacked hBN (**d**) and of the middle layer A′/B (**e**) after removing two "A" layers each from the top and bottom. Boron and nitrogen atoms are represented by pink and blue spheres, respectively. **f**, Inverse fast Fourier transform image displays the 6′6′ configuration at the boundary. Scale bar in (**a**), 1 nm and (**b**), 0.1 μm.
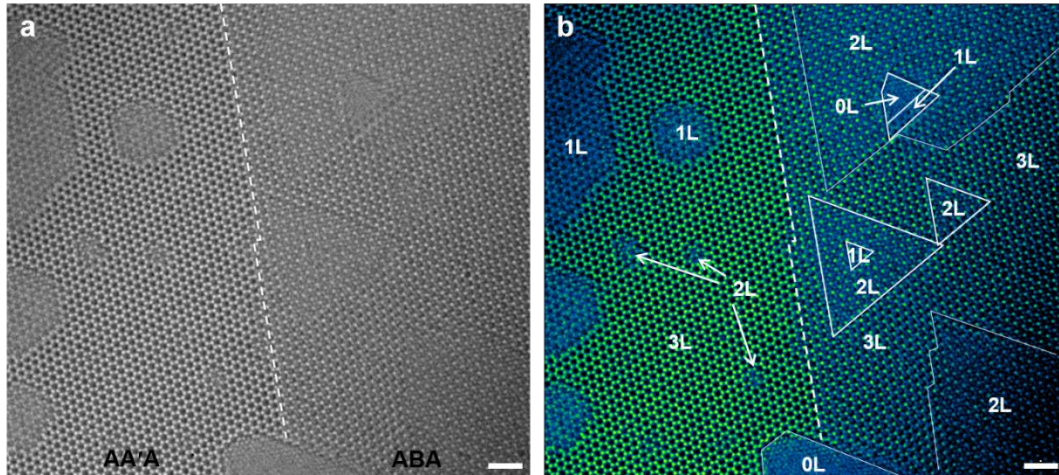
Figure 29. AR-TEM image of the same region as in Figure 28a after tens of seconds of electron-beam irradiation. A few layers in some regions are etched out by the electron beam. Raw image (**a**) and colorized image (**b**) for better visualization of the numbers of layers. Colors change from green to blue as the number of layers decreases from 3 L to 0 L (vacuum) in each of the AA′- and AB-stacked regions. Both the AA′- and AB-stacked regions are tri-layers. Scale bar, 1 nm.
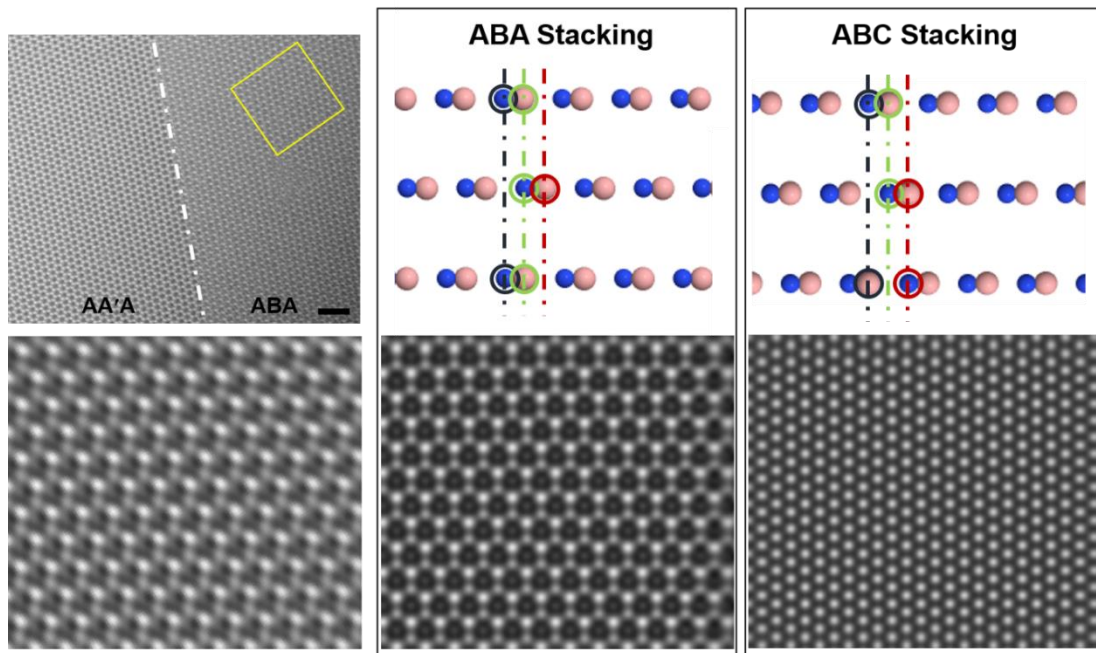
Figure 30. AR-TEM image from Figure 28a and simulated images of the ABA and ABC stacking configurations. The ABA stacking shows stronger contrast in positions where three atoms are superimposed, weaker contrast for two atoms, and faint for one atom at the given position. There is no contrast difference for ABC stacking because two atoms are piled up at all positions. The AR-TEM image matches the ABA stacking configuration. Scale bar, 2 nm. Boron and nitrogen atoms are represented by pink and blue, respectively.

To determine the atomic configuration at this boundary, a corresponding atomic model is made (Figure 28d) and subtracted two "A" layers, one each from the top and bottom, leaving only the middle A′ and B layers (Figure 28e). This shows that the boundary acts as a mirror plane for the A′ and B regions, i.e., a twin boundary. The deduction of the atomic configurations in Figure 28d, e starts from the four possible structures of AA′A/ABA stacking boundary along zigzag direction (Figure 31). Depending on the orientation of [BN] or [NB] and the stacking order of AB or AC, the AA′A/ABA stacking boundary in zigzag direction can have four different types of twin boundaries. They are denoted by (1) 6′6′-N, (2) 44-B, (3) 6′6′-B, and (4) 44-N, where 6′6′ (44) represents an oblong hexagonal (rhombal) ring and -N(-B) denotes the N(B) mirror plane at the twin boundary. The 6′6′-N (44-B) twin boundary is formed at the center of an A′/B (A′/C) layer when the first layer A has [BN] orientation. The 6′6′-B (44-N) twin boundary is formed at the center of the A′/C (A′/B) layer when the first layer A has the [NB] orientation.

Two verification steps were performed to determine which of the four possible structures best fit the observations shown in Figure 28a. First, the orientation of the N-terminated triangular defect highlighted in yellow in Figure 28a matches that of either (1) 6′6′-N or (2) 44-B. In addition, the intensity profile across the twin boundary (Figure 32) proves that the 6′6′-N structure matches the experimental result shown in Figure 28a. Therefore, an atomically sharp twin boundary, with N atoms as the mirror plane and novel oblong hexagons (6′6′), is formed at the middle layer of the AA′A/ABA stacking boundary (Figure 28e). IFFT image (Figure 28f), obtained by inversing the filtered FFT after removing the typical hBN lattice information, also shows the 6′6′ configuration (Figure 33).
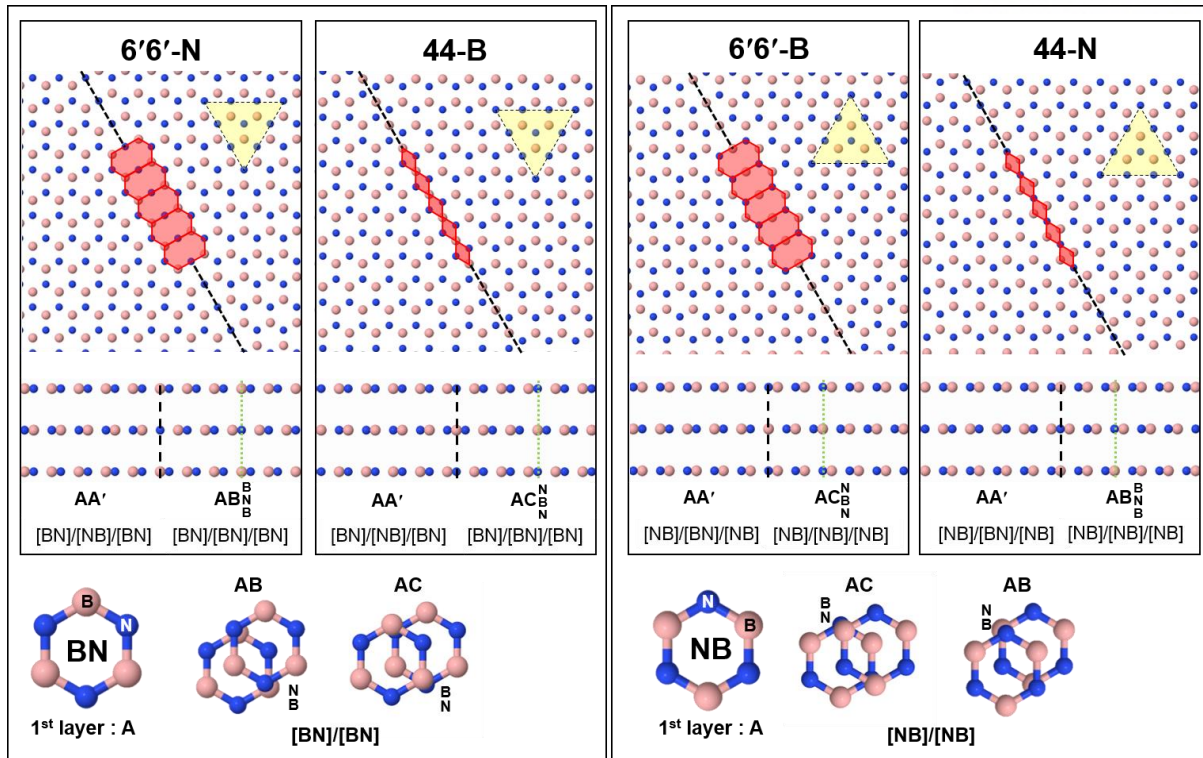
Figure 31. Atomic structures of the four possible stacking boundaries. Each top-view image is from the middle layer of the stacking structure represented below it. A 6′6′-N (44-B) twin boundary is formed at the center of an A′/B (A′/C) layer when the first layer A has the [BN] orientation. A 6′6′-B (44-N) twin boundary is formed at the center of an A′/C (A′/B) layer when the first layer A has the [NB] orientation. Boron and nitrogen atoms are represented by pink and blue spheres, respectively.
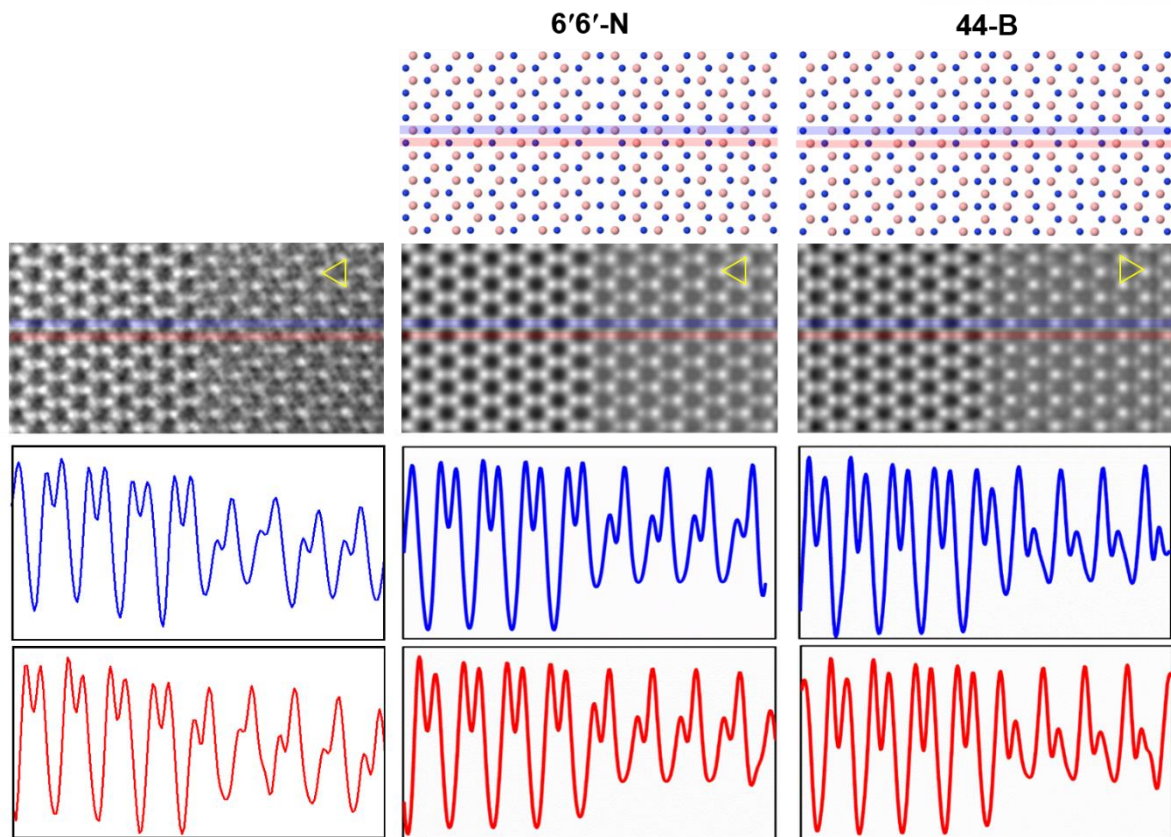
Figure 32. Intensity profiles along the blue and red lines in the experimental image (left) and the two simulated images (middle and right) of the 6′6′-N and 44-B structures, respectively. Yellow triangles are drawn by connecting three brighter sites of hexagonal lattice to highlight the difference between intensity of the 6′6′-N and 44-B structures. Boron and nitrogen atoms are represented by pink and blue spheres, respectively.
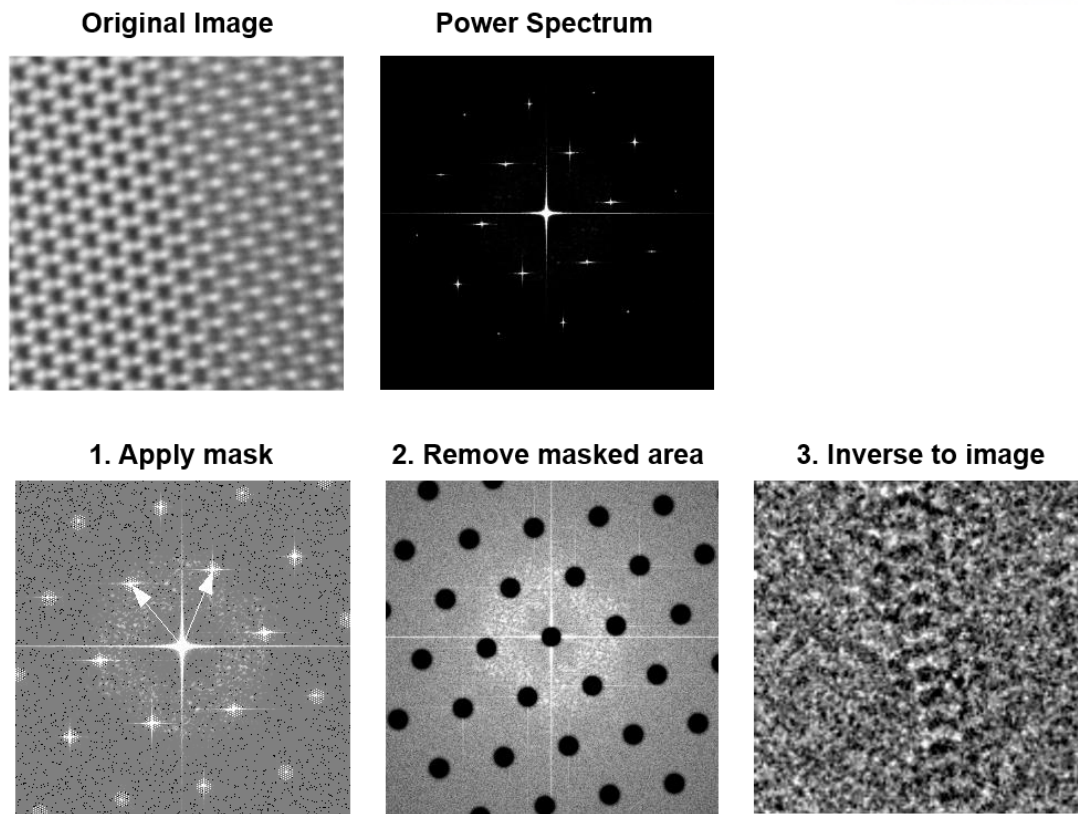
Figure 33. The 6′6′ configuration in a Fourier-filtered image at the A′/B boundary. Since it is not easy to directly observe the 6′6′ configuration sandwiched within three layers, additional filtering was applied to extract the 6′6′ configuration from the original image (Figure 28a). IFFT image was obtained by inversing the filtered FFT after removing the typical hBN hexagonal diffraction spots. The resulting image thus shows only the mismatched lattice from a typical hBN lattice. The result confirms the formation of the 6′6′ configuration at the A′/B boundary.

5.3.3. 6′6′ vs. 558 configurations: DFT, MD, and image simulations

The N atoms at the mirror plane of the 6′6′-N structure are doubly coordinated with one dangling bond. This obviously raises a question about the stability of the structure. Using DFT calculations the stabilities of the four possible atomic configurations at the twin boundary were tested (Figure 34): (1) 6′6′-N, (2) 44-B, (3) 6′6′-B, and (4) 44-N. As a result, the 6′6′-N configuration changes into 558-N (two pentagons and one octagon), a fully-coordinated, stable structure, with the uncoordinated N atoms bonding together (Figure 34a, c). There is no shift in the positions of the atoms on the left and right, except for a slight in-plane movement (<1 Å) of the uncoordinated N atoms in the middle layer. The 44-B structure (Figure 34b) also changes to 558-N by shifting all atoms on the right side of the boundary, as indicated by the red arrow marked in Figure 3c. Similarly, the stable form of 6′6′-B (Figure 34d) becomes 558-B (Figure 34f), with the uncoordinated B atoms at the mirror plane saturating each other. The structure 44-N (Figure 34e) could not retain the original bonding due to large distortions, with the atoms kicked from the plane. The 558 structure is more stable than 6′6′ for the monolayer, bilayer, and trilayer cases.

Nevertheless, the intensity profiles along the lines at the AA′A/ABA stacking boundary in the experimental (purple), simulated 6′6′ (red), and simulated 558 (olive) images indicate that the structure observed by TEM are more likely 6′6′ configuration than 558 as shown in Figure 35a. There are distinctive height differences between the peaks in the experimental and simulated 558 image, whereas little difference between the experimental and simulated 6′6′ images. The height differences of the peaks in the 558 configuration are thought to be due to differences in the electron densities in the pentagon and octagon regions. The same analysis were performed but in the opposite defocus to prove the tendency of line profile is consistent with defocus condition (Figure 35b).
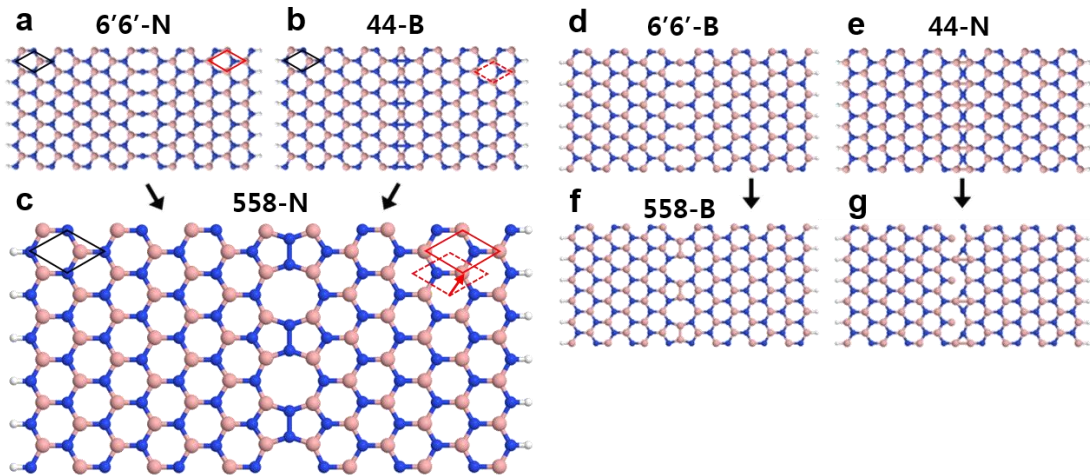
Figure 34. Illustration of the atomic configurations at a twin boundary by DFT calculations. The optimized structures (**c**,**f**,**g**) of the initial four possible structures at the stacking boundary (**a**,**b**,**d**,**e**) show the construction of the 558 configurations as a twin boundary. The symbols -B(-N) stand for B(N) atoms in the mirror plane at the twin boundary. Boron and nitrogen atoms are represented by pink and blue, respectively.
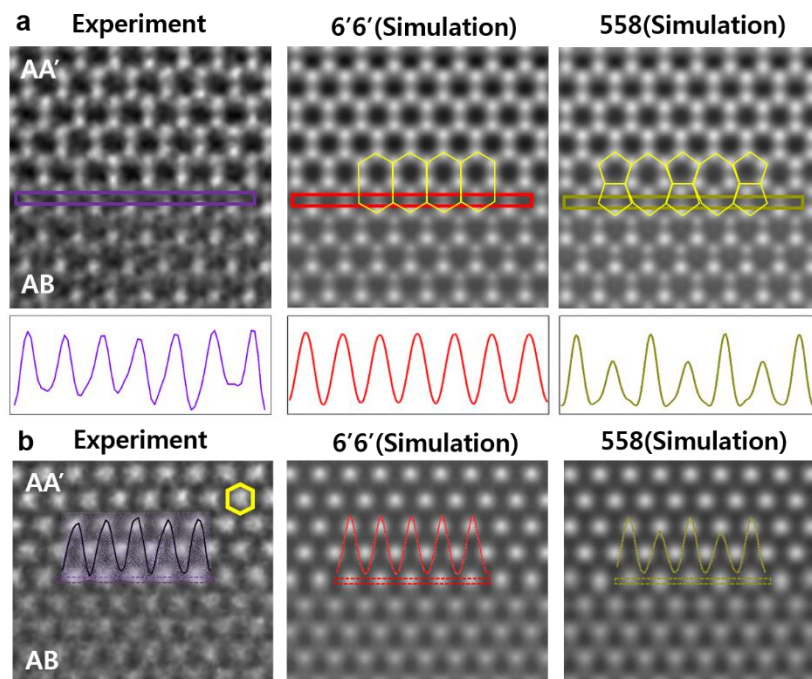
Figure 35. a, Intensity profiles along the AA′/AB stacking boundary in the experimental images (purple), simulated images of the 6′6′ (red) and 558 (olive) configurations. **b,** Intensity profiles along the AA′/AB stacking boundary in the experimental image and simulated images of 6′6′ and 558 configurations at the opposite defocus to (**a**). In this representation, atoms appear black.

To explain the discrepancy between the results of the DFT calculations and the experimental observations, MD simulations were performed monitoring N-N atom distances along the 558-N twin boundary at temperature of 10 K, 100 K, 300 K, and 1000 K. Figure 36a is one representative result among 400 frames of the MD simulation performed at 100 K with varying N-N atom distances. The measurements of the N-N bond length over 400 frames at 10, 100, 300, and 1000 K are summarized in Figure 36b. The results of MD simulations at 10 K accord with DFT calculations that the 558 configuration is preferred. As temperature increase to 100 K, a few 558 configurations break their N-N bonds and turn to 6′6′ configuration. At temperature of 300 K, almost all of N-N bonds are broken to have 6′6′ configuration. The results of MD simulations with raising temperature from 0 K to 300 K suggest the thermal energy delivered to the system serves to break N-N bonds of 558 configurations. Additional thermal energy in the system with a higher temperature, for example 1000 K, make 6′6′ configurations more vigorous. The experimental observations agree with the results of MD simulations at temperature of 300~1000 K, which covers the experimental temperature conditions. Interswitching of 558 and 6′6′ configurations (but dominant 6′6′) is further confirmed experimentally by IFFT images (Figure 37).
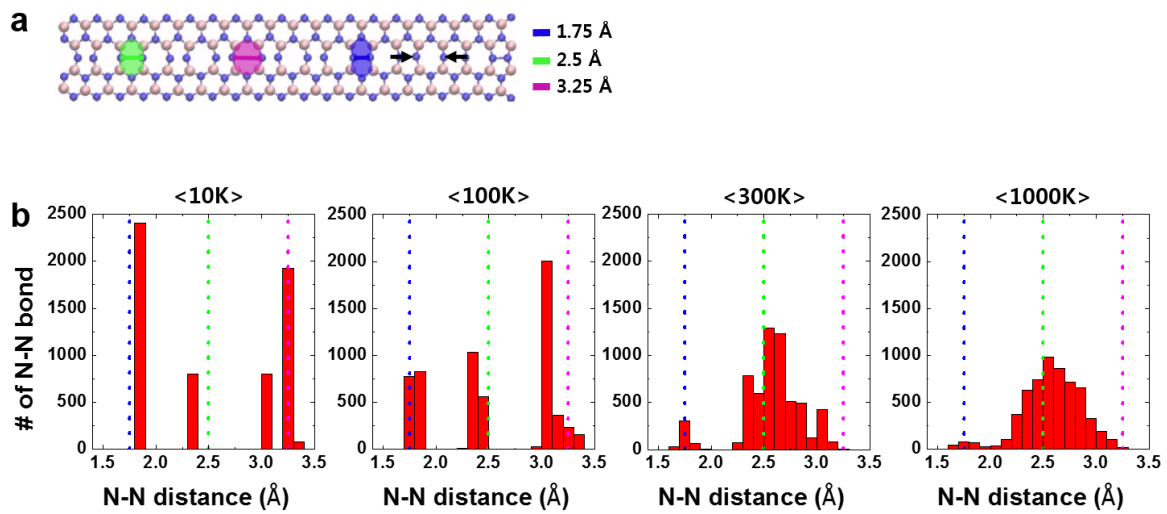
Figure 36. A summary of MD simulations of the structure of a 558-N twin boundary at 10, 100, 300, 1000 K. a, A frame selected from the 400 steps of the MD simulations at 300K shows varying N-N atom distances. **b**, Measurements of the N-N atom distances (marked in black arrows in (**a**)) over the 400 frames of MD simulations at 10, 100, 300, and 1000K are summarized. The points indicated by blue, green, and pink dotted lines represent the distance between N-N atoms of 1.7, 2.5, and 3.3 Å along the twin boundary, respectively.
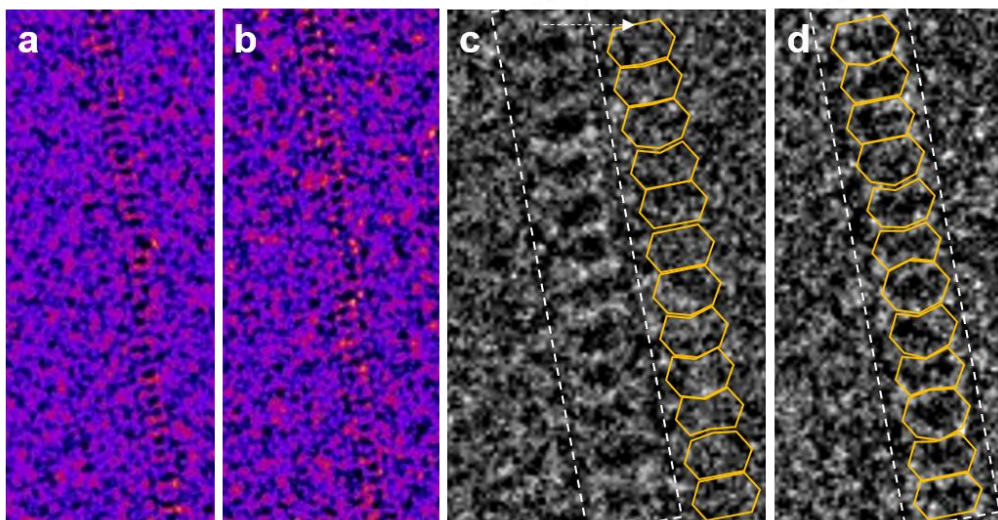
Figure 37. Interswitching of 558 and 6′6′ configuration. IFFT images at twin boundary from two different frames show the interswitching of 558 and 6′6′ configurations.

There is little structural difference between the 558 and 6′6′ configurations. However, there is a significant difference in electrical properties because of the presence of free electrons (dangling bonds). Figure 38 shows the electronic band structures calculated for both the 558-N and 6′6′-N hBN nanoribbons. N atoms along the twin boundary are fixed and the other atoms are fully relaxed through the structure for the calculation of band gap. The bandgap of the 558-N configuration is 3.44 eV, while the bandgap of 6′6′-N is zero (Figure 38a, b). The red circles in the band structures represent contribution of N atoms in twin boundary region. The bandgap of hBN nanoribbon decreases as the distance of N-N bond of 558 configuration increases from 558-N to 6′6′-N configuration (Figure 38c). The calculated band structure for 558-B hBN nanoribbon also shows a reduced bandgap of 2.64 eV (Figure 39).
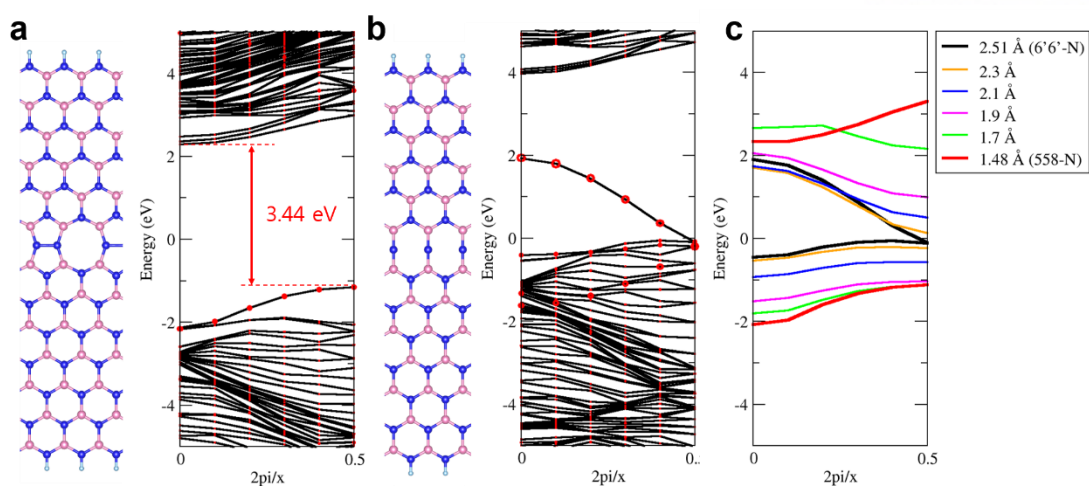
Figure 38. Band structure of hBN nanoribbons with 558-N and 6′6′-N configurations at a twin boundary. a,b, The atomic model and corresponding band structure for the 558-N (**a**) and 6′6′-N (**b**) configurations, respectively. The red circles in band structure represent contribution of N atoms in twin boundary region. Boron, nitrogen, and hydrogen atoms are represented by pink, blue, and cyan spheres, respectively. **c**, Conduction and valence bands to varying N-N atom distance from 558-N to 6′6′-N along the N atom twin boundary.
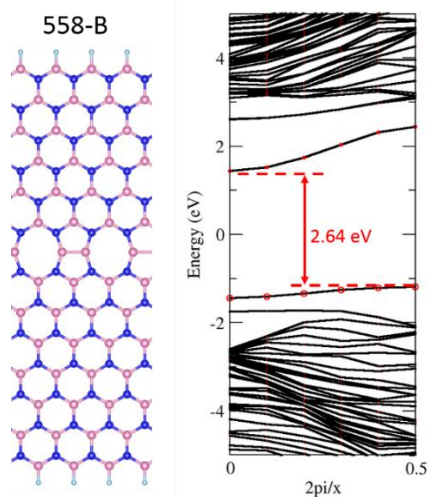
Figure 39. Atomic model of an hBN nanoribbon with a 558-B configuration and its associated band structure. The red circles in band structure represent the contribution of B atoms in twin boundary region. Boron, nitrogen, and hydrogen atoms are represented by pink, blue, and cyan spheres, respectively.

The bandgap at twin boundaries was experimentally assessed using EELS to compare to the calculated value. General instruments for bandgap measurement by optical methods offer high energy resolution but very poor spatial resolution (~μm)[152, 190-193]. Spatial resolution using optical methods is clearly insufficient to measure bandgap of one atom-wide AA′/AB stacking boundary and ~50 nm in length. Meanwhile EELS has proved to be a powerful tool for measuring bandgaps[194-197]. The bandgap can be assessed by applying a linear fit and directly reading the cross point between the extrapolated line and the bottom line from the first peak after zero-loss peak (ZLP) in EELS[197]. EEL spectra were acquired using Gatan Quantum 965 dual EELS system with energy resolution of 0.15 eV. The bandgap was assessed using linear fit method after subtracting ZLP and eliminating plural scattering using Fourier-log method. The limit of used EELS system is that ZLP needs to be subtracted to 2 eV due to the tail, thus a bandgap less than 2 eV is hardly assessed exactly. But still, a quite notable difference in EELS edge was found at AA′/AB stacking boundaries compared to pristine hBN.

Figure 40 shows four EEL spectra acquired near atomically sharp AA′/AB stacking boundary. The black EEL spectrum is from clean and pristine hBN, orange and green EEL spectra are from pristine hBN covered with hydrocarbon adsorbates on the surface, and red EEL spectrum is from the atomically sharp stacking boundary of hBN. The cross points where the extrapolated lines (blue dashed lines) meet with the bottom lines at the black, orange, and green spectra are all around 5eV, which represent the bandgap of pristine hBN. However, the red EEL spectrum acquired from the atomically sharp stacking boundary shows gradual decrease in the intensity of the front edge without steep falling to x-axis of 2 eV. Small intensity around 2 to 4 eV turning up at the orange and green EEL spectra (blue circled region) is due to the unavoidable amorphous hydrocarbon on the surface of hBN, which can be judged by the appearance of carbon K-edge around 300 eV at high energy loss region. To prevent misinterpretation of EELS signal in front of 5 eV, areas with small amount of hydrocarbon were carefully selected. The sample was heated up at 200 °C for a few hours and vacuumed overnight in ultrahigh vacuum TEM system. In addition, EEL spectra were acquired for the minimal time of 0.00053s per one position to minimize the deposition of hydrocarbon on the surface by intense electron beam (even in the high vacuum system) and overlap of the positions was avoided. Nevertheless, a small amount of deposition of hydrocarbon was unavoidable. The signals from 2-4 eV in the orange and green EEL spectra are distinctive but still the falling slopes are not changed and the cross point to x-intercept are 5 eV, even with the higher amount of hydrocarbon compared to that detected at the stacking boundary, which can be evaluated by the peak intensity ratio of B-K edge (~200 eV) to C-K edge (~300 eV). In contrast, the red EEL spectrum acquired at the stacking boundary shows lower slope with gradual decrease to 2 eV or further. Another example of line scanning EELS across the stacking boundary (Figure 41) also shows the gradual decrease of the front edge of peak to 2 eV at the stacking boundary.

The EELS results at the stacking boundaries could be from the 6′6′-N configurations with the

bandgap of 0 eV, or 558-B (N) configurations with 2.64 (3.44) eV bandgap, or mixed 6'6' and 558 configurations included within converged electron beam. Since ZLP has been subtracted to 2 eV, the exact onset of signal where the delayed front edge starts before 2 eV is not read. But, at least, the reduced bandgap at the atomically sharp stacking boundary was experimentally detected by using EELS.

Considering that a pure hBN nanoribbon has a wide bandgap ~ 5 eV[176], the twin boundary can act as an atomically thin electronic channel. The present observations of dominance of 6'6' configuration at twin boundaries open a new possibility for single-hBN nanoelectronic devices. Lahiri et al. have reported that this type of grain boundary in graphene can act as a metallic wire[4]. Similarly, the AA'A/ABA twin boundary in hBN can be a one-dimensional conducting channel embedded in the original insulating hBN, which is expected to be much more effective than a metallic wire in a conductive graphene sheet.
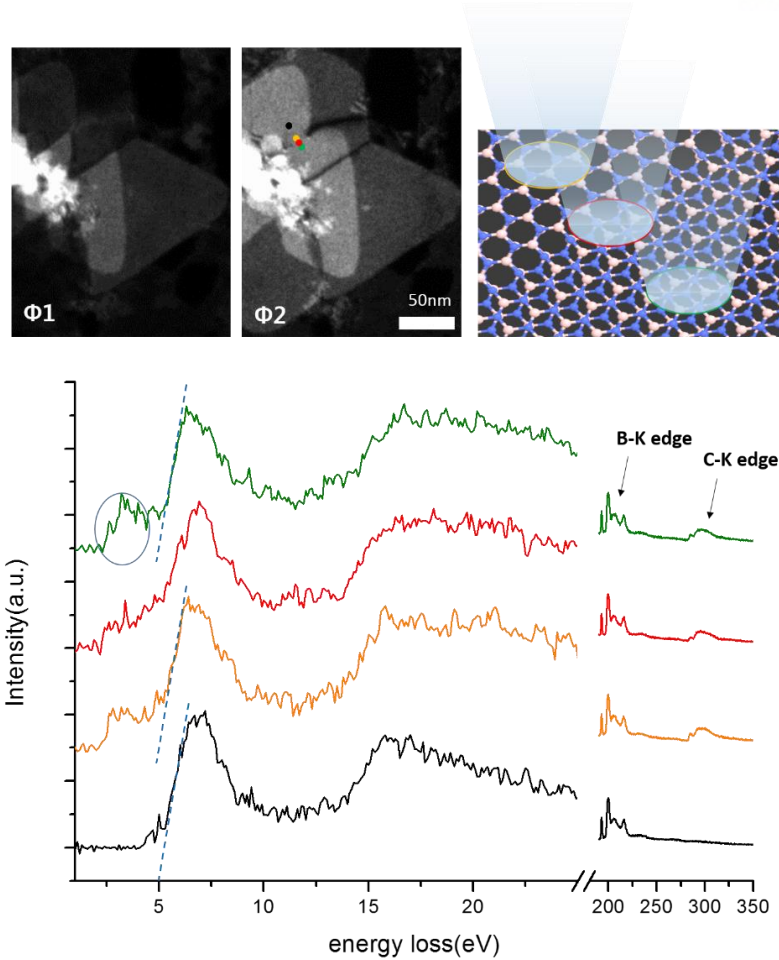
Figure 40. Bandgap measurement at an atomically sharp stacking boundary by EELS. Four EEL spectra are deconvoluted by subtraction of zero-loss peak and plural scattering from the original spectra. The black EEL spectrum is from clean and pristine hBN, orange- and green EEL spectra are from pristine hBN covered with hydrocarbon adsorbates on the surface, and red EEL spectrum is from the atomically sharp stacking boundary of hBN. The blue dotted lines depict extrapolation of the peaks to x-axis. Signals marked with blue circle around 2-4 eV arise due to the unavoidable hydrocarbon on surface of the sample.
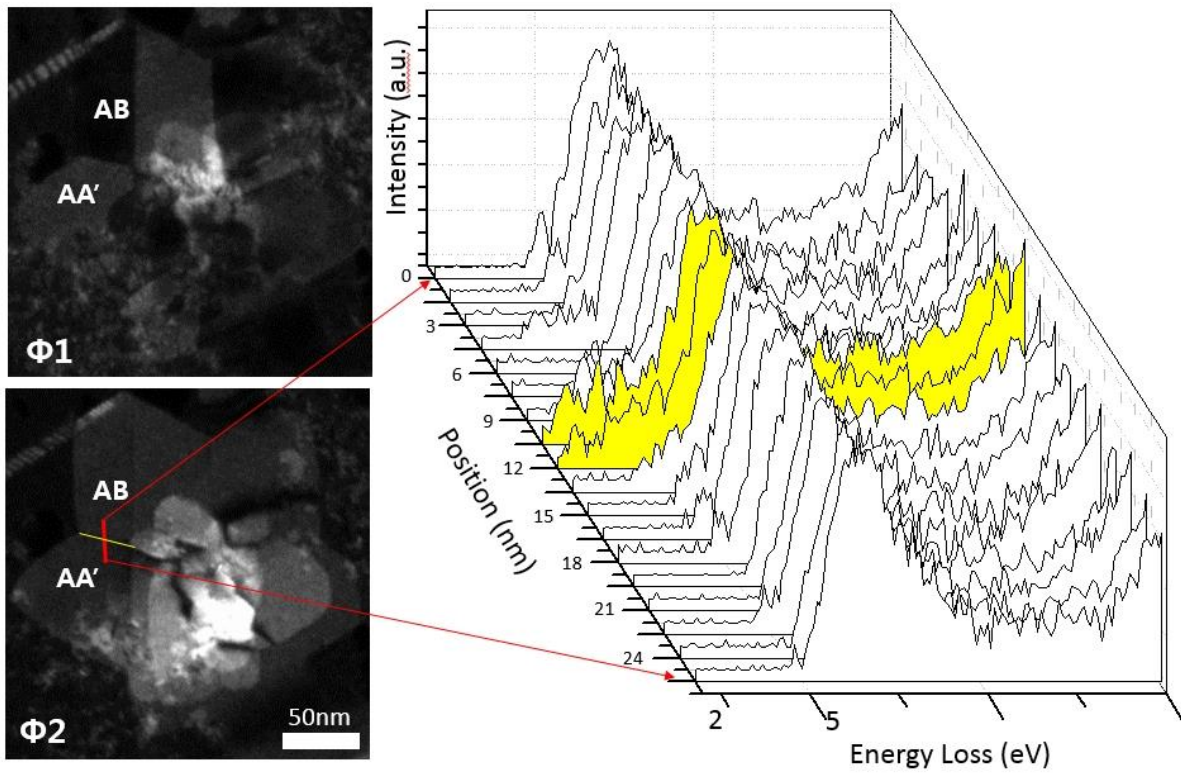
Figure 41. EELS line profile across an atomically sharp AA′/AB stacking boundary. On the contrary to the other EELS edges that have steep slopes to meet x-intercept around 5 eV, the front edges from the stacking boundary gradually decrease to 2 eV region with lower slopes. Space of each scan is 1.5 nm.

5.3.4. Stability of exposed and sandwiched 6′6′ twin boundary

Atomically sharp AA′/AB stacking boundaries are commonly found and clearly visible in tri-layer case as shown in Figure 42a. Atomically sharp AA′/AB stacking boundary in bi-layer, where one side of twin boundary should be exposed to ambient condition, are found but the "bare" 6′6′ configuration is not revealed under TEM since the boundary is always covered by hydrocarbon as shown in Figure 42b. This is because such "defect" line imbedded in perfect hBN hexagonal lattice has higher chemical reactivity. This suggests that a twin boundary sandwiched in the middle of a tri-layer, and thus protected by the top and bottom layers is much more stable than that lying in a bi-layer, wherein the twin boundary is exposed to ambient conditions. This does not mean monolayer 6′6′ twin boundary cannot exist alone. According to DFT calculations, the formation energy of hBN sheet embedding atomically sharp twin boundaries (558-N, 558-B) are all stable in mono-, bi-, and tri-layer. And MD simulations for 558 configuration in mono- and tri-layer turned to 6′6′ configuration favorably. In other words, 6′6′ twin boundary itself is theoretically stable to exist alone, if no foreign atom is wandering around as the system of simulations. In the real system, however, the exposed side was always covered by hydrocarbon. Therefore, the 6′6′ twin boundary is only clearly observable in tri-layer or more layer if sandwiched, since the top and bottom layer are protecting the twin boundary from the attachment of hydrocarbon outside onto the surface.

Next, the stability of sandwiched 6′6′ twin boundary was further studied under electron beam. Figure 43a-c show defect growth on the tri-layer AA′A/ABA staking boundary region by prolonged electron beam irradiation and Figure 43d-f are IFFT images of Figure 43a-c using the same method described in Figure507 for better visibility of the 6′6′ twin boundary. Note that defect growth speed in pristine AA′- or AB-stacked region are much faster than the atomically sharp stacking boundary region. Before I detect etching out of the protecting layers and see exposed 6′6′ configuration in the stacking boundary, the sheet was torn out due to the faster growth of defects in pristine AA′- or AB-stacked region. The stacking boundary region was undamaged under electron beam over 7 min. Similarly, in Figure 44, triangular defect growth at stacking boundary is slower than defect growth within pristine grains. A few atoms are sputtered out from the boundary region in this case, but still immature to observe exposed 6′6′ configuration since still one protecting layer is hindering to resolve the bare 6′6′ configuration. Triangular pits in IFFT images are from the defects sputtered, not representing a distortion of 6′6′ configuration. 6′6′ configurations near the defects along the stacking boundary remain stable.

To summarize, the sandwiched 6′6′ twin boundary is very stable for a long time of electron beam irradiation and even when some atoms are knocked out of the surface, compared to AA′ and AB-stacked intra-grain regions. However, I am being very careful to explain the reason of retarded defect growth in twin boundaries. This may be another evidence that the 6′6′ boundary acts as one-dimensional electron channel. But, interpretation of interaction of electron beams with electron clouds in atoms at the 6′6′

boundary is not simple to conclude a definitive answer. It needs further study for deeper understanding of electron beam damage mechanism of materials under electron beam irradiation.
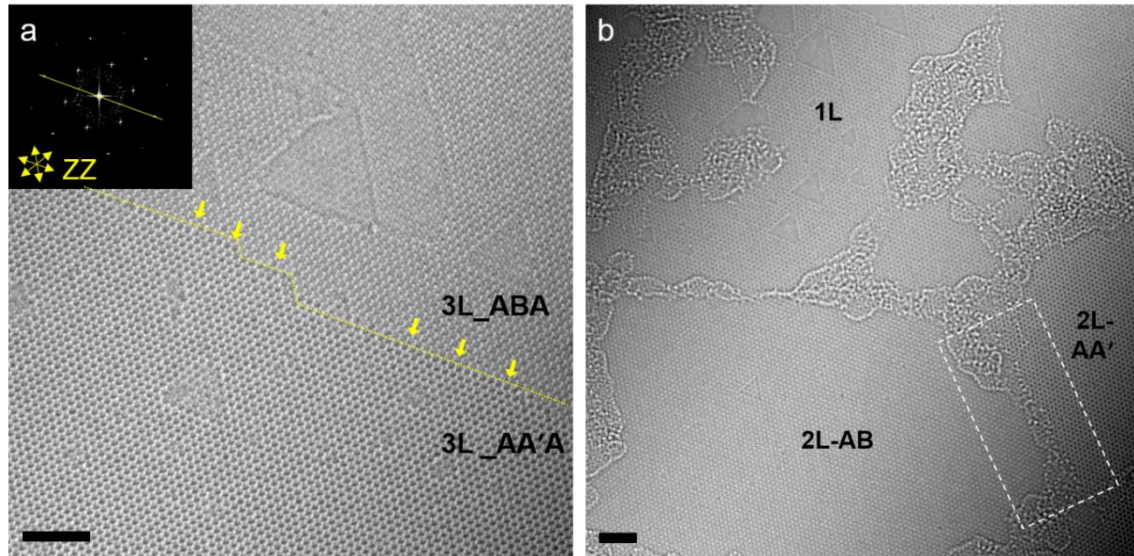
Figure 42. Atomically sharp stacking boundary in tri-layer and bi-layer hBN. a, Another example of a tri-layer AA′A/ABA stacking boundary. The stacking boundary is clearly visible. **b**, AA′- and AB-stacked hBN bi-layers stitch together perfectly without any transition region, although the boundary is covered by adsorbates on the surface (white-boxed area). Scale bar, 2 nm.
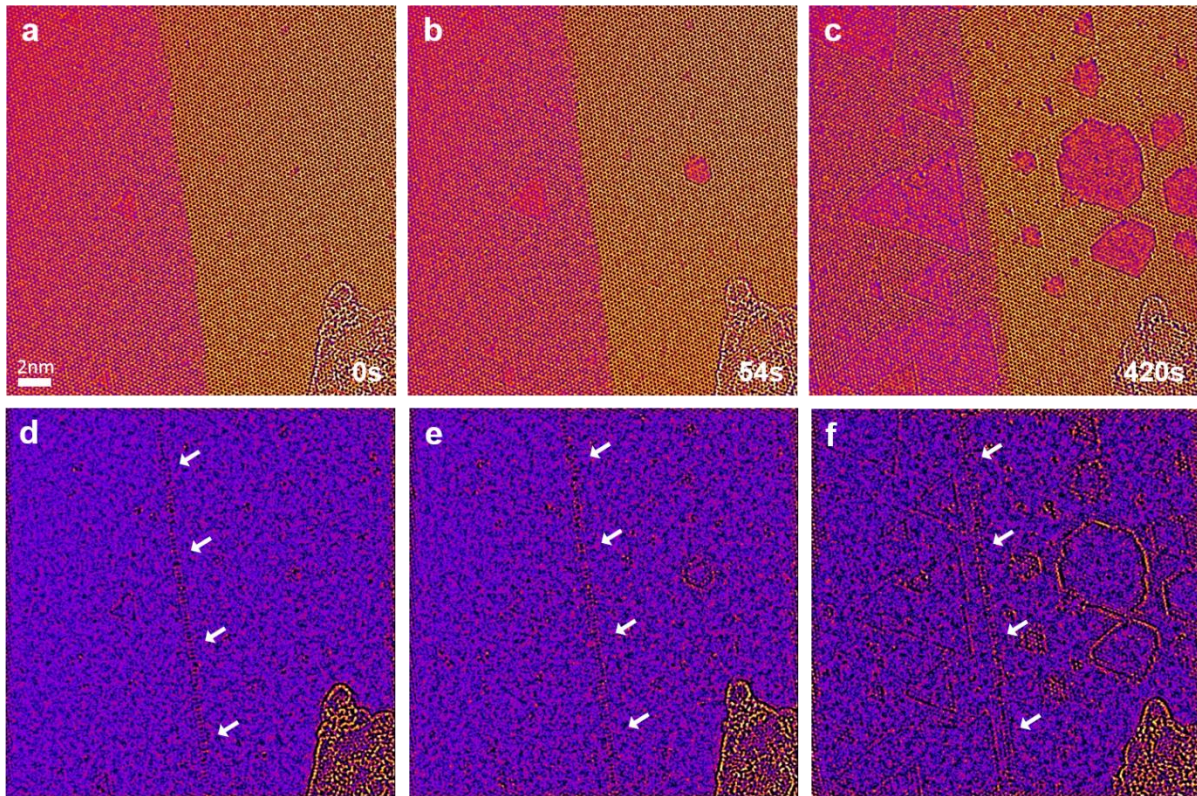
Figure 43. Defect growth by prolonged electron beam irradiation at tri-layer AA′A/ABA stacking boundary. False-colored AR-TEM images (**a-c**) and IFFT images (**d-f**) of defect growth over time. The twin boundary with 6′6′ configuration pointed by white arrow has remained stable while the defects grow fast within AA′- and AB-stacked grains.
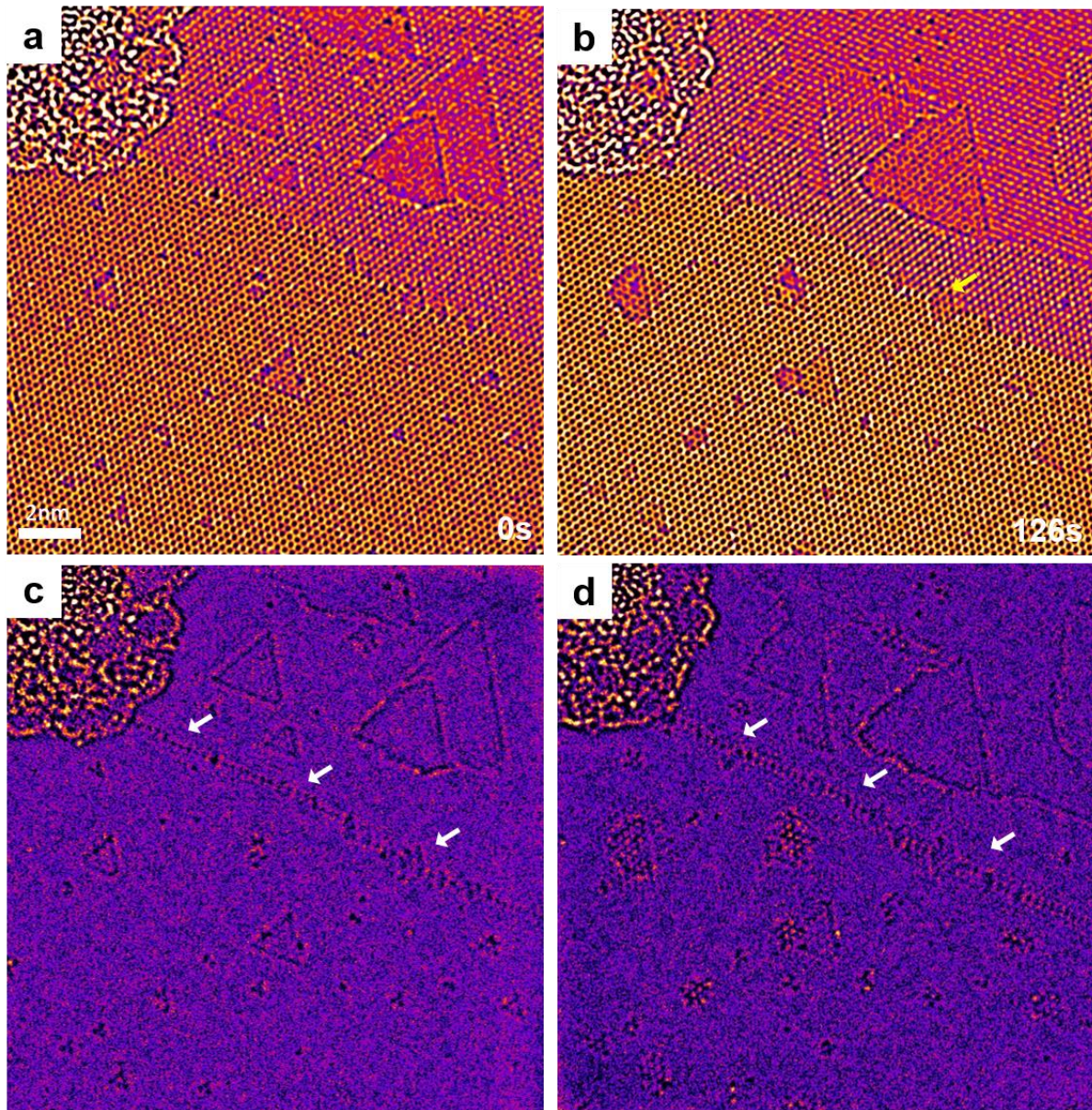
Figure 44. Defect growth by prolonged electron beam irradiation at AA′/AB stacking boundary. False-colored AR-TEM images (**a,b**) and IFFT images (**c,d**) of defect growth over time. A few atoms are sputtered out from the stacking boundary but the 6′6′ twin boundary remains its line between AA′- and AB-stacked hBN. White arrows point a 6′6′ twin boundary.

5.3.5. Formation mechanism of atomically sharp twin boundaries and EK edges

Atomically sharp stacking boundaries are commonly found in the hBN samples synthesized as described in experimental section, but some have a wide transition region in an AA′/AB stacking boundary. The probability of finding stacking boundary with an abrupt change or with a transition region was about half-and-half (Figure 45). I elicit that the formation of atomically sharp stacking boundaries is determined by certain combinations of AA′ and AB stacking during crystal growth from observations of EK edges at monolayer/bilayer boundaries of an AB-stacked region, as shown in Figure 46.

Figure 46a is an AR-TEM image of the hBN monolayer (1L) and bilayers (2L) with the layer boundary (1|2-layer boundary). The atomic configurations of the blue-boxed area containing the 1|2-layer boundary and the green-boxed area ([NB]-AC bilayer containing one edge of a triangular defect) are closely analyzed to confirm the edge configuration in Figure 47. Compared to the relative positions of the hexagonal and triangular patterns (orange lines) along bright contrast at the 1|2-layer boundary, the experimental image matches with the AC stacking structure. Thus, it is confirmed that the bilayer region in Figure 46a has [NB]-AC stacking. In addition, with the contrast difference at the positions here atoms exist or not along the boundary, the hexagonal edge is determined as 'closed' as usual, or 'open' also known as the EK edge. In Figure 46b, there is no contrast in the area marked by red dotted circles at the 1|2-layer boundary, whereas the white contrast is obvious where the N atoms exist at the edges of the triangular defect. The atomic model of the 1|2-layer boundary in Figure 46b is displayed with the stacking notation (Figure 46c), and the first layer ([NB]-A) is removed (Figure 46d). The result shows that the edge of the second layer ([NB]-C) is not terminated by N atoms, which is also known as an EK edge[198-199]. The EK edge was predicted as the fourth type of periodic edge, after the zigzag, reconstructed 5-7, and armchair edge for graphene[200] but there has been no report of EK edge for hBN. Now, suppose that a second layer of [BN]-A′ is grown on top of the monolayer region with AA′ stacking (the upper part of Figure 46e). If it meets the EK edge of the second layer of [NB]-C (the lower part of Figure 46e), a 6′6′-B twin boundary is created.
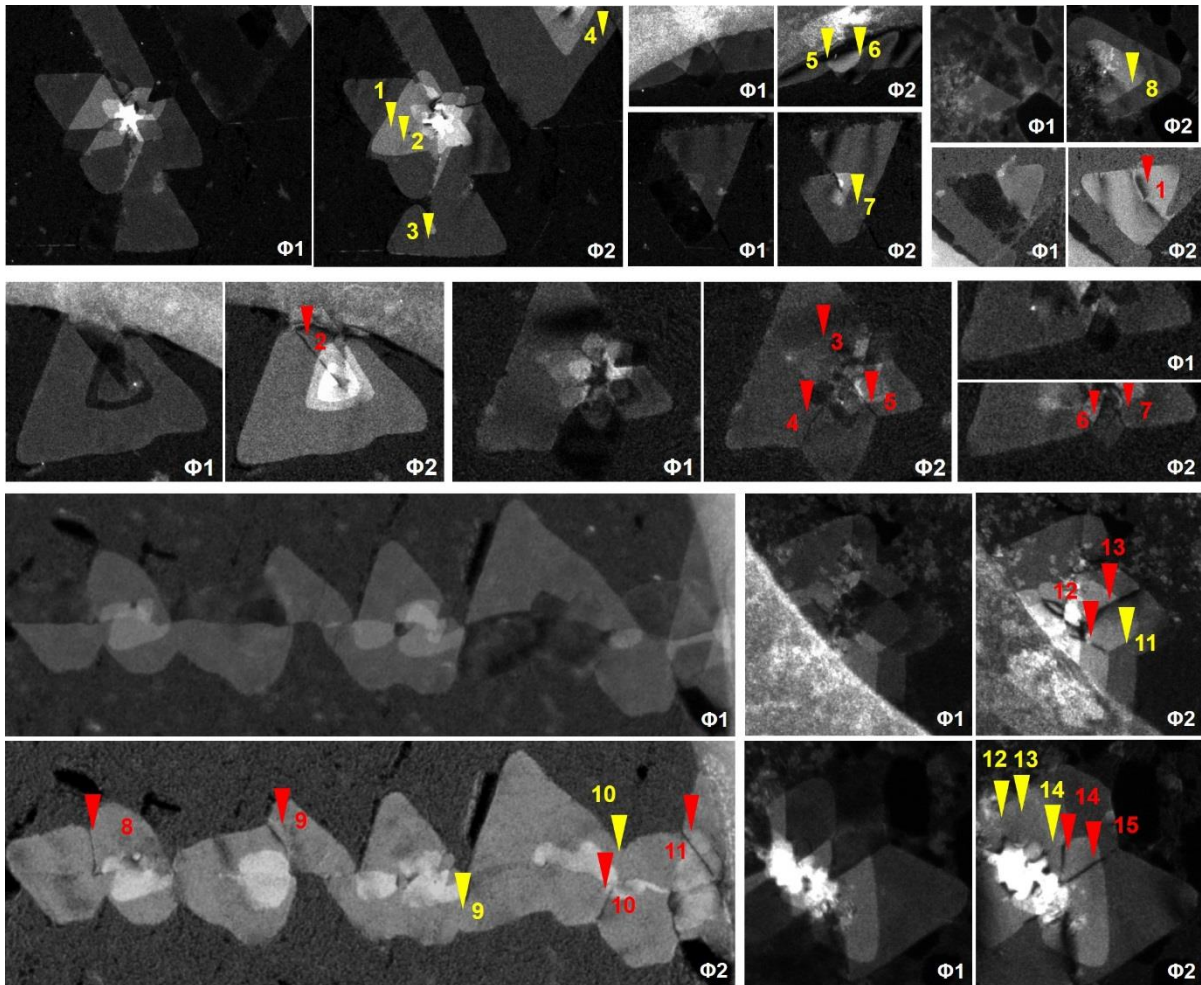
Figure 45. Probability of finding stacking boundary with an abrupt change or with a transition region. Yellow marked areas indicate atomically sharp stacking boundaries, where show no dark line in DF-TEM images acquired from the second order diffraction spot (Φ2). And red marked areas present stacking boundaries with transition regions with dark lines in Φ2 DF-TEM images. Among 29 regions, 14 atomically sharp stacking boundaries and 15 stacking boundaries with transition regions were observed (almost half-half probability).
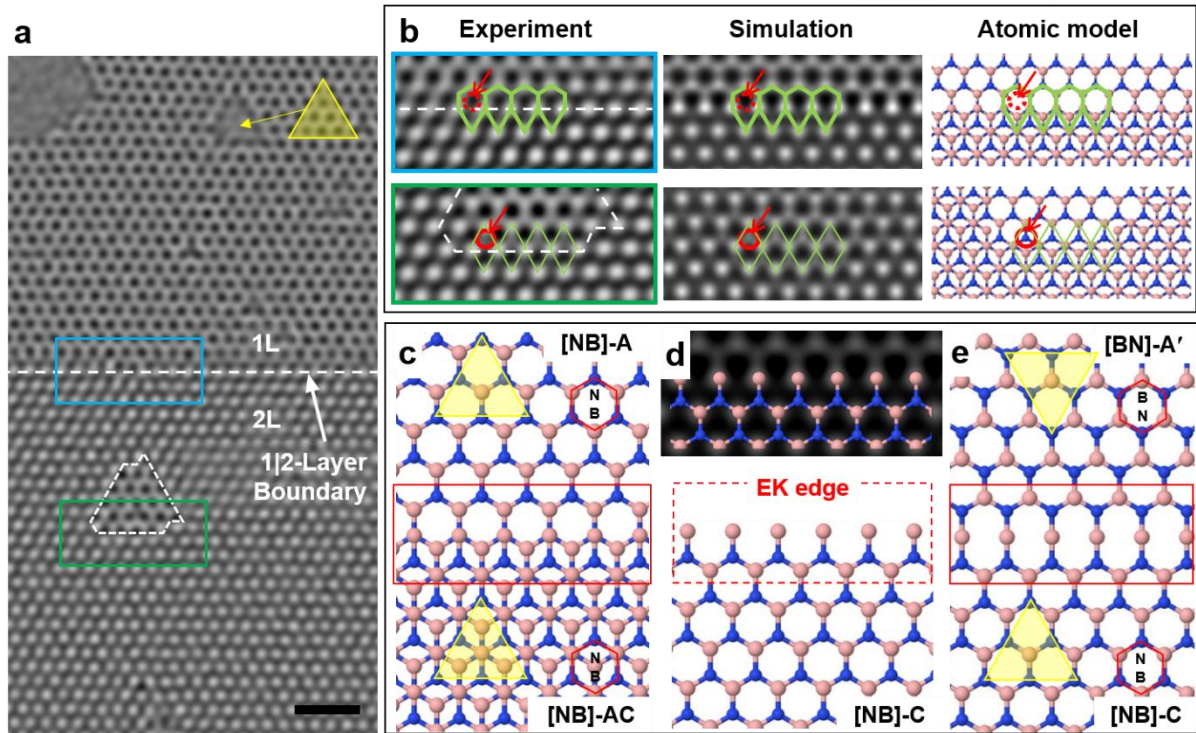
Figure 46. EK edge at a 1|2-layer boundary in AB-stacked hBN. a, AR-TEM image of mono- and bilayer hBN with an AB stacking structure. The white arrow points to the 1|2-layer boundary. Scale bar, 1nm. **b**, Experimental images from the blue-boxed (1|2-layer boundary) and green-boxed area (a triangular defect) inside (**a**), and the corresponding simulation image and atomic model. **c-e**, Formation mechanism of a twin boundary from observations of an EK edge. Boron and nitrogen atoms are represented in pink and blue, respectively.
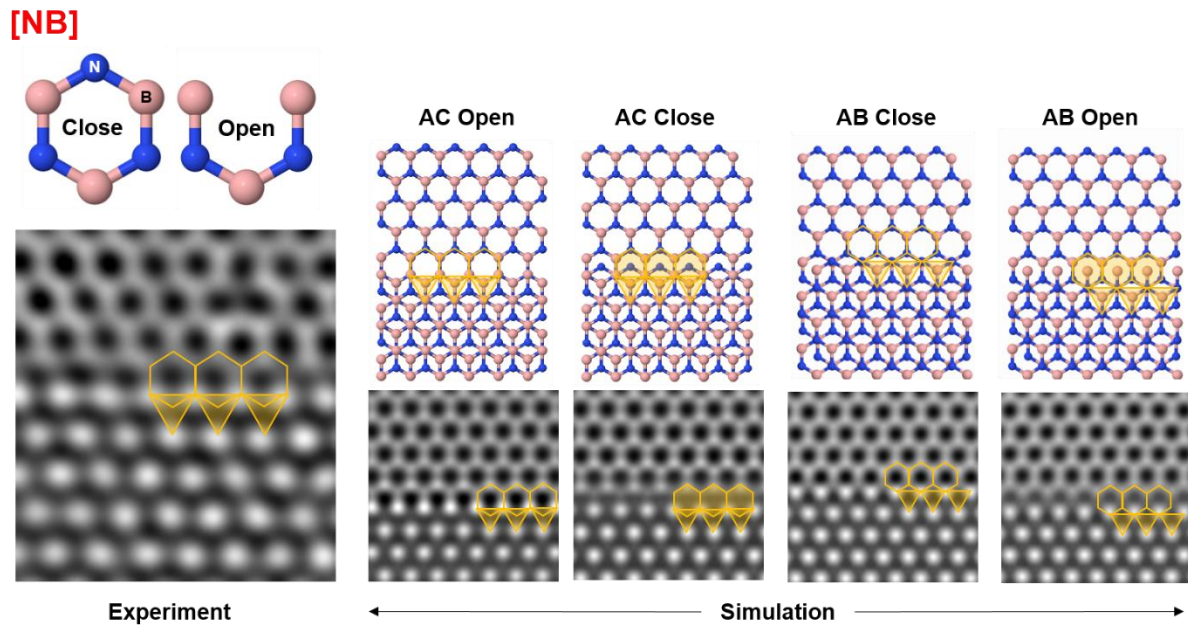
Figure 47. Comparison of experimental AR-TEM image with simulated images of open- and closed-edge conformations at the 1|2-layer boundary of AB-stacked hBN. The experimental image matches the open (EK) edge conformation. Boron and nitrogen atoms are represented by pink and blue spheres, respectively.

Note that a 6′6′-B twin boundary is formed only for the combination of AA′ and [NB]-AC stacking, as described in Figure 48. HBN has two types of EK edges: a B-atom EK edge for [NB]-oriented hBN and an N-atom EK edge for [BN]-oriented hBN (Figure 48a, d). The B-atom EK edge sits on the N atoms below when the structure has [NB]-AC stacking (Figure 48b, left), while it terminates at the hollow sites of the hexagonal lattice of the first layer when it has [NB]-AB stacking (Figure 48c, left). If the B-atom EK edge of the second layer meets the second layer of AA′-stacked hBN, [NB]-AC forms an atomically sharp 6′6′-B twin boundary (Figure 48b). However, the [NB]-AB configuration makes 44-N, which cannot maintain its structure, thus expected to form a transition region at the stacking boundary (Figure 48c). Moreover, the results of DFT calculations show that B-atom EK edge terminating at the N atoms below (Figure 48b, left) is much more stable than that terminating at the hollow sites of the hexagonal lattice of the first layer (Figure 48c, left) as described in Figure 49. Likewise, an N-atom EK edge of [BN]-AB creates an atomically sharp 6′6′-N twin boundary, while that of [BN]-AC forms a 44-B configuration. As previously explained in Figure 34, transformation of 44-B to 558-N requires overall shift of all the atoms of the half system as much of red arrow in Figure 34 by overcoming the van der Waals force. In addition, it causes a change in the stacking order, which convinces a creation of transition region. Notably, all four pairs of stacking structures for the EK edges and the consequential 6′6′ or 44 twin boundaries coincide with the structures as shown in Figure 31. Therefore, I conclude that atomically sharp stacking boundaries are formed only when AA′- and AB-stacked hBN meet with the certain combinations such as Figure 48b, e during crystal growth. It may open the way to synthesis of one atomic wide electronic channel by controlled manipulation of stacking structures.
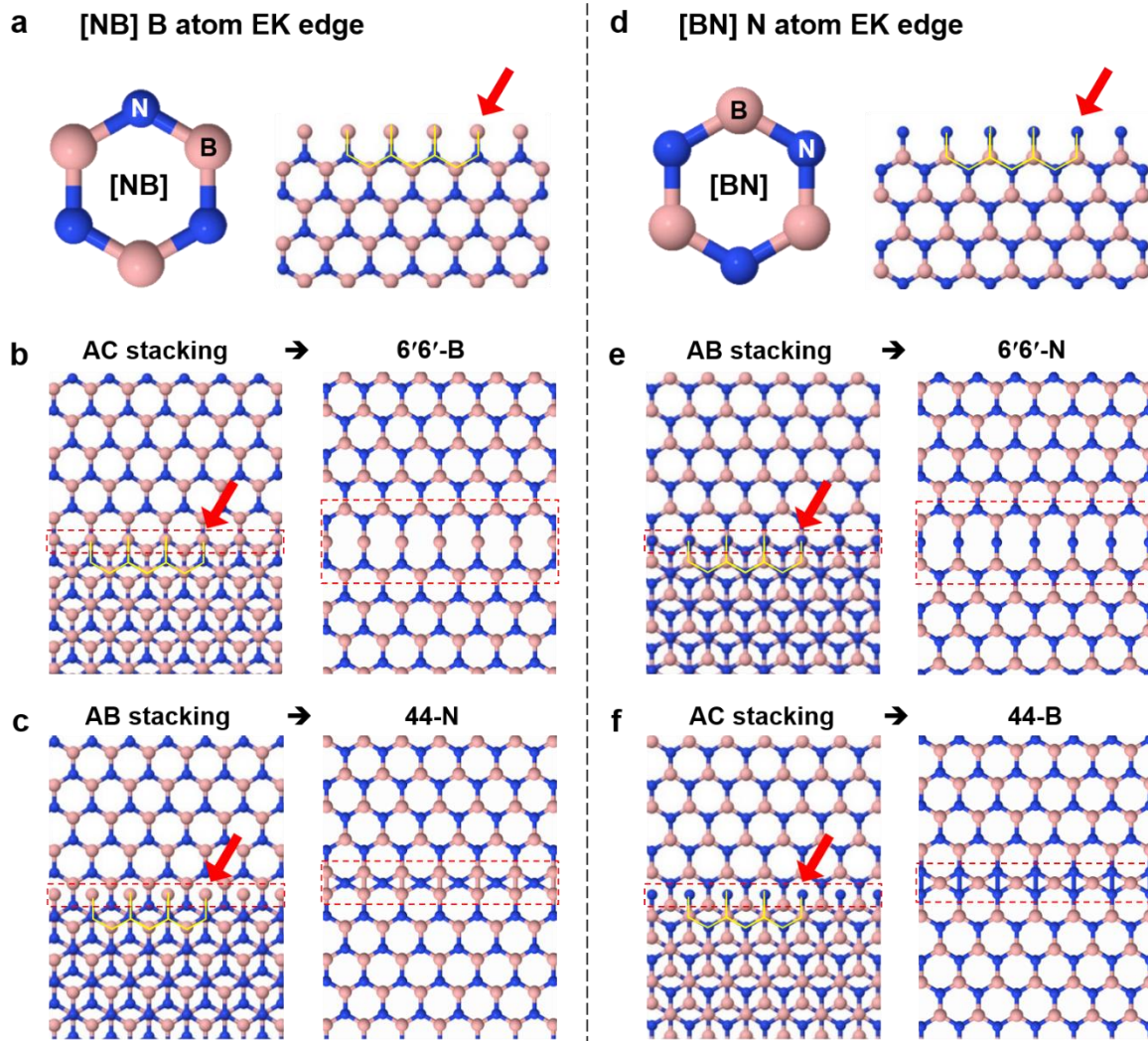
Figure 48. Two types of EK edges and the formation of different stacking boundaries depending upon the positions of atoms at the EK edges. a-c, A B atom EK edge of [NB]-AC creates an atomically sharp 6′6′-B twin boundary, while that of [NB]-AB forms a 44-N configuration. **d-f**, An N-atom EK edge of [BN]-AB creates an atomically sharp 6′6′-N twin boundary, while that of [BN]-AC forms a 44-B configuration. The atomic model to the left in each of panels (**b**,**c**,**e**,**f**) shows an hBN structure with an EK edge at the 1|2-layer boundary, while the panels to the right depict an AA′/AB stacking boundary configuration for the second layer, provided that it grows above the upper part of the first layer with the AA′ stacking structure and knits with the EK edge at the 1|2-layer boundary. Boron and nitrogen atoms are represented in pink and blue, respectively.
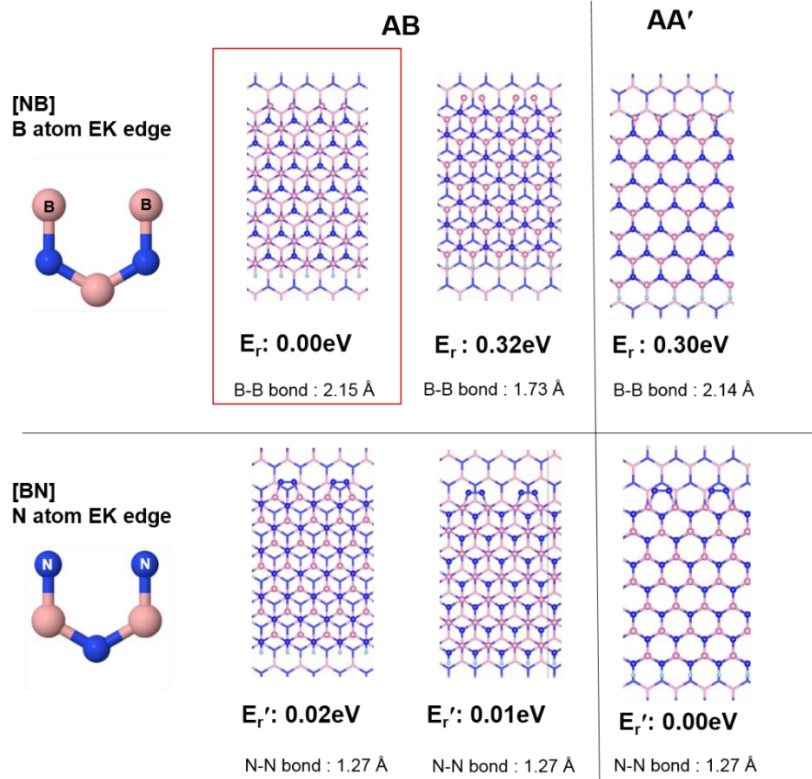
Figure 49. Relative energies of EK edge structures having B and N atoms in different stacking orders. Boron and nitrogen atoms are represented by pink and blue spheres, respectively.

5.4 Conclusion

The coexistence of AA′ and AB stacking structures in CVD-grown few-layer hBN islands was observed using AR-TEM. I found atomically sharp twin boundaries along zigzag direction at the AA′/AB stacking boundaries. DFT calculations suggest that the 558 configuration is the stable structure for twin boundary. However, the experimental results claim the existence of 6′6′ configuration (major) as well as 558 configuration (minor) and interswitching of them at the stacking boundary. Further study using MD simulations explains transition of dominant configurations from 558 to 6′6′ with increased thermal energy with raising temperature from 0 to 1000 K. While 558-N shows a reduced bandgap of 3.44 eV compared to ~5 eV of pristine hBN, 6′6′-N has zero bandgap. The reduced bandgap at stacking boundaries was also experimentally detected by using EELS. Moreover, I postulate that atomically sharp stacking boundaries are created from given stacking combinations of AA′/AB, which is inferred from the EK edges of hBN layer boundaries. This gives an insight for the fabrication of atomic wide electronic channel. Ultimately, the twin boundary of AA′/AB-stacked hBN is promising as a one-dimensional conducting channel embedded in the original insulating hBN sheet, i.e. single-hBN electronic device.

Chapter 6: Conclusion

I have studied on defect formation mechanism and growth mechanism of 2D materials using advanced TEM. Based on the characterization of various types of defects and novel features on 2D materials using AR-TEM, DF-TEM, EELS, the growth mechanisms and defect formation mechanisms in given growth conditions and/or stacking structures, domain boundaries were inferred. TEM image simulations, DFT calculations and MD simulations were further performed to support the observations in TEM.

In summary, hole defects on hBN were systematically controlled in triangular, hexagonal, and random shape by controlling the stacking structures. Saw-teeth shaped triangular hole defects in AB-stacked hBN is now being further studied. Spiral growth of hBN was also studied including finding of initiation of screw-dislocations at APB and explanation of the conditions whether the shear strain is created between merging spiral islands. Moreover, I postulate that atomically sharp stacking boundaries are created from given stacking combinations of AA′/AB, which is inferred from the EK edges of hBN layer boundaries. Bandgap close to 0 eV at the atomic-wide twin boundary was measured using EELS, suggesting potential possibility as a one-dimensional electronic channel embedded in original insulating hBN matrix. This is meaningful that TEM study is able to explain the relation between structure and property, as well as to characterize the crystal structures.

Besides the study described above, growth mechanism of multilayer graphene was established by comparing spiral growth and concentric growth synthesized by atmospheric CVD[171]. Overlapping and folding of single crystal graphene in merging area synthesized on Cu-Ni substrate was also confirmed[201]. I believe these studies provide more clear understanding in the mechanism of defects formation and defect-driven growth of 2D materials and make a step forward for practical use of 2D materials.

References

1. Banhart, F.; Kotakoski, J.; Krasheninnikov, A. V., Structural Defects in Graphene. *ACS Nano* **2010,** *5* (1), 26-41.

2. Girit, Ç. Ö.; Meyer, J. C.; Erni, R.; Rossell, M. D.; Kisielowski, C.; Yang, L.; Park, C.-H.; Crommie, M.; Cohen, M. L.; Louie, S. G., Graphene at the edge: stability and dynamics. *science* **2009,** *323* (5922), 1705-1708.

3. Attaccalite, C.; Bockstedte, M.; Marini, A.; Rubio, A.; Wirtz, L., Coupling of excitons and defect states in boron-nitride nanostructures. *Phys Rev B* **2011,** *83* (14).

4. Lahiri, J.; Lin, Y.; Bozkurt, P.; Oleynik, I. I.; Batzill, M., An extended defect in graphene as a metallic wire. *Nat Nanotechnol* **2010,** *5* (5), 326-329.

5. Yazyev, O. V.; Louie, S. G., Electronic transport in polycrystalline graphene. *Nat Mater* **2010,** *9* (10), 806-809.

6. Zhou, W.; Zou, X. L.; Najmaei, S.; Liu, Z.; Shi, Y. M.; Kong, J.; Lou, J.; Ajayan, P. M.; Yakobson, B. I.; Idrobo, J. C., Intrinsic Structural Defects in Monolayer Molybdenum Disulfide. *Nano Lett* **2013,** *13* (6), 2615-2622.

7. Li, X. S.; Cai, W. W.; An, J. H.; Kim, S.; Nah, J.; Yang, D. X.; Piner, R.; Velamakanni, A.; Jung, I.; Tutuc, E.; Banerjee, S. K.; Colombo, L.; Ruoff, R. S., Large-Area Synthesis of High-Quality and Uniform Graphene Films on Copper Foils. *Science* **2009,** *324* (5932), 1312-1314.

8. Chen, J. H.; Shi, T. W.; Cai, T. C.; Xu, T.; Sun, L. T.; Wu, X. S.; Yu, D. P., Self healing of defected graphene. *Appl Phys Lett* **2013,** *102* (10).

9. Lam, D. V.; Kim, S. M.; Cho, Y.; Kim, J. H.; Lee, H. J.; Yang, J. M.; Lee, S. M., Healing defective CVD-graphene through vapor phase treatment. *Nanoscale* **2014,** *6* (11), 5639-5644.

10. Garaj, S.; Hubbard, W.; Reina, A.; Kong, J.; Branton, D.; Golovchenko, J. A., Graphene as a s ubnanometre trans-electrode membrane. *Nature* **2010,** *467* (7312), 190-3.

11. Merchant, C. A.; Healy, K.; Wanunu, M.; Ray, V.; Peterman, N.; Bartel, J.; Fischbein, M. D.; Venta, K.; Luo, Z.; Johnson, A. T.; Drndic, M., DNA translocation through graphene nanopores. *Nano Lett* **2010,** *10* (8), 2915-21.

12. Schneider, G. F.; Kowalczyk, S. W.; Calado, V. E.; Pandraud, G.; Zandbergen, H. W.; Vandersypen, L. M.; Dekker, C., DNA translocation through graphene nanopores. *Nano Lett* **2010,** *10* (8), 3163-7.

13. Garaj, S.; Liu, S.; Golovchenko, J. A.; Branton, D., Molecule-hugging graphene nanopores. *Proceedings of the National Academy of Sciences of the United States of America* **2013,** *110* (30), 12192-6.

14. Dan, Y.; Lu, Y.; Kybert, N. J.; Luo, Z.; Johnson, A. T., Intrinsic response of graphene vapor sensors. *Nano Lett* **2009,** *9* (4), 1472-5.

15. Sint, K.; Wang, B.; Kral, P., Selective ion passage through functionalized graphene nanopores. *Journal of the American Chemical Society* **2008,** *130* (49), 16448-9.

16. Koenig, S. P.; Wang, L.; Pellegrino, J.; Bunch, J. S., Selective molecular sieving through porous graphene. *Nat Nanotechnol* **2012,** *7* (11), 728-32.

17. Liu, S.; Zhao, Q.; Xu, J.; Yan, K.; Peng, H.; Yang, F.; You, L.; Yu, D., Fast and controllable fabrication of suspended graphene nanopore devices. *Nanotechnology* **2012,** *23* (8), 085301.

18. Xu, Q.; Wu, M. Y.; Schneider, G. F.; Houben, L.; Malladi, S. K.; Dekker, C.; Yucelen, E.; Dunin-Borkowski, R. E.; Zandbergen, H. W., Controllable atomic scale patterning of freestanding monolayer graphene at elevated temperature. *Acs Nano* **2013,** *7* (2), 1566-72.

19. Liu, S.; Lu, B.; Zhao, Q.; Li, J.; Gao, T.; Chen, Y.; Zhang, Y.; Liu, Z.; Fan, Z.; Yang, F.; You, L.; Yu, D., Boron nitride nanopores: highly sensitive DNA single-molecule detectors. *Adv Mater* **2013,** *25* (33), 4549-54.

20. Farimani, A. B.; Min, K.; Aluru, N. R., DNA base detection using a single-layer MoS2. *Acs Nano* **2014,** *8* (8), 7914-22.

21. Liu, K.; Feng, J.; Kis, A.; Radenovic, A., Atomically thin molybdenum disulfide nanopores with high sensitivity for DNA translocation. *Acs Nano* **2014,** *8* (3), 2504-11.

22. Waduge, P.; Bilgin, I.; Larkin, J.; Henley, R. Y.; Goodfellow, K.; Graham, A. C.; Bell, D. C.; Vamivakas, N.; Kar, S.; Wanunu, M., Direct and Scalable Deposition of Atomically Thin Low-Noise MoS2 Membranes on Apertures. *Acs Nano* **2015,** *9* (7), 7352-9.

23. Nam, N. N. T.; Koshino, M., Electron transmission through a stacking domain boundary in multilayer graphene. *Phys Rev B* **2015,** *91* (21).

24. San-Jose, P.; Gorbachev, R. V.; Geim, A. K.; Novoselov, K. S.; Guinea, F., Stacking Boundaries and Transport in Bilayer Graphene. *Nano Lett* **2014,** *14* (4), 2052-2057.

25. Ghorbani-Asl, M.; Enyashin, A. N.; Kuc, A.; Seifert, G.; Heine, T., Defect-induced conductivity anisotropy in MoS2 monolayers. *Phys Rev B* **2013,** *88* (24).

26. Gunlycke, D.; White, C. T., Graphene Valley Filter Using a Line Defect. *Phys Rev Lett* **2011,** *106* (13).

27. Lin, Y. C.; Bjorkman, T.; Komsa, H. P.; Teng, P. Y.; Yeh, C. H.; Huang, F. S.; Lin, K. H.; Jadczak, J.; Huang, Y. S.; Chiu, P. W.; Krasheninnikov, A. V.; Suenaga, K., Three-fold rotational defects in two-dimensional transition metal dichalcogenides. *Nat Commun* **2015,** *6*.

28. Barja, S.; Wickenburg, S.; Liu, Z. F.; Zhang, Y.; Ryu, H. J.; Ugeda, M. M.; Hussain, Z.; Shen, Z. X.; Mo, S. K.; Wong, E.; Salmeron, M. B.; Wang, F.; Crommie, M. F.; Ogletree, D. F.; Neaton, J. B.; Weber-Bargioni, A., Charge density wave order in 1D mirror twin boundaries of single-layer MoSe2. *Nat Phys* **2016,** *12* (8), 751-756.

29. Li, Q. C.; Zou, X. L.; Liu, M. X.; Sun, J. Y.; Gao, Y. B.; Qi, Y.; Zhou, X. B.; Yakobson, B. I.; Zhang, Y. F.; Liu, Z. F., Grain Boundary Structures and Electronic Properties of Hexagonal Boron Nitride on Cu(111). *Nano Lett* **2015,** *15* (9), 5804-5810.

30.   Dean, C. R.; Young, A. F.; Meric, I.; Lee, C.; Wang, L.; Sorgenfrei, S.; Watanabe, K.; Taniguchi, T.; Kim, P.; Shepard, K. L.; Hone, J., Boron nitride substrates for high-quality graphene electronics. *Nat Nanotechnol* **2010,** *5* (10), 722-6.

31.   Liu, Z.; Gong, Y.; Zhou, W.; Ma, L.; Yu, J.; Idrobo, J. C.; Jung, J.; MacDonald, A. H.; Vajtai, R.; Lou, J.; Ajayan, P. M., Ultrathin high-temperature oxidation-resistant coatings of hexagonal boron nitride. *Nat Commun* **2013,** *4*.

32.   Billinge, S. J.; Levin, I., The problem with determining atomic structure at the nanoscale. *Science* **2007,** *316* (5824), 561-565.

33.   Urban, K. W., Studying atomic structures by aberration-corrected transmission electron microscopy. *Science* **2008,** *321* (5888), 506-510.

34.   Smith, D. J., The realization of atomic resolution with the electron microscope. *Rep Prog Phys* **1997,** *60* (12), 1513-1580.

35.   Urban, K. W., Is science prepared for atomic-resolution electron microscopy? *Nat Mater* **2009,** *8* (4), 260-262.

36.   Smith, D. J., The realization of atomic resolution with the electron microscope. *Reports on Progress in Physics* **1997,** *60* (12), 1513.

37.   Haider, M.; Uhlemann, S.; Schwan, E.; Rose, H.; Kabius, B.; Urban, K., Electron microscopy image enhanced. *Nature* **1998,** *392*, 768-769.

38.   Dellby, N.; Krivanek, L.; Nellist, D.; Batson, E.; Lupini, R., Progress in aberration-corrected scanning transmission electron microscopy. *Journal of Electron Microscopy* **2001,** *50* (3), 177-185.

39.   Varela, M.; Lupini, A. R.; Benthem, K. v.; Borisevich, A. Y.; Chisholm, M. F.; Shibata, N.; Abe, E.; Pennycook, S. J., Materials characterization in the aberration-corrected scanning transmission electron microscope. *Annu. Rev. Mater. Res.* **2005,** *35*, 539-569.

40.   Lentzen, M., Progress in aberration-corrected high-resolution transmission electron microscopy using hardware aberration correction. *Microscopy and Microanalysis* **2006,** *12* (3), 191-205.

41.   Smith, D. J., Development of aberration-corrected electron microscopy. *Microscopy and Microanalysis* **2008,** *14* (1), 2-15.

42.   Scherzer, O., Über einige fehler von elektronenlinsen. *Zeitschrift für Physik* **1936,** *101* (9-10), 593-603.

43.   Haider, M.; Muller, H.; Uhlemann, S.; Zach, J.; Loebau, U.; Hoeschen, R., Prerequisites for a C-c/C-s-corrected ultrahigh-resolution TEM. *Ultramicroscopy* **2008,** *108* (3), 167-178.

44.   Preikszas, D.; Rose, H., Correction properties of electron mirrors. *J Electron Microsc* **1997,** *46* (1), 1-9.

45.   Zach, J. C.; Haider, M., Aberration Correction in a Low-Voltage Sem by a Multipole Corrector. *Nucl Instrum Meth A* **1995,** *363* (1-2), 316-325.

46.   Haider, M.; Uhlemann, S.; Schwan, E.; Rose, H.; Kabius, B.; Urban, K., Electron microscopy image enhanced. *Nature* **1998,** *392* (6678), 768-769.

47.   Jia, C. L.; Lentzen, M.; Urban, K., Atomic-resolution imaging of oxygen in perovskite ceramics. *Science* **2003,** *299* (5608), 870-873.

48.   Morniroli, J. P.; Houdellier, F.; Roucau, C.; Puiggali, J.; Gesti, S.; Redjaimia, A., LACDIF, a new electron diffraction technique obtained with the LACBED configuration and a C-s corrector: Comparison with electron precession. *Ultramicroscopy* **2008,** *108* (2), 100-115.

49.   Rose, H., Outline of a Spherically Corrected Semiaplanatic Medium-Voltage Transmission Electron-Microscope. *Optik* **1990,** *85* (1), 19-24.

50.   Krivanek, O. L.; Dellby, N.; Lupini, A. R., Towards sub-angstrom electron beams. *Ultramicroscopy* **1999,** *78* (1-4), 1-11.

51.   Krivanek, O. L.; Corbin, G. J.; Dellby, N.; Elston, B. F.; Keyse, R. J.; Murfitt, M. F.; Own, C. S.; Szilagyi, Z. S.; Woodruff, J. W., An electron microscope for the aberration-corrected era. *Ultramicroscopy* **2008,** *108* (3), 179-195.

52.   Warner, J. H.; Margine, E. R.; Mukai, M.; Robertson, A. W.; Giustino, F.; Kirkland, A. I., Dislocation-driven deformations in graphene. *Science* **2012,** *337* (6091), 209-212.

53.   Rose, H., Correction of Aberrations, a Promising Means for Improving the Spatial and Energy Resolution of Energy-Filtering Electron-Microscopes. *Ultramicroscopy* **1994,** *56* (1-3), 11-25.

54.   Pennycook, S. J.; Varela, M.; Hetherington, C. J. D.; Kirkland, A. I., Materials advances through aberration-corrected electron microscopy. *Mrs Bull* **2006,** *31* (1), 36-43.

55.   Yang, J. C.; Small, M. W.; Grieshaber, R. V.; Nuzzo, R. G., Recent developments and applications of electron microscopy to heterogeneous catalysis. *Chem Soc Rev* **2012,** *41* (24), 8179-8194.

56.   Suenaga, K.; Koshino, M., Atom-by-atom spectroscopy at graphene edge. *Nature* **2010,** *468* (7327), 1088-1090.

57.   Varela, M.; Findlay, S. D.; Lupini, A. R.; Christen, H. M.; Borisevich, A. Y.; Dellby, N.; Krivanek, O. L.; Nellist, P. D.; Oxley, M. P.; Allen, L. J.; Pennycook, S. J., Spectroscopic imaging of single atoms within a bulk solid. *Phys Rev Lett* **2004,** *92* (9).

58.   Bosman, M.; Keast, V. J.; Garcia-Munoz, J. L.; D'Alfonso, A. J.; Findlay, S. D.; Allen, L. J., Two-dimensional mapping of chemical information at atomic resolution. *Phys Rev Lett* **2007,** *99* (8).

59.   Muller, D. A.; Kourkoutis, L. F.; Murfitt, M.; Song, J. H.; Hwang, H. Y.; Silcox, J.; Dellby, N.; Krivanek, O. L., Atomic-scale chemical imaging of composition and bonding by aberration-corrected microscopy. *Science* **2008,** *319* (5866), 1073-1076.

60.   Russo, C. J.; Golovchenko, J. A., Atom-by-atom nucleation and growth of graphene nanopores. *Proceedings of the National Academy of Sciences of the United States of America* **2012,** *109* (16), 5953-7.

61.   Kim, M.; Safron, N. S.; Han, E.; Arnold, M. S.; Gopalan, P., Fabrication and characterization of large-area, semiconducting nanoperforated graphene materials. *Nano Lett* **2010,** *10* (4), 1125-31.

62. Bieri, M.; Treier, M.; Cai, J.; Ait-Mansour, K.; Ruffieux, P.; Groning, O.; Groning, P.; Kastler, M.; Rieger, R.; Feng, X.; Mullen, K.; Fasel, R., Porous graphenes: two-dimensional polymer synthesis with atomic precision. *Chem Commun (Camb)* **2009,** (45), 6919-21.

63. Bai, J.; Zhong, X.; Jiang, S.; Huang, Y.; Duan, X., Graphene nanomesh. *Nat Nanotechnol* **2010,** *5* (3), 190-4.

64. Girit, C. O.; Meyer, J. C.; Erni, R.; Rossell, M. D.; Kisielowski, C.; Yang, L.; Park, C. H.; Crommie, M. F.; Cohen, M. L.; Louie, S. G.; Zettl, A., Graphene at the edge: stability and dynamics. *Science* **2009,** *323* (5922), 1705-8.

65. Smith, B. W.; Luzzi, D. E., Electron irradiation effects in single wall carbon nanotubes. *J Appl Phys* **2001,** *90* (7), 3509-3515.

66. Kotakoski, J.; Jin, C. H.; Lehtinen, O.; Suenaga, K.; Krasheninnikov, A. V., Electron knock-on damage in hexagonal boron nitride monolayers. *Phys. Rev. B* **2010,** *82*, 113404.

67. Komsa, H. P.; Kotakoski, J.; Kurasch, S.; Lehtinen, O.; Kaiser, U.; Krasheninnikov, A. V., Two-Dimensional Transition Metal Dichalcogenides under Electron Irradiation: Defect Production and Doping. *Phys Rev Lett* **2012,** *109* (3).

68. Ramasse, Q. M.; Zan, R.; Bangert, U.; Boukhvalov, D. W.; Son, Y. W.; Novoselov, K. S., Direct experimental evidence of metal-mediated etching of suspended graphene. *Acs Nano* **2012,** *6* (5), 4063-71.

69. Crespi, V. H.; Chopra, N. G.; Cohen, M. L.; Zettl, A.; Louie, S. G., Anisotropic electron-beam damage and the collapse of carbon nanotubes. *Phys Rev B* **1996,** *54* (8), 5927-5931.

70. Nakada, K.; Fujita, M.; Dresselhaus, G.; Dresselhaus, M. S., Edge state in graphene ribbons: Nanometer size effect and edge shape dependence. *Physical review. B, Condensed matter* **1996,** *54* (24), 17954-17961.

71. Son, Y. W.; Cohen, M. L.; Louie, S. G., Half-metallic graphene nanoribbons. *Nature* **2006,** *444* (7117), 347-9.

72. Magda, G. Z.; Jin, X.; Hagymasi, I.; Vancso, P.; Osvath, Z.; Nemes-Incze, P.; Hwang, C.; Biro, L. P.; Tapaszto, L., Room-temperature magnetic order on zigzag edges of narrow graphene nanoribbons. *Nature* **2014,** *514* (7524), 608-11.

73. Kim, W. Y.; Kim, K. S., Prediction of Very Large Values of Magnetoresistance in a Graphene Nanoribbon Device. *Nat Nanotechnol* **2008,** *3*, 408-412.

74. Jung, J.; MacDonald, A. H., Carrier Density and Magnetismin Graphene Zigzag Nanoribbons. *Phys. Rev. B* **2009,** *79*, 235433.

75. Kim, K.; Coh, S.; Kisielowski, C.; Crommie, M. F.; Louie, S. G.; Cohen, M. L.; Zettl, A., Atomically perfect torn graphene edges and their reversible reconstruction. *Nat Commun* **2013,** *4*, 2723.

76. Song, B.; Schneider, G. F.; Xu, Q.; Pandraud, G.; Dekker, C.; Zandbergen, H., Atomic-scale electron-beam sculpting of near-defect-free graphene nanostructures. *Nano Lett* **2011,** *11* (6), 2247-50.

77. He, K.; Robertson, A. W.; Fan, Y.; Allen, C. S.; Lin, Y. C.; Suenaga, K.; Kirkland, A. I.; Warner, J. H., Temperature dependence of the reconstruction of zigzag edges in graphene. *Acs Nano* **2015,** *9* (5), 4786-95.

78. Koskinen, P.; Malola, S.; Hakkinen, H., Self-passivating edge reconstructions of graphene. *Phys Rev Lett* **2008,** *101* (11), 115502.

79. Wells, D. B.; Belkin, M.; Comer, J.; Aksimentiev, A., Assessing graphene nanopores for sequencing DNA. *Nano Lett* **2012,** *12* (8), 4117-23.

80. Sathe, C.; Zou, X.; Leburton, J. P.; Schulten, K., Computational investigation of DNA detection using graphene nanopores. *Acs Nano* **2011,** *5* (11), 8842-51.

81. Zan, R.; Ramasse, Q. M.; Bangert, U.; Novoselov, K. S., Graphene Reknits Its Holes. *Nano Lett* **2012,** *12* (8), 3936-3940.

82. Lee, J.; Yang, Z.; Zhou, W.; Pennycook, S. J.; Pantelides, S. T.; Chisholm, M. F., Stabilization of graphene nanopore. *Proceedings of the National Academy of Sciences of the United States of America* **2014,** *111* (21), 7522-6.

83. Kim, G.; Jang, A. R.; Jeong, H. Y.; Lee, Z.; Kang, D. J.; Shin, H. S., Growth of high-crystalline, single-layer hexagonal boron nitride on recyclable platinum foil. *Nano Letters* **2013,** *13* (4), 1834-1839.

84. Dean, C. R.; Young, A. F.; Meric, I.; Lee, C.; Wang, L.; Sorgenfrei, S.; Watanabe, K.; Taniguchi, T.; Kim, P.; Shepard, K. L.; Hone, J., Boron nitride substrates for high-quality graphene electronics. *Nat Nanotechnol* **2010,** *5* (10), 722-6.

85. Ryu, G. H.; Park, H. J.; Ryou, J.; Park, J.; Lee, J.; Kim, G.; Shin, H. S.; Bielawski, C. W.; Ruoff, R. S.; Hong, S.; Lee, Z., Atomic-scale dynamics of triangular hole growth in monolayer hexagonal boron nitride under electron irradiation. *Nanoscale* **2015,** *7* (24), 10600-5.

86. Jin, C.; Lin, F.; Suenaga, K.; Iijima, S., Fabrication of a Freestanding Boron Nitride Single Layer and Its Defect Assignments. *Phys. Rev. Lett.* **2009,** *102* (19), 195505.

87. Meyer, J. C.; Chuvilin, A.; Algara-Siller, G.; Biskupek, J.; Kaiser, U., Selective sputtering and atomic resolution imaging of atomically thin boron nitride membranes. *Nano Lett* **2009,** *9* (7), 2683-9.

88. Yin, L. C.; Cheng, H. M.; Saito, R., Triangle defect states of hexagonal boron nitride atomic layer: Density functional theory calculations. *Phys Rev B* **2010,** *81* (15).

89. Alem, N.; Erni, R.; Kisielowski, C.; Rossell, M. D.; Gannett, W.; Zettl, A., Atomically Thin Hexagonal Boron Nitride Probed by Ultrahigh-Resolution Transmission Electron Microscopy. *Phys. Rev. B* **2009,** *80*, 155425.

90. Pacile, D.; Meyer, J. C.; Girit, C. O.; Zettl, A., The Two-Dimensional Phase of Boron Nitride: Few-Atomic-Layer Sheets and Suspended Membranes. *Appl. Phys. Lett.* **2008,** *92*, 133107.

91. Du, A.; Chen, Y.; Zhu, Z.; Amal, R.; Lu, G. Q.; Smith, S. C., Dots versus antidots: computational exploration of structure, magnetism, and half-metallicity in boron-nitride nanostructures. *Journal of the American Chemical Society* **2009,** *131* (47), 17354-9.

92.   Wilson, J. A.; Yoffe, A. D., Transition Metal Dichalcogenides Discussion and Interpretation of Observed Optical, Electrical and Structural Properties. *Adv Phys* **1969,** *18* (73), 193-&.

93.   Hong, J.; Hu, Z.; Probert, M.; Li, K.; Lv, D.; Yang, X.; Gu, L.; Mao, N.; Feng, Q.; Xie, L.; Zhang, J.; Wu, D.; Zhang, Z.; Jin, C.; Ji, W.; Zhang, X.; Yuan, J., Exploring atomic defects in molybdenum disulphide monolayers. *Nat Commun* **2015,** *6*, 6293.

94.   Liu, X.; Xu, T.; Wu, X.; Zhang, Z.; Yu, J.; Qiu, H.; Hong, J. H.; Jin, C. H.; Li, J. X.; Wang, X. R.; Sun, L. T.; Guo, W., Top-down fabrication of sub-nanometre semiconducting nanoribbons derived from molybdenum disulfide sheets. *Nat Commun* **2013,** *4*, 1776.

95.   Zan, R.; Ramasse, Q. M.; Jalil, R.; Georgiou, T.; Bangert, U.; Novoselov, K. S., Control of radiation damage in MoS2 by graphene encapsulation. *Acs Nano* **2013,** *7* (11), 10167-74.

96.   Zhou, Y.; Yang, P.; Zu, H.; Gao, F.; Zu, X., Electronic structures and magnetic properties of MoS2 nanostructures: atomic defects, nanoholes, nanodots and antidots. *Physical chemistry chemical physics : PCCP* **2013,** *15* (25), 10385-94.

97.   Constantinescu, G.; Kuc, A.; Heine, T., Stacking in Bulk and Bilayer Hexagonal Boron Nitride. *Phys Rev Lett* **2013,** *111* (3).

98.   Pease, R. S., Crystal Structure of Boron Nitride. *Nature* **1950,** *165* (4201), 722-723.

99.   Kim, C. J.; Brown, L.; Graham, M. W.; Hovden, R.; Havener, R. W.; McEuen, P. L.; Muller, D. A.; Park, J., Stacking Order Dependent Second Harmonic Generation and Topological Defects in h-BN Bilayers. *Nano Lett* **2013,** *13* (11), 5660-5665.

100.   Ping, J. L.; Fuhrer, M. S., Layer Number and Stacking Sequence Imaging of Few-Layer Graphene by Transmission Electron Microscopy. *Nano Lett* **2012,** *12* (9), 4635-4641.

101.   Brown, L.; Hovden, R.; Huang, P.; Wojcik, M.; Muller, D. A.; Park, J., Twinning and Twisting of Tri- and Bilayer Graphene. *Nano Lett* **2012,** *12* (3), 1609-1615.

102.   Shevitski, B.; Mecklenburg, M.; Hubbard, W. A.; White, E. R.; Dawson, B.; Lodge, M. S.; Ishigami, M.; Regan, B. C., Dark-field transmission electron microscopy and the Debye-Waller factor of graphene. *Phys Rev B* **2013,** *87* (4).

103.   Alden, J. S.; Tsen, A. W.; Huang, P. Y.; Hovden, R.; Brown, L.; Park, J.; Muller, D. A.; McEuen, P. L., Strain solitons and topological defects in bilayer graphene. *P Natl Acad Sci USA* **2013,** *110* (28), 11256-11260.

104.   Butz, B.; Dolle, C.; Niekiel, F.; Weber, K.; Waldmann, D.; Weber, H. B.; Meyer, B.; Spiecker, E., Dislocations in bilayer graphene. *Nature* **2014,** *505* (7484), 533-+.

105.   Lin, J. H.; Fang, W. J.; Zhou, W.; Lupini, A. R.; Idrobo, J. C.; Kong, J.; Pennycook, S. J.; Pantelides, S. T., AC/AB Stacking Boundaries in Bilayer Graphene. *Nano Lett* **2013,** *13* (7), 3262-3268.

106.   Ishii, T.; Sato, T.; Sekikawa, Y.; Iwata, M., Growth of whiskers of hexagonal boron nitride. *Journal of Crystal Growth* **1981,** *52, Part 1* (0), 285-289.

107.   Paine, R. T.; Narula, C. K., Synthetic routes to boron nitride. *Chemical Reviews* **1990,** *90* (1), 73-91.

108. Alem, N.; Erni, R.; Kisielowski, C.; Rossell, M. D.; Gannett, W.; Zettl, A., Atomically thin hexagonal boron nitride probed by ultrahigh-resolution transmission electron microscopy. *Phys. Rev. B* **2009,** *80* (15), 155425.

109. Meyer, J. C.; Chuvilin, A.; Algara-Siller, G.; Biskupek, J.; Kaiser, U., Selective Sputtering and Atomic Resolution Imaging of Atomically Thin Boron Nitride Membranes. *Nano Lett.* **2009,** *9* (7), 2683-2689.

110. Yin, L.-C.; Cheng, H.-M.; Saito, R., Triangle defect states of hexagonal boron nitride atomic layer: Density functional theory calculations. *Phys Rev B* **2010,** *81* (15), 153407.

111. Derycke, V.; Soukiassian, P.; Mayne, A.; Dujardin, G.; Gautier, J., Carbon atomic chain formation on the β-SiC (100) surface by controlled sp→ sp 3 transformation. *Phys Rev Lett* **1998,** *81* (26), 5868.

112. Heath, J. R.; Zhang, Q.; O'Brien, S. C.; Curl, R. F.; Kroto, H. W.; Smalley, R. E., The formation of long carbon chain molecules during laser vaporization of graphite. *Journal of the American Chemical Society* **1987,** *109* (2), 359-363.

113. Lagow, R. J.; Kampa, J. J.; Wei, H.-C.; Battle, S. L.; Genge, J. W.; Laude, D. A.; Harper, C. J.; Bau, R.; Stevens, R. C.; Haw, J. F.; Munson, E., Synthesis of Linear Acetylenic Carbon: The "sp" Carbon Allotrope. *Science* **1995,** *267* (5196), 362-367.

114. Troiani, H. E.; Miki-Yoshida, M.; Camacho-Bragado, G. A.; Marques, M. A. L.; Rubio, A.; Ascencio, J. A.; Jose-Yacaman, M., Direct Observation of the Mechanical Properties of Single-Walled Carbon Nanotubes and Their Junctions at the Atomic Level. *Nano Lett* **2003,** *3* (6), 751-755.

115. Yuzvinsky, T. D.; Mickelson, W.; Aloni, S.; Begtrup, G. E.; Kis, A.; Zettl, A., Shrinking a Carbon Nanotube. *Nano Lett* **2006,** *6* (12), 2718-2722.

116. Zhao, X.; Ando, Y.; Liu, Y.; Jinno, M.; Suzuki, T., Carbon Nanowire Made of a Long Linear Carbon Chain Inserted Inside a Multiwalled Carbon Nanotube. *Phys Rev Lett* **2003,** *90* (18), 187401.

117. Cretu, O.; Komsa, H.-P.; Lehtinen, O.; Algara-Siller, G.; Kaiser, U.; Suenaga, K.; Krasheninnikov, A. V., Experimental Observation of Boron Nitride Chains. *ACS Nano* **2014**.

118. Zobelli, A.; Gloter, A.; Ewels, C. P.; Seifert, G.; Colliex, C., Electron knock-on cross section of carbon and boron nitride nanotubes. *Phys Rev B* **2007,** *75* (24), 245402.

119. Kresse, G.; Furthmüller, J., Efficiency of ab-initio total energy calculations for metals and semiconductors using a plane-wave basis set. *Comput. Mater. Sci* **1996,** *6* (1), 15-50.

120. Kresse, G.; Furthmüller, J., Efficient iterative schemes for ab initio total-energy calculations using a plane-wave basis set. *Phys Rev B* **1996,** *54* (16), 11169.

121. Blöchl, P. E., Projector augmented-wave method. *Phys Rev B* **1994,** *50* (24), 17953-17979.

122. Kresse, G.; Joubert, D., From ultrasoft pseudopotentials to the projector augmented-wave method. *Phys Rev B* **1999,** *59* (3), 1758-1775.

123. Grimme, S., Semiempirical GGA-type density functional constructed with a long-range dispersion correction. *J Comput Chem* **2006,** *27* (15), 1787-1799.

124. Kohn, W.; Sham, L. J., Self-Consistent Equations Including Exchange and Correlation Effects. *Physical Review* **1965,** *140* (4A), A1133-A1138.

125. Perdew, J. P.; Burke, K.; Ernzerhof, M., Generalized Gradient Approximation Made Simple [Phys. Rev. Lett. 77, 3865 (1996)]. *Phys Rev Lett* **1997,** *78* (7), 1396-1396.

126. Plimpton, S., Fast parallel algorithms for short-range molecular dynamics. *Journal of computational physics* **1995,** *117* (1), 1-19.

127. van Duin, A. C.; Damsté, J. S. S., Computational chemical investigation into isorenieratene cyclisation. *Organic geochemistry* **2003,** *34* (4), 515-526.

128. van Duin, A. C. T.; Dasgupta, S.; Lorant, F.; Goddard, W. A., ReaxFF: A Reactive Force Field for Hydrocarbons. *The Journal of Physical Chemistry A* **2001,** *105* (41), 9396-9409.

129. Zobelli, A.; Ewels, C. P.; Gloter, A.; Seifert, G.; Stephan, O.; Csillag, S.; Colliex, C., Defective Structure of BN Nanotubes: From Single Vacancies to Dislocation Lines. *Nano Lett* **2006,** *6* (9), 1955-1960.

130. Geim, A. K.; Grigorieva, I. V., Van der Waals heterostructures. *Nature* **2013,** *499* (7459), 419-425.

131. Britnell, L.; Gorbachev, R. V.; Jalil, R.; Belle, B. D.; Schedin, F.; Mishchenko, A.; Georgiou, T.; Katsnelson, M. I.; Eaves, L.; Morozov, S. V.; Peres, N. M. R.; Leist, J.; Geim, A. K.; Novoselov, K. S.; Ponomarenko, L. A., Field-effect tunneling transistor based on vertical graphene heterostructures. *Science* **2012,** *335* (6071), 947-50.

132. Avsar, A.; Vera-Marun, I. J.; Tan, J. Y.; Watanabe, K.; Taniguchi, T.; Castro Neto, A. H.; Özyilmaz, B., Air-Stable Transport in Graphene-Contacted, Fully Encapsulated Ultrathin Black Phosphorus-Based Field-Effect Transistors. *ACS Nano* **2015,** *9* (4), 4138-4145.

133. Song, L.; Ci, L.; Lu, H.; Sorokin, P. B.; Jin, C.; Ni, J.; Kvashnin, A. G.; Kvashnin, D. G.; Lou, J.; Yakobson, B. I.; Ajayan, P. M., Large scale growth and characterization of atomic hexagonal boron nitride layers. *Nano Lett* **2010,** *10* (8), 3209-3215.

134. Shi, Y.; Hamsen, C.; Jia, X.; Kim, K. K.; Reina, A.; Hofmann, M.; Hsu, A. L.; Zhang, K.; Li, H.; Juang, Z.-Y.; Dresselhaus, M. S.; Li, L.-J.; Kong, J., Synthesis of few-layer hexagonal boron nitride thin film by chemical vapor deposition. *Nano Lett* **2010,** *10* (10), 4134-4139.

135. Kim, K. K.; Hsu, A.; Jia, X.; Kim, S. M.; Shi, Y.; Hofmann, M.; Nezich, D.; Rodriguez-Nieva, J. F.; Dresselhaus, M.; Palacios, T.; Kong, J., Synthesis of monolayer hexagonal boron nitride on Cu foil using chemical vapor deposition. *Nano Lett* **2012,** *12* (1), 161-166.

136. Liu, L.; Siegel, D. A.; Chen, W.; Liu, P.; Guo, J.; Duscher, G.; Zhao, C.; Wang, H.; Wang, W.; Bai, X.; McCarty, K. F.; Zhang, Z.; Gu, G., Unusual role of epilayer–substrate interactions in determining orientational relations in van der Waals epitaxy. *Proceedings of the National Academy of Sciences* **2014,** *111* (47), 16670-16675.

137. Wood, G. E.; Marsden, A. J.; Mudd, J. J.; Walker, M.; Asensio, M.; Avila, J.; Chen, K.; Bell, G. R.; Wilson, N. R., van der Waals epitaxy of monolayer hexagonal boron nitride on copper foil: growth, crystallography and electronic band structure. *2D Materials* **2015,** *2* (2), 025003.

138.   Frueh, S.; Kellett, R.; Mallery, C.; Molter, T.; Willis, W. S.; King'ondu, C.; Suib, S. L., Pyrolytic Decomposition of Ammonia Borane to Boron Nitride. *Inorg Chem* **2011,** *50* (3), 783-792.

139.   Lu, G. Y.; Wu, T. R.; Yuan, Q. H.; Wang, H. S.; Wang, H. M.; Ding, F.; Xie, X. M.; Jiang, M. H., Synthesis of large single-crystal hexagonal boron nitride grains on Cu-Ni alloy. *Nat Commun* **2015,** *6*.

140.   Tay, R. Y.; Griep, M. H.; Mallick, G.; Tsang, S. H.; Singh, R. S.; Tumlin, T.; Teo, E. H. T.; Karna, S. P., Growth of Large Single-Crystalline Two-Dimensional Boron Nitride Hexagons on Electropolished Copper. *Nano Lett* **2014,** *14* (2), 839-846.

141.   Wang, L.; Wu, B.; Chen, J.; Liu, H.; Hu, P.; Liu, Y., Monolayer Hexagonal Boron Nitride Films with Large Domain Size and Clean Interface for Enhancing the Mobility of Graphene-Based Field-Effect Transistors. *Advanced Materials* **2014,** *26* (10), 1559-1564.

142.   Tay, R. Y.; Park, H. J.; Ryu, G. H.; Tan, D.; Tsang, S. H.; Li, H.; Liu, W.; Teo, E. H. T.; Lee, Z.; Lifshitz, Y.; Ruoff, R. S., Synthesis of aligned symmetrical multifaceted monolayer hexagonal boron nitride single crystals on resolidified copper. *Nanoscale* **2016,** *8* (4), 2434-2444.

143.   Liu, Y.; Bhowmick, S.; Yakobson, B. I., BN white graphene with "colorful" edges: The energies and morphology. *Nano Lett* **2011,** *11* (8), 3113-3116.

144.   Zhang, Z.; Liu, Y.; Yang, Y.; Yakobson, B. I., Growth Mechanism and Morphology of Hexagonal Boron Nitride. *Nano Lett* **2016,** *16* (2), 1398-1403.

145.   Zhao, R.; Gao, J.; Liu, Z.; Ding, F., The reconstructed edges of the hexagonal BN. *Nanoscale* **2015,** *7* (21), 9723-9730.

146.   Kidambi, P. R.; Blume, R.; Kling, J.; Wagner, J. B.; Baehtz, C.; Weatherup, R. S.; Schloegl, R.; Bayer, B. C.; Hofmann, S., In Situ Observations during Chemical Vapor Deposition of Hexagonal Boron Nitride on Polycrystalline Copper. *Chemistry of Materials* **2014,** *26* (22), 6380-6392.

147.   Ji, Y. X.; Calderon, B.; Han, Y. M.; Cueva, P.; Jungwirth, N. R.; Alsalman, H. A.; Hwang, J.; Fuchs, G. D.; Muller, D. A.; Spencer, M. G., Chemical Vapor Deposition Growth of Large Single-Crystal Mono-, Bi-, Tri-Layer Hexagonal Boron Nitride and Their Interlayer Stacking. *Acs Nano* **2017,** *11* (12), 12057-12066.

148.   Shu, N.; Wei, W.; Shirui, X.; Qingkai, Y.; Jiming, B.; Shin-shem, P.; Kevin, F. M., Growth from below: bilayer graphene on copper by chemical vapor deposition. *New Journal of Physics* **2012,** *14* (9), 093028.

149.   Li, Q.; Chou, H.; Zhong, J.-H.; Liu, J.-Y.; Dolocan, A.; Zhang, J.; Zhou, Y.; Ruoff, R. S.; Chen, S.; Cai, W., Growth of Adlayer Graphene on Cu Studied by Carbon Isotope Labeling. *Nano Lett* **2013,** *13* (2), 486-490.

150.   Fang, W.; Hsu, A. L.; Caudillo, R.; Song, Y.; Birdwell, A. G.; Zakar, E.; Kalbac, M.; Dubey, M.; Palacios, T.; Dresselhaus, M. S.; Araujo, P. T.; Kong, J., Rapid Identification of Stacking Orientation in Isotopically Labeled Chemical-Vapor Grown Bilayer Graphene by Raman Spectroscopy. *Nano Lett* **2013,** *13* (4), 1541-1548.

151. Hao, Y.; Wang, L.; Liu, Y.; Chen, H.; Wang, X.; Tan, C.; Nie, S.; Suk, J. W.; Jiang, T.; Liang, T.; Xiao, J.; Ye, W.; Dean, C. R.; Yakobson, B. I.; McCarty, K. F.; Kim, P.; Hone, J.; Colombo, L.; Ruoff, R. S., Oxygen-activated growth and bandgap tunability of large single-crystal bilayer graphene. *Nat Nano* **2016,** *11* (5), 426-431.

152. van der Zande, A. M.; Huang, P. Y.; Chenet, D. A.; Berkelbach, T. C.; You, Y. M.; Lee, G. H.; Heinz, T. F.; Reichman, D. R.; Muller, D. A.; Hone, J. C., Grains and grain boundaries in highly crystalline monolayer molybdenum disulphide. *Nat Mater* **2013,** *12* (6), 554-561.

153. Najmaei, S.; Liu, Z.; Zhou, W.; Zou, X. L.; Shi, G.; Lei, S. D.; Yakobson, B. I.; Idrobo, J. C.; Ajayan, P. M.; Lou, J., Vapour phase growth and grain boundary structure of molybdenum disulphide atomic layers. *Nat Mater* **2013,** *12* (8), 754-759.

154. Nicholas, N. W.; Connors, L. M.; Ding, F.; Yakobson, B. I.; Schmidt, H. K.; Hauge, R. H., Templated growth of graphenic materials. *Nanotechnology* **2009,** *20* (24), 245607.

155. Ly, T. H.; Zhao, J.; Kim, H.; Han, G. H.; Nam, H.; Lee, Y. H., Vertically Conductive MoS2 Spiral Pyramid. *Adv Mater* **2016,** *28* (35), 7723-8.

156. Zhang, L.; Liu, K.; Wong, A. B.; Kim, J.; Hong, X.; Liu, C.; Cao, T.; Louie, S. G.; Wang, F.; Yang, P., Three-Dimensional Spirals of Atomic Layered MoS2. *Nano Lett* **2014,** *14* (11), 6418-6423.

157. Chen, L.; Liu, B.; Abbas, A. N.; Ma, Y.; Fang, X.; Liu, Y.; Zhou, C., Screw-Dislocation-Driven Growth of Two-Dimensional Few-Layer and Pyramid-like WSe2 by Sulfur-Assisted Chemical Vapor Deposition. *ACS Nano* **2014,** *8* (11), 11543-11551.

158. Sarma, P. V.; Patil, P. D.; Barman, P. K.; Kini, R. N.; Shaijumon, M. M., Controllable growth of few-layer spiral WS2. *RSC Advances* **2016,** *6* (1), 376-382.

159. Regan, W.; Alem, N.; Aleman, B.; Geng, B. S.; Girit, C.; Maserati, L.; Wang, F.; Crommie, M.; Zettl, A., A direct transfer of layer-area graphene. *Appl Phys Lett* **2010,** *96* (11).

160. Shevitski, B.; Mecklenburg, M.; Hubbard, W. A.; White, E. R.; Dawson, B.; Lodge, M. S.; Ishigami, M.; Regan, B. C., Dark-field transmission electron microscopy and the Debye-Waller factor of graphene. *Phys Rev B Condens Matter Mater Phys* **2013,** *87*, 045417.

161. Ping, J.; Fuhrer, M. S., Layer number and stacking sequence imaging of few-layer graphene by transmission electron microscopy. *Nano Lett* **2012,** *12* (9), 4635-41.

162. Perdew, J. P.; Burke, K.; Ernzerhof, M., Generalized gradient approximation made simple. *Phys Rev Lett* **1996,** *77* (18), 3865.

163. Blöchl, P. E., Projector augmented-wave method. *Phys Rev B* **1994,** *50* (24), 17953.

164. Kresse, G.; Joubert, D., From ultrasoft pseudopotentials to the projector augmented-wave method. *Phys Rev B* **1999,** *59* (3), 1758.

165. Grimme, S., Semiempirical GGA-type density functional constructed with a long-range dispersion correction. *Journal of computational chemistry* **2006,** *27* (15), 1787-1799.

166. Monkhorst, H. J.; Pack, J. D., Special points for Brillouin-zone integrations. *Phys Rev B* **1976,** *13* (12), 5188.

167. Kotakoski, J.; Jin, C. H.; Lehtinen, O.; Suenaga, K.; Krasheninnikov, A. V., Electron knock-on damage in hexagonal boron nitride monolayers. *Phys Rev B* **2010,** *82* (11).

168. Ryu, G. H.; Park, H. J.; Ryou, J.; Park, J.; Lee, J.; Kim, G.; Shin, H. S.; Bielawski, C. W.; Ruoff, R. S.; Hong, S.; Lee, Z., Atomic-scale dynamics of triangular hole growth in monolayer hexagonal boron nitride under electron irradiation. *Nanoscale* **2015,** *7* (24), 10600-10605.

169. Pham, T.; Gibb, A. L.; Li, Z. L.; Gilbert, S. M.; Song, C. Y.; Louie, S. G.; Zett, A., Formation and Dynamics of Electron-Irradiation-Induced Defects in Hexagonal Boron Nitride at Elevated Temperatures. *Nano Lett* **2016,** *16* (11), 7142-7147.

170. Gilbert, S. M.; Dunn, G.; Azizi, A.; Pham, T.; Shevitski, B.; Dimitrov, E.; Liu, S.; Aloni, S.; Zettl, A., Fabrication of Subnanometer-Precision Nanopores in Hexagonal Boron Nitride. *Sci Rep-Uk* **2017,** *7*.

171. Tay, R. Y.; Park, H. J.; Ling, J. J.; Ng, Z. K.; Jing, L.; Li, H. L.; Zhu, M. M.; Tsang, S. H.; Lee, Z.; Teo, E. H. T., Concentric and Spiral Few-Layer Graphene: Growth Driven by Interfacial Nucleation vs Screw Dislocation. *Chem Mater* **2018,** *30* (19), 6858-6866.

172. Lin, J.; Fang, W.; Zhou, W.; Lupini, A. R.; Idrobo, J. C.; Kong, J.; Pennycook, S. J.; Pantelides, S. T., AC/AB stacking boundaries in bilayer graphene. *Nano Lett* **2013,** *13* (7), 3262-8.

173. Markov, I. V., *Crystal growth for beginners : fundamentals of nucleation, crystal growth and epitaxy*. World Scientific: Singapore, 1994.

174. Burton, W. K.; Cabrera, N.; Frank, F. C., Role of Dislocations in Crystal Growth. *Nature* **1949,** *163*, 398-399.

175. Burton, W. K.; Cabrera, N.; Frank, F. C., The Growth of Crystals and the Equilibrium Structure of their Surfaces. *Philosophical Transactions of the Royal Society of London A: Mathematical, Physical and Engineering Sciences* **1951,** *243* (866), 299-358.

176. Watanabe, K.; Taniguchi, T.; Kanda, H., Direct-bandgap properties and evidence for ultraviolet lasing of hexagonal boron nitride single crystal. *Nat Mater* **2004,** *3* (6), 404-409.

177. Ci, L.; Song, L.; Jin, C.; Jariwala, D.; Wu, D.; Li, Y.; Srivastava, A.; Wang, Z. F.; Storr, K.; Balicas, L.; Liu, F.; Ajayan, P. M., Atomic layers of hybridized boron nitride and graphene domains. *Nat Mater* **2010,** *9*, 430.

178. Tay, R. Y.; Li, H. L.; Tsang, S. H.; Zhu, M. M.; Loeblein, M.; Jing, L.; Leong, F. N.; Teo, E. H. T., Trimethylamine Borane: A New Single-Source Precursor for Monolayer h-BN Single Crystals and h-BCN Thin Films. *Chemistry of Materials* **2016,** *28* (7), 2180-2190.

179. Singh, R. S.; Tay, R. Y.; Chow, W. L.; Tsang, S. H.; Mallick, G.; Teo, E. H. T., Band gap effects of hexagonal boron nitride using oxygen plasma. *Appl Phys Lett* **2014,** *104* (16).

180. Kern, G.; Kresse, G.; Hafner, J., Ab initio calculation of the lattice dynamics and phase diagram of boron nitride. *Phys Rev B* **1999,** *59* (13), 8551-8559.

181. Warner, J. H.; Rummeli, M. H.; Bachmatiuk, A.; Buchner, B., Atomic Resolution Imaging and Topography of Boron Nitride Sheets Produced by Chemical Exfoliation. *Acs Nano* **2010,** *4* (3), 1299-1304.

182. Sutter, P.; Lahiri, J.; Zahl, P.; Wang, B.; Sutter, E., Scalable Synthesis of Uniform Few-Layer Hexagonal Boron Nitride Dielectric Films. *Nano Lett* **2013**, *13* (1), 276-281.

183. Kresse, G.; Furthmuller, J., Efficient iterative schemes for ab initio total-energy calculations using a plane-wave basis set. *Phys Rev B* **1996**, *54* (16), 11169-11186.

184. Kresse, G.; Furthmuller, J., Efficiency of ab-initio total energy calculations for metals and semiconductors using a plane-wave basis set. *Comp Mater Sci* **1996**, *6* (1), 15-50.

185. Perdew, J. P.; Burke, K.; Ernzerhof, M., Generalized gradient approximation made simple. *Phys Rev Lett* **1996**, *77* (18), 3865-3868.

186. Weismiller, M. R.; van Duin, A. C. T.; Lee, J.; Yetter, R. A., ReaxFF Reactive Force Field Development and Applications for Molecular Dynamics Simulations of Ammonia Borane Dehydrogenation and Combustion. *J Phys Chem A* **2010**, *114* (17), 5485-5492.

187. Tay, R. Y.; Wang, X. L.; Tsang, S. H.; Loh, G. C.; Singh, R. S.; Li, H.; Mallick, G.; Teo, E. H. T., A systematic study of the atmospheric pressure growth of large-area hexagonal crystalline boron nitride film. *J Mater Chem C* **2014**, *2* (9), 1650-1657.

188. Robertson, A. W.; Warner, J. H., Atomic resolution imaging of graphene by transmission electron microscopy. *Nanoscale* **2013**, *5* (10), 4079-4093.

189. Zan, R.; Bangert, U.; Ramasse, Q.; Novoselov, K. S., Imaging of Bernal stacked and misoriented graphene and boron nitride: experiment and simulation. *Journal of Microscopy* **2011**, *244* (2), 152-158.

190. Eda, G.; Yamaguchi, H.; Voiry, D.; Fujita, T.; Chen, M. W.; Chhowalla, M., Photoluminescence from Chemically Exfoliated MoS2. *Nano Lett* **2011**, *11* (12), 5111-5116.

191. Gutierrez, H. R.; Perea-Lopez, N.; Elias, A. L.; Berkdemir, A.; Wang, B.; Lv, R.; Lopez-Urias, F.; Crespi, V. H.; Terrones, H.; Terrones, M., Extraordinary Room-Temperature Photoluminescence in Triangular WS2 Monolayers. *Nano Lett* **2013**, *13* (8), 3447-3454.

192. Rigosi, A. F.; Hill, H. M.; Rim, K. T.; Flynn, G. W.; Heinz, T. F., Electronic band gaps and exciton binding energies in monolayer MoxW1-xS2 transition metal dichalcogenide alloys probed by scanning tunneling and optical spectroscopy. *Phys Rev B* **2016**, *94* (7).

193. Splendiani, A.; Sun, L.; Zhang, Y. B.; Li, T. S.; Kim, J.; Chim, C. Y.; Galli, G.; Wang, F., Emerging Photoluminescence in Monolayer MoS2. *Nano Lett* **2010**, *10* (4), 1271-1275.

194. Erni, R.; Browning, N. D., Valence electron energy-loss spectroscopy in monochromated scanning transmission electron microscopy. *Ultramicroscopy* **2005**, *104* (3-4), 176-192.

195. Erni, R.; Browning, N. D., Quantification of the size-dependent energy gap of individual CdSe quantum dots by valence electron energy-loss spectroscopy. *Ultramicroscopy* **2007**, *107* (2-3), 267-273.

196. Erni, R.; Browning, N. D., The impact of surface and retardation losses on valence electron energy-loss spectroscopy. *Ultramicroscopy* **2008**, *108* (2), 84-99.

197. Park, J.; Heo, S.; Chung, J. G.; Kim, H.; Lee, H.; Kim, K.; Park, G. S., Bandgap measurement of thin dielectric films using monochromated STEM-EELS. *Ultramicroscopy* **2009,** *109* (9), 1183-1188.

198. Klein, D. J.; Bytautas, L., Graphitic edges and unpaired pi-electron spins. *J Phys Chem A* **1999,** *103* (26), 5196-5210.

199. Klein, D. J., Graphitic Polymer Strips with Edge States. *Chem Phys Lett* **1994,** *217* (3), 261-265.

200. He, K.; Robertson, A. W.; Lee, S.; Yoon, E.; Lee, G. D.; Warner, J. H., Extended Klein Edges in Graphene. *Acs Nano* **2014,** *8* (12), 12272-12279.

201. Huang, M.; Biswal, M.; Park, H. J.; Jin, S.; Qu, D.; Hong, S.; Zhu, Z. L.; Qiu, L.; Luo, D.; Liu, X. C.; Yang, Z.; Liu, Z. L.; Huang, Y.; Lim, H.; Yoo, W. J.; Ding, F.; Wang, Y. L.; Lee, Z.; Ruoff, R. S., Highly Oriented Monolayer Graphene Grown on a Cu/Ni(111) Alloy Foil. *Acs Nano* **2018,** *12* (6), 6117-6127.

CURRICULUM VITAE

HYO JU PARK

Email: hyojupark@unist.ac.kr; hyoju.park90@gmail.com

Birthday: November 11th, 1990

Mobile: +82-10-2592-1514

Address: Bidg.102-511, 50 UNIST-gil, Ulsan 44919, Republic of Korea

Research Gate:

https://www.researchgate.net/profile/Hyo_Ju_Park

EDUCATION

2013 ~ 2018	**Combined M.S. & Ph.D. Course in Materials Science and Engineering**
	UNIST (Ulsan National Institute of Science and Technology), Ulsan, Republic of Korea
	Advisor: Prof. Zonghoon Lee (zhlee@unist.ac.kr, http://ASEMlab.org/)
	(Dissertation title: Study on Mechanism of Defects Formation and Defect-Driven Growth of Two-Dimensional Materials using Transmission Electron Microscopy)
2009 ~ 2013	**B.S. in Materials Science and Engineering, February 2013**
	UNIST (Ulsan National Institute of Science and Technology), Ulsan, Republic of Korea

RESEARCH EXPEREIENCES

2013 ~ 2015	**Graduate Research Assistant**
	Materials Science Department, UNIST, Ulsan, Republic of Korea

PUBLICATIONS

1. **H.J. Park**, R.Y. Tay, X. Wang, W. Zhao, J.H. Kim, R. S. Ruoff, F. Ding, E.H.T. Teo, and Z. Lee*, "Screw Dislocation-Driven Growth of Double-Helix Hexagonal Boron Nitride, *(Submitted)*.

2. **H.J. Park**, J. Cha, J.H. Kim, R.Y. Tay, E.H.T. Teo, S. Hong and Z. Lee*, "One-Dimensional Hexagonal Boron Nitride Semiconductor", *(Submitted)*.

3. R.Y. Tay, **H.J. Park**, J. Lin, Z.K. Ng, L. Jing, H. Li, M. Zhu, S.H. Tsang, Z. Lee, E.H.T. Teo*, "Concentric and Spiral Few-Layer Graphene: Growth Driven by Interfacial Nucleation vs Screw Dislocation", *Chemistry of Materials* 30 (19), 2018.
   -Co-first author

4. J.N. Tiwari, S. Sultan, C.W. Myung, T. Yoon, N. Li, M. Ha, A. M. Harzandi, **H.J. Park**, D.Y. Kim, S.S. Chandrasekaran, W.G. Lee, V. Vij, H. Kang, T.J. Shin, H.S. Shin, G. Lee, Z. Lee, K.S. Kim*, "Multicomponent electrocatalyst with ultralow Pt loading and high hydrogen evolution activity" *Nature Energy* 3, Jul 2018.

5. M. Huang, M. Biswal, **H.J. Park**, S. Jin, D. Qu, S. Hong, Z. Zhu, L Qiu, D. Luo, X. Liu, Z. Yang, Z. Liu, Y. Huang, H. Lim, W.J. Woo, F. Ding, Y. Wang, Z. Lee, and R. S. Ruoff*, "Highly Oriented Monolayer Graphene Grown on a Cu/Ni(111) Alloy Foil", *ACS Nano*, 12 (6), 2018

6. D. Luo, X. You, B.-W. Li, X. Chen, **H.J. Park**, M. Jung, T.Y. Ko, K. Wong, M. Yousaf, X. Chen, M. Huang, S.H. Lee, Z. Lee, H.-J. Shin, S. Ryu, S.K. Kwak, N. Park, R R. Bacsa, W. Bacsa, and R. S. Ruoff*, "Role of Graphene in Water-Assisted Oxidation of Copper in Relation to Dry Transfer of Graphene", *Chemistry of Materials*, 29 (10), May 2017.

7. T.H. Lee, K. Kim, G. Kim, **H.J. Park**, D. Scullion, L. Shaw, M.-G. Kim, X. Gu, W.-G. Bae, E.J.G. Santos, Z. Lee, H.S. Shin, Y. Nishi, and Z. Bao*, "Chemical Vapor-Deposited Hexagonal Boron Nitride as a Scalable Template for High-Performance Organic Field-Effect Transitors", *Chemistry of Materials*, 29 (5), Feb 2017.

8. J. Chen, Y. Han, X. Kon, X. Deng, **H.J. Park**, Y. Guo, S. Jin, Q. Zhikai, Z. Lee, Z. Qiao, R.S. Ruoff, H. Ji*, "The Origin of Improved Electrical Double-Layer Capacitance by Inclusion of Topological Defects and Dopants in Graphene for Supercapacitors", *Angewandte Chemi International Edition*, 55(44), Oct 2016

9. S.-Y. Kim, K. Kim, Y.H. Hwang, J. Park, J. Jang, Y. Nam, Y. Kang, M. Kim, **H.J. Park**, Z. Lee, J. Chol, Y. Kim, S. Jeong, B.-S. Bae, J.U. Park*, "High-Resolution, Electrohydrodynamic Inkjet printing of Stretchable, Metal Oxide Semiconductor Transistors with High Performances", *Nanoscale*, 39, Sep 2016

10. R.Y. Tay, **H.J. Park**, G.H. Ryu, D. Tan, S.H.Tsang, H. Li, W. Liu, E.H.T.Teo*, Z. Lee, Y. Lifshitz and R.S. Ruoff, "Synthesis of Aligned Symmetrical Multifaceted Monolayer Hexagonal Boron Nitride Single Crystals on Resolidified Copper", *Nanoscale*, 8(4), Jan 2016.

11. J. Kim, J.-U. Lee, J. Lee, **H.J. Park**, Z. Lee, C. Lee and H. Cheong*, "Anomalous polarization dependence of Raman scattering and crystallographic orientation of black phosphorus", *Nanoscale*, 7(44), Oct 2015.

12. **H.J. Park**, G.H. Ryu, Z. Lee*, "Hole Defects on 2D Materials Formed by Electron Beam Irradiation: Toward Nanopore Devices", *Applied Microscopy*, 45(3), pp.107-114, Sep 2015
   -Feature on a front cover of Sep 2015

13. B. Park, J. Park, J.G. Son, Y.-J. Kim, S.U. Yu, **H.J. Park**, D.-H. Chae, J. Byun, G. Jeon, S. Huh, S.-K. Lee, A. Mishchenko, S. Hyun, T.G. Lee, S.W. Han, J.-H. Ahn, Z. Lee, C. Hwang, K.S. Novoselov, K.S. Kim, B.H. Hong, J.K. Kim*, "A Facile Route for Patterned Growth of Metal-Insulator Carbon Lateral Junction through One-pot Synthesis", *ACS Nano*, 9(8), Jul 2015.

14. G.H. Ryu, **H.J. Park**, J. Ryou, J. Park, J. Lee, G. Kim, H.S. Shin, C.W. Bielawski, R.S. Ruoff, S. Hong and Z. Lee*, "Atomic-scale dynamics of triangular hole growth in monolayer hexagonal boron nitride under electron irradiation," *Nanoscale* 7, pp. 10600-10605, May 2015.
   -Co-first author
   -Feature on a front cover of Jun 2015
   -Selected as the 2015 Hot Paper in Nanoscale

15. J.M. Yuk, H.Y. Jeong, N.Y. Kim, **H.J. Park**, G. Kim, H.S. Shin, R.S. Ruoff, J.Y. Lee,* and Z. Lee*, "Superstructural defects and superlattice domains in stacked graphene," *Carbon*, 80, 755-761, Sep 2014.

16. G.H. Ryu, **H.J. Park**, N.Y. Kim and Z. Lee*, "Atomic Resolution Imaging of Rotated Bilayer Graphene Sheets using a Low kV Aberration-corrected TEM," *Applied Microscopy*, 42(4),

pp.218-22, Dec 2012.

- Selected as the Journal Cover of December 2012

- Selected as the best paper published in 2012 in the Korean Society of Microscopy Journals

On-going Research

1. Crystallization of dopamine in 2D sheet assisted by graphene vessel
2. Saw-teeth shaped triangular hole defect in AB-stacked hBN

RESEARCH INTEREST

- Imaging, Spectroscopy and Simulation Study on Aberration Corrected TEM/STEM

- Investigation of defect formation mechanism and defect engineering in 2D Crystals

- Study on growth mechanism of 2D materials

- Carbon based nanostructure materials: nanoparticles on carbon matrix, organic materials on graphene

TECHNICAL EXPERIENCE

Atomic-resolution transmission electron microscopy
1. Atomic imaging of 2D materials using aberration corrected TEM (Double corrected FEI Titan Cubed 60-300 with a monochromator, JEOL 2100F with probe corrector)
2. Spectroscopic analysis of soft matters using Electron Energy Loss Spectroscopy (EELS)

Image simulations
- TEM/STEM image simulations using MacTempasX

Synthesis of nanostructures
- Synthesis of high-quality single-layer & multi-layer graphene by chemical vapor deposition method

Modification of materials using chemical and physical methods
1. Oxygen plasma treatments on 2D materials (physical and chemical methods)

2. UV/Ozone treatments on 2D materials (chemical method)

Other analytical equipment
1. Focused Ion Beam (FIB): TEM sample prep, site-specific analysis, deposition, ablation of materials

2. Scanning Electron Microscopy (SEM): analyzing surface of solid materials

CONFERENCE PRESENTATIONS

Conference Proceedings/Extended Abstracts

1. G.H. Ryu, **H.J. Park** and Z.Lee, "Dynamics of triangular hole growth in monolayer hexagonal boron nitride under electron irradiation" *Microscopy & Microanalysis 2015*, 21, Aug 2-6, 2015, Portland, Oregon, USA, pp.739-740

2. N.Y. Kim, G.H. Ryu, **H.J. Park** and Z. Lee, "An Improved Specimen Preparation of porous Powder materials for Transmission Electron Microscopy", *Microscopy & Microanalysis 2014,*20, Aug 3-7, 2014, Hartford, Connecticut, USA, pp.366-367

Presentations

1. **H.J Park**, J. Cha, J.H. Kim, R.Y. Tay, E.H.T. Teo, S. Hong, Z. Lee, "One-Dimensional Hexagonal Boron Nitride Semiconductor", International Microscopy Conference 19, Sep 09-14, 2018, Sydney, Australia (Oral)

2. **H.J. Park**, J.H. Kim, Z. Lee, "Screw Dislocation-Driven Growth of Double-Helical Hexagonal Boron Nitride", International Microscopy Conference 19, Sep 09-14, 2018, Sydney, Australia (Poster)

3. J.H Kim, S.-Y. Kim, Y. Cho, H.-J. Shin, **H.J. Park**, S.-Y. Kwon, Z. Lee, "Dislocations in Bilayer Transition Metal Dichalcogenides", International Microscopy Conference 19, Sep 09-14, 2018, Sydney, Australia (Poster)

4. **H.J. Park**, J.H. Kim, Z. Lee, "Screw-Dislocation Driven Growth of Multilayer Hexagonal Boron Nitride", 2018 Korean Society of Microscopy Conference, Jun 20-22, 2018, Jeju, Korea (Poster)

5. J.H. Kim, S.-Y. Kim, **H.J. Park**, S.-Y. Kwon, Z. Lee, "Direct Growth of Bilayer WS2 with Topological Defects induced by Morphological Defects of Graphene", EAMC3, Nov 07-11, 2017, Busan, Korea (Poster)

6. **H.J. Park**, X. Wang, W. Zhao, J.H. Kim, F. Ding, Z. Lee, "Screw-Dislocation Driven Growth of Multilayer Hexagonal Boron Nitride", EAMC3, Nov 07-11, 2017, Busan, Korea (Oral)

7. M. Huang, M. Biswal, S. Jin, **H.J. Park**, Z. Lee, R.S. Ruoff, "Preparation and use of Cu/Ni(111) alloy substrates for CVD growth of bilayer graphene" RPGR, Sep 25-29, 2016, Seoul, Korea (Poster)

8. S. Lee, **H.J. Park**, Z. Lee, "Epitaxial growth of thckness controllable microplate copper phosphide (Cu3P) on Cu (100) foil", ISSM, Sep 23-26, 2016, China (Poster)

9. D. Luo, X. You, B. Li, **H.J. Park**, M. Jung, Z. Lee, H.-J. Shin, W. Bacsa, R.S. Ruoff, "Understanding the effect of water in the oxidation of graphene coated copper for dry delamination of graphene", Advances in Functional Materials International Conference,

10. **H.J. Park**, G.H. Ryu, R.Y. Tay, E.H.T. Teo, R.S. Ruoff, Z.Lee, "Analyzing the crystalline structures of oriented hBN using transmission electron microscopy", the 3rd Korean Graphene Symposium, April 14-15, 2016, Buyeo, Korea (Poster)

11. G.H. Ryu, **H.J. Park**, J.H. Kim, N.Y. Kim, Z. Lee, "Characteriazation of Defects in 2D Materials at Atomic Scale using Aberration Corrected Transmission Electron Microscopy", International Symposium on Microscopy & Microanalysis of Materials 2015, Nov 11-14, 2015, Chanwon, Korea (Invited)

12. G.H. Ryu, **H.J. Park**, J.H. Kim, N.Y. Kim, Z. Lee, "Characteriazation of Defects in 2D Materials at Atomic Scale using Aberration Corrected Transmission Electron Microscopy", Dasan Conference, Dimensional Properties Materials Research, Nov 2-4, 2015, Jeju, Korea (Invited)

13. J. Kim, J.-U. Lee, J. Lee, **H.J. Park**, Z. Lee, C. Lee and H. Cheong, "Anomalous polarization dependence of Raman scattering and crystallographic orientation of black phosphorus", Dasan Conference, Dimensional Properties Materials Research, Nov 2-4, 2015, Jeju, Korea (Invited)

14. G.H. Ryu, **H.J. Park** and Z.Lee, "Dynamics of triangular hole growth in monolayer hexagonal boron nitride under electron irradiation" Microscopy & Microanalysis 2015, Aug. 2-6,2015, Portland, USA

15. G.H. Ryu, **H.J. Park**, N.Y. Kim, J.H. Kim, H.G. Hong, Z. Lee, "Atomic-scale Research on 2D Materials using Aberration-corrected TEM", 2015 Collaborative Conference on 3D and Materials Research, Jun 15-19, 2015, Korea (Invited)

16. **H.J. Park**, G.H. Ryu, J. Lee, J. Ryou, J. Park, S. Hong and Z. Lee, "원자분해능 투과전자현미경을 이용한 단층 h-BN 의 삼각형 결함 성장 메커니즘", 2015 Korean Society of Microscopy Conference, May 28-29, 2015, Seoul, Korea

17. G.H. Ryu, **H.J. Park**, J. Lee, J. Ryou, J. Park, S. Hong and Z. Lee, "Mechanism of Triangular Hole Growth in Monoalayer hexagonal boron Nitride through Electron Beam Irradiation", the 2nd Korean Graphene Symposium, March 26-27, 2015, Buyeo, Korea (Poster)

18. S. Son, S. Lee, Y. Lee, **H.J. park** and Z. Lee, "Controllable Layer by Layer Plasma Technique for 2-Dimensional Crystals, 2014 Korean Society of Microscopy Conference (Poster)

19. N.Y. Kim, G.H. Ryu, **H.J. Park** and Z. Lee, "An Improved Specimen Preparation of porous Powder materials for Transmission Electron Microscopy", Microscopy & Microanalysis 2014

20. G.H. Ryu, **H.J. Park**, N.Y. Kim, M.J. Lee and Z. Lee, "Graphene research at atomic scale using aberration-corrected TEM", 2014 Collaborative Conference on Materials Research.

21. G.H. Ryu, J.H. Kim, S. Son, **H.J. Park**, K.Kim, M.J. Lee, N.Y. Kim, H. Hong and Z. Lee, "Investigation of stacking structure and grain boundary of bilayer 2D materials using aberration-corrected TEM", 2014 Korean Society of Microscopy Conference (Poster)

22. G.H. Ryu, **H.J. Park,** N.Y. Kim, J.H. Kim, K.Kim, M.J. Lee, S. Son , H. Hong and Z. Lee, "Investigation of stacking structure and grain boundary of bilayer 2D materials using aberration-corrected TEM", the 1st Korean Graphene Symposium, April 3-4, 2014, Buyeo, Korea (Poster)

23. G.H. Ryu, **H.J. Park,** N.Y. Kim, J.H. Kim, K.Kim, M.J. Lee and Z. Lee, "Investigation of stacking structure and defects of bilayer graphene using aberration corrected TEM", International Conference of Surface Engineering, ICSE2013, Nov 18-21, 2013, Korea

24. S. Son , H. Hong, G.H. Ryu, **H.J. Park** and Z. Lee, " Controllable layer by layer plasma etching for hexagonal Boron Nitride", International Conference of Surface Engineering, ICSE2013, Nov 18-21, 2013, Korea (Poster)

ACTIVITIES/AWARDS

1. **Best electron microscopy photo award**, "그래핀 호수의 러버덕", 2018 Korean Society of Microscopy Conference, Jeju, Korea, June 20-22, 2018.

2. **Best poster award**, "Screw-Dislocation Driven Growth of Multilayer Hexagonal Boron Nitride", 2018 Korean Society of Microscopy Conference, June 20-22, 2018, Jeju, Korea.

3. **Best poster award**, "Epitaxial growth of thckness controllable microplate copper phosphide (Cu3P) on Cu (100) foil", ISSM, Sep 23-26, China.

4. **Best electron microscopy photo award**, "해저로 가라앉는 암석덩어리", 2015 Korean Society of Microscopy Conference, May 28-29, 2015, Seoul, Korea.

5. **Best poster award**, "Investigation of stacking structure and grain boundary of bilayer 2D materials using aberration-corrected TEM", 45th Korean Society of Microscopy Spring Conference, May 22-23, 2014, Chonbuk, Korea.

6. **Best paper award**, "Atomic resolution imaging of rotated bilayer graphene sheets using a low kV aberration corrected transmission electron microscope", 44th Korean Society of Microscopy Spring Conference, Yonsei University, Korea, June 13-14, 2013.

COMPLETION OF EDUCATION

Period	Education	Educational institution
2013.07.16-2013.07.19	20th Transmission Electron Microscope workshop (Korea)	Korean Society of Microscopy
	Microscope application and use education	
2014.02.24-2014.02.28	Titan Advanced Materials Sc. Course (Eindhoven, Netherlands)	FEI company (Thermo Fisher Scientific)
	Training using aberration corrected Transmission Electron Microscope	
2014.03.18-2014.03.20	Gatan EELS & EFTEM Analysis School (Korea)	Gatan Inc.
	Training of EELS and EFTEM	

RESEARCH PROJECT PARTICIPATED

1. Growth and defect control in graphene and development of innovative graphene-based electronic devices, Nano Material Technology Development Program, the Ministry of Science, S. Korea (2012.09.01 - 2017.08.31).

2. Atomic scale electron microscopy study on multidimensional carbon materials and 2D crystals (under Prof. Zonghoon Lee), Student researcher, IBS-R019-D1.
   : Center for Multidimensional Carbon Materials (CMCM, director: Prof. Rodney S. Ruoff), Institute of Basic Science.